

AWARD NUMBER: W81XWH-11-1-0242

TITLE: Assessment of Nanobiotechnology-Targeted siRNA Designed to Inhibit NF-KappaB Classical and Alternative Signaling in Breast Tumor Macrophages

PRINCIPAL INVESTIGATOR: Fiona Yull

CONTRACTING ORGANIZATION:
Vanderbilt University
Nashville, TN 37203

REPORT DATE: 12/2014

TYPE OF REPORT: Final

PREPARED FOR: U.S. Army Medical Research and Materiel Command
Fort Detrick, Maryland 21702-5012

DISTRIBUTION STATEMENT: Approved for Public Release;
Distribution Unlimited

The views, opinions and/or findings contained in this report are those of the author(s) and should not be construed as an official Department of the Army position, policy or decision unless so designated by other documentation.

REPORT DOCUMENTATION PAGE

Form Approved
OMB No. 0704-0188

Table of Contents

	<u>Page</u>
1. Introduction.....	1
2. Keywords.....	1
3. Overall Project Summary.....	1 - 12
4. Key Research Accomplishments.....	13
5. Conclusion.....	13
6. Publications, Abstracts, and Presentations.....	14
7. Inventions, Patents and Licenses.....	16
8. Reportable Outcomes.....	16
9. Other Achievements.....	16
10. References.....	18
11. Appendices.....	19 - 81

Introduction

Macrophages have been proposed as a potential target for manipulation of the microenvironment in breast cancer because they are potent effectors of the immune system, demonstrating the ability to secrete a wide range of intercellular signals from pro-inflammatory cytokines and chemokines, to growth and pro-angiogenic factors [1, 2]. NF- κ B (NF- κ B) signaling in macrophages contributes to their impact during breast tumorigenesis [3-9]. Thus, macrophage-targeted modulation of NF- κ B has potential as a novel therapeutic approach for breast cancer. NF- κ B signaling is mediated via two major pathways; the canonical/classical pathway and the alternative pathway both of which have been implicated in oncogenesis [10-13] (Figure 1). Our strategy is designed to use siRNA-mediated knockdown of expression of key proteins within each pathway to examine their individual and combined roles with respect to potential breast cancer immunotherapy. We selected as our initial targets the IKK β activator (canonical) or p52 (alternative) proteins. In order to harness inhibition of these pathways to modulate the tumor microenvironment we determined to deliver siRNA specifically to tumor-associated-macrophages (TAMs). To achieve this goal, the proposed work sought to synthesize, characterize and assess multifunctional nanoparticles for siRNA delivery specifically to tumor-associated-macrophages (TAMs). The nanoparticles produced by our studies have the capacity for siRNA association, protection and endosome release combined with tissue/cell specific delivery. Taken together, this strategy would enable the particles to knockdown protein expression of NF- κ B modulators with exceptional specificity for TAMs. We believe that TAM-specific nanoparticle targeting offers an innovative approach to enable NF- κ B modulation *in vivo* through highly localized siRNA knockdown of critical, pathway-specific proteins that control NF- κ B. Our approach is a novel combination intended to treat primary and metastatic breast cancer, the phase of this disease with the poorest clinical outcomes.

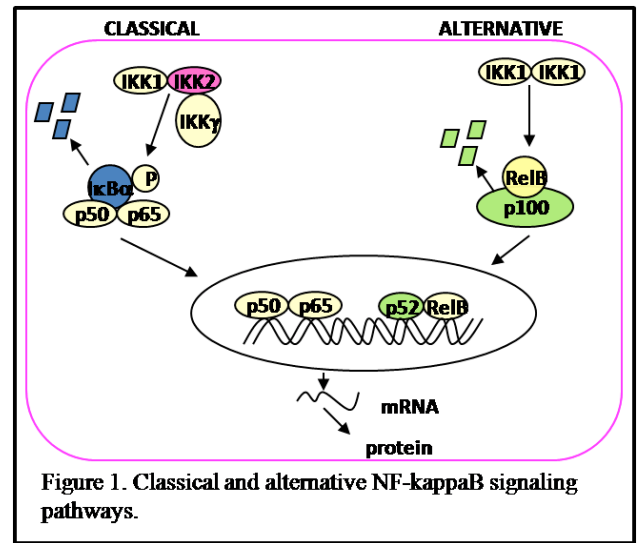


Figure 1. Classical and alternative NF- κ B signaling pathways.

We tested the following ***hypothesis***: siRNA-mediated inhibition of NF- κ B signaling in TAMs will decrease primary tumor growth and metastatic potential. Our ***objectives*** were (1) exploration of macrophage response to inhibition of NF- κ B activation by the canonical and alternative pathways, separately and in combination using siRNA knockdown *in vitro* and (2) development of a nanobiotechnology delivery vehicle with the capacity for siRNA delivery TAMs for the purpose of pathway-specific NF- κ B knockdown *in vivo*.

Keywords Nanoparticles, NF- κ B, macrophages, alternative NF- κ B

Overall Project Summary

Specific Aim 1: Generate siRNA-delivering nanoparticles and optimize dosage *in vitro* in cell cultures of murine bone marrow derived macrophages (BMDM).

- 1a.** Synthesize and fluorescently tag copolymer poly-HPMA-bl-DMAEMA-bl-[DMAEMA-co-PAA-co-BMA], and attach macrophage targeting peptide onto the HPMA end. (Months 1-2)

Task 1a was completed in year 1 (see BC102696 annual report 2012 for details).

1b. Verify pH-responsive endosomolytic activity of new copolymer in hemolysis assays, and characterize polymer physical properties (light scattering, TEM, siRNA complexation assays). (Month 3)

Task 1b was completed in year 1 (see BC102696 annual report 2012 for details).

1c. Expose BMDM from NGL reporter transgenics in culture to the nanoparticles. Quantify peptide-specific & dose-dependent delivery of nanoparticles to the BMDMs by fluorescence microscopy and flow cytometry. [16 mice] (Months 4-5)

Significant portions of Task 1c were completed in years 1 and 2 (see BC102696P1 annual report 2012 and 2013 for details).

TAMs display increased amounts of the mannose receptor, which is the surface ligand targeted by our mannosylated nanoparticles (MnNP). Mannose receptor is also an M2 macrophage marker. We have previously shown that uptake of the MnNP is mannose dependent, and that uptake can be reduced by introducing free mannose during transfection, which competes with the MnNP for uptake by the macrophage mannose receptor. To investigate the differences between untargeted, hydroxyl capped nanoparticles, OHNP, and MnNP, Cy3 labeled dsDNA was loaded into the particles and delivered to BMDMs for 18 hours. Two different populations of BMDMs were used: normal BMDMs and BMDMs stimulated with IL-4 to increase mannose receptor production. Nanoparticle uptake was measured at various time points by measuring Cy3 fluorescence in the BMDMs. In IL-4 stimulated macrophages, uptake of MnNP is significantly increased as compared to uptake of MnNP in unstimulated macrophages (Figure 2). Uptake of OHNP is not significantly different between the two groups of cells. This result indicates that the mannose ligand on the surface of the MnNP is mediating an enhanced uptake effect that is specific for macrophages that have undergone phenotypic differentiation by IL-4.

Although IL-4 stimulated BMDMs are reported to have increased mannose receptor production, unstimulated BMDMs also express this receptor at their surface. This explains why, even at earlier time points, MnNP uptake is enhanced relative to OHNP uptake in both IL-4 stimulated and unstimulated BMDMs. Significant uptake of MnNP occurs as early as 30 minutes after administration to IL-4 stimulated BMDMs. This rapid uptake is consistent with endosomal uptake of the particles, in this case mediated by the mannose receptor. These results also indicate that the particles can be taken up to some small extent in a non-specific manner. It is likely that some particles are phagocytized by the macrophages or taken up via non-specific endosomal pathways.

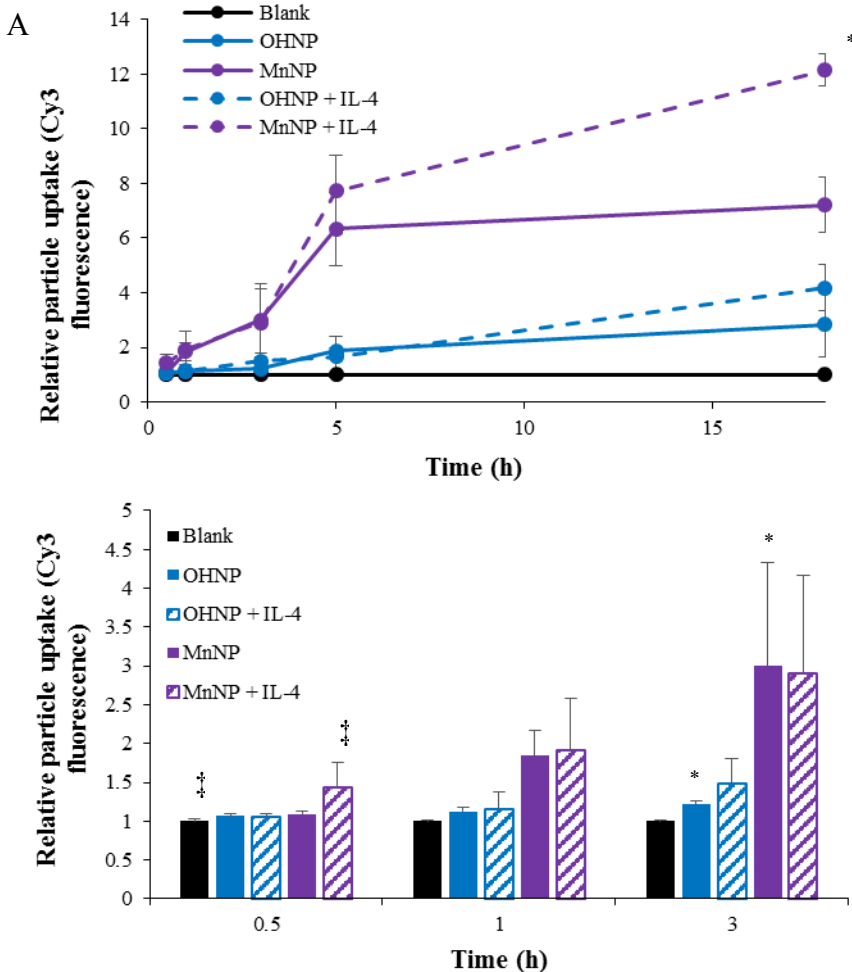


Figure 2: Nanoparticle uptake time course in IL-4 stimulated and unstimulated BMDMs. (A) Uptake of MnNP in IL-4 stimulated BMDMs was significantly greater than uptake in unstimulated BMDMs after 18 hrs. Uptake of MnNP under both conditions was significantly greater than uptake of OHNP after 5 and 18 hours. (B) Earlier time points of nanoparticle uptake are highlighted. Uptake of MnNP occurs as early as 30 minutes after administration. Uptake of MnNP is significantly greater than uptake of OHNP after 1 hour. T-tests for significant differences in group averages were performed between multiple experimental groups. †, **, or ‡: P ≤ 0.05, * or +: P ≤ 0.001.

1d. Deliver IKK2 and p52 siRNA alone and in combination to BMDMs from NGL reporter transgenics *in vitro* and assess modulation of NF- κ B activity by luciferase assay and western analysis of nuclear protein extracts to quantify p65 or p52 translocation to the nucleus as a measure of activation of the canonical and alternative NF- κ B pathways. Further, assess resulting phenotype with respect to M2 v M1 markers by RT-PCR to quantify expression of target genes correlated with M1 (iNOS, MIP1- α , IL-12) or M2 (IL-10, CCL17, mannose receptor) phenotypes. [48 NGL mice] (Months 5-7)

Significant portions of Task 1d were completed in years 1 and 2 (see BC102696P1 annual report 2012 and 2013 for details).

In year 2, it was discovered, by parallel studies supported by other funding sources, that it was possible to activate the classical NF- κ B pathway by knocking down an inhibitor of the pathway using

siRNA. It was hypothesized that activating the classical pathway in this manner in tumor associated macrophages would activate a classical immune response in these cells resulting in anti-tumor effects. Thus phenotypic analysis of TAMs modified using siRNA against the originally hypothesized p52 and the novel $\text{I}\kappa\text{B}\alpha$ target was performed in the extension year, year 3 of the grant. Wild type BMDMs were plated in 6-well plates at a density of 2,000,000 cells per well. Each sample was taken from a different mouse, for a total of 3 biological replicates, with 3 experimental replicates per biological replicate. The cells were transfected using MnNP for 24 hours with $\text{I}\kappa\text{B}\alpha$, p52/p100, or scrambled siRNA, with and without TNF- α stimulation. After transfection, mRNA was collected from the cells for qRT-PCR. mRNA was extracted from cells using Qiagen's RNeasy kit and DNA was removed from the samples using Life Technologies' DNA-free kit. cDNA was prepared from the isolated mRNA using dNTPs from Roche and random hexamers and superscript II reverse transcriptase from Life Technologies. qRT-PCR was performed with SYBR green real-time PCR master mix (Life Technologies) using Applied Biosystems' Step One Plus real-time PCR systems hardware and software. The Step One Plus software was used to automatically calculate optimized baseline and threshold values. Differences in cDNA levels were calculated using the $\Delta\Delta\text{Ct}$ method with GAPDH as an internal control. The sequences used for qRT-PCR are summarized in Table 1.

Table 1: qRT-PCR primer sequences

<u>Gene</u>	<u>Forward Sequence (5'-3')</u>	<u>Reverse Sequence (5'-3')</u>
GAPDH	TGAGGACCAGGTTGTCTCCT	CCCTGTTGCTGTAGCCGTAAT
$\text{I}\kappa\text{B}\alpha$	TGAAGGACGAGGAGTACGAGC	TTCGTGGATGATTGCCAAGTG
p100	GCTTCTCAGCTTCCTCGAGCTA	GCAAATAAACCTCGTCTCCACC
IKK β	GCTGGAGCAGAGAAATGTCAGAGT	CTCAGGAACAATCAAAGCGTGCAG
CXCL9	GTGGTGAAATGGAAAGATCAGGGC	AAGAGAGAAATGGGTTCCCTGGAG
IL-10	ACCTGCTCCACTGCCTTGCT	GGTTGCCAAGCCTTATCGGA
CD206	CAAGGAAGGTTGGCATTTGT	CCTTCAGTCCTTGCAAGC
CCL3	TGCCCTTGCTGTTCTCT	GATGAATTGGCGTGGAAATCT

Figure 3 shows the effect of knocking down p52 on common macrophage phenotype markers. First, p52 mRNA is successfully decreased. CXCL9, an M1 marker and T-cell recruiting cytokine, is increased by knocking down p52 using siRNA delivered by MnNP. Furthermore, this effect acts synergistically with TNF- α , an inflammatory cytokine known to be present in the microenvironment of many breast tumors and metastases. mRNA of the M2 marker, CD206, is significantly decreased as well. Finally, the M2 marker and immunosuppressive cytokine, IL-10, is not significantly affected. This is most likely because p52 is a transcriptionally active protein of the alternative NF- κB pathway, and IL-10 is under classical pathway control.

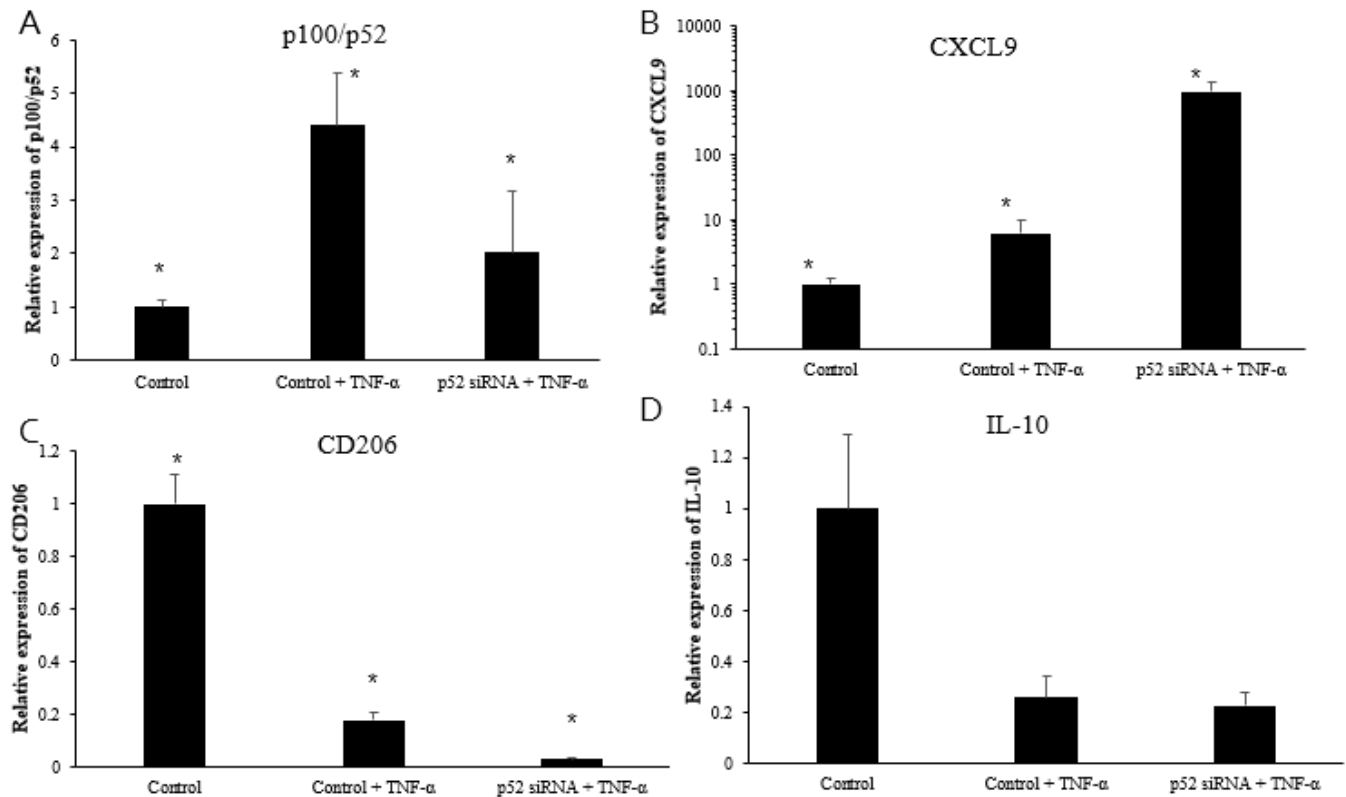


Figure 3: qRT-PCR of p52 siRNA transfected BMDMs. (A) p52 siRNA significantly knocks down p52 mRNA. Although stimulation with TNF- α increase I κ B α mRNA, this effect is significantly reduced by p52 siRNA. (B) p52 siRNA increases mRNA for T-cell recruitment cytokine, CXCL9. The increase in CXCL9 mRNA by transfection alone is significantly greater than the increase caused by TNF- α alone. (C) p52 siRNA decreases mRNA for the mannose receptor, CD206, a trophic, TAM phenotype marker. (D) p52 siRNA does not affect mRNA for IL-10, an immunosuppressive cytokine. * : P < 0.05.

As the combination of these funded studies with other funded studies indicated that it was possible to activate NF- κ B by knocking down the inhibitor of the classical pathway and that I κ B α k/o macrophages can be cytotoxic to tumor cells, the mRNA from BMDMs transfected with I κ B α siRNA by MnNP was analyzed for potential anti-tumor indications. Figure 4A shows that levels of mRNA for I κ B α are significantly decreased following transfection with I κ B α siRNA, indicating successful knockdown at the mRNA level of I κ B α . This can be contrasted to IKK β as a classical pathway target, which we our previous reports had suggested was not an optimal target for mRNA level knockdown.

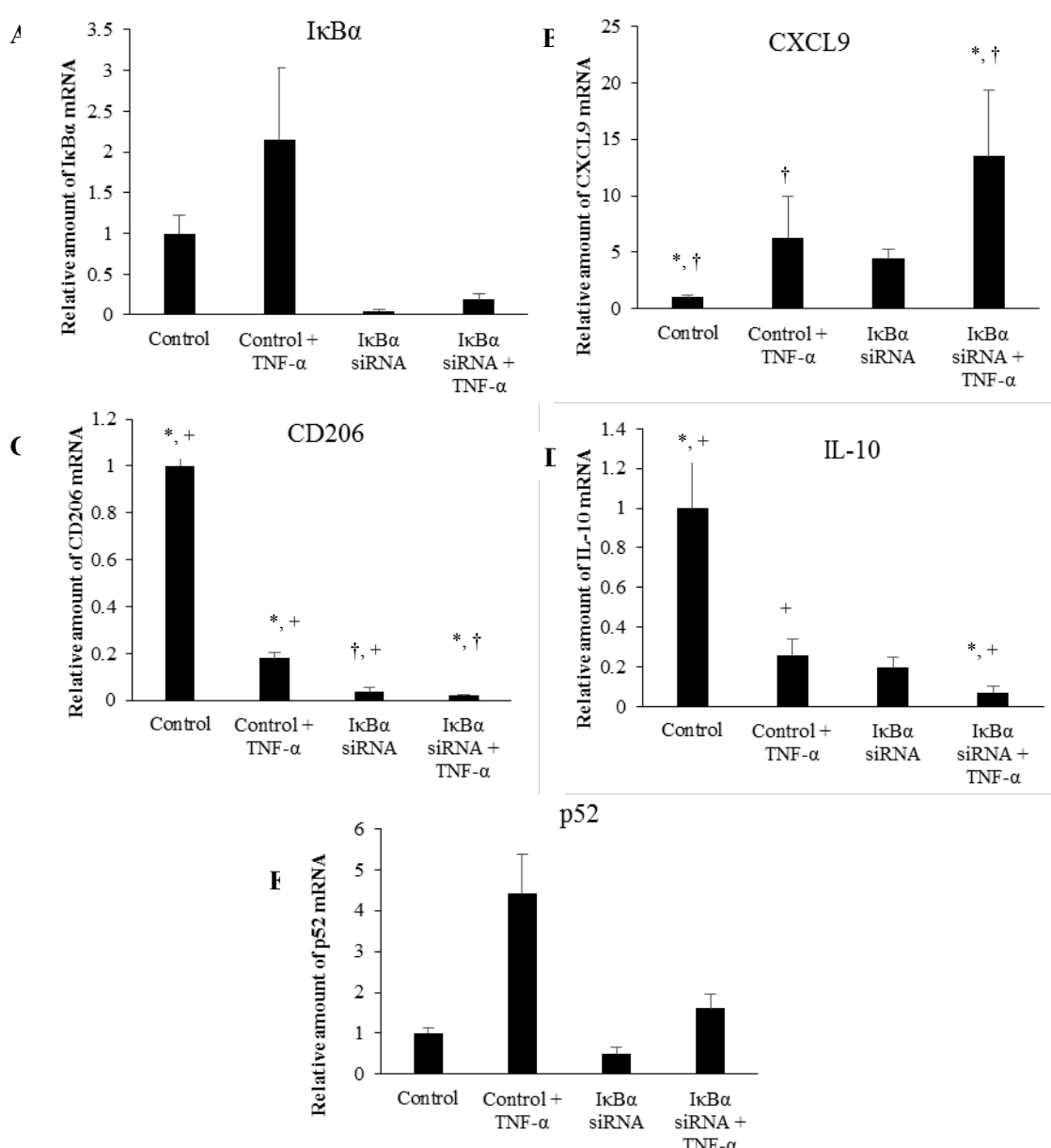


Figure 4: qRT-PCR of IκBα siRNA transfected BMDMs. (A) IκBα siRNA significantly knocks down IκBα mRNA. Although stimulation with TNF- α increase IκBα mRNA, this effect is significantly reduced by IκBα siRNA. (B) IκBα siRNA increases mRNA for T-cell recruitment cytokine, CXCL9. The increase in CXCL9 mRNA by transfection alone is not significantly different than the increase caused by TNF- α alone. (C) IκBα siRNA decreases mRNA for the mannose receptor, CD206, a trophic, TAM phenotype marker. TNF- α alone and MnNP delivered siRNA alone cause a significant decrease in CD206 mRNA. The combination of the two results in significantly greater decrease in CD206 mRNA. (D) IκBα siRNA decreases mRNA for IL-10, an immunosuppressive cytokine. The decrease in IL-10 mRNA by transfection alone is not significantly different than the decrease caused by TNF- α alone, but the combination of the two results in less IL-10 mRNA than either condition by itself. (E) IκBα siRNA decreases mRNA for p52. As previously shown, TNF- α stimulation of macrophages increases levels of p52 mRNA, indicating that p52 is a viable target for mRNA level knockdown. Transfection with IκBα siRNA reduces the increase in p52 mRNA caused by TNF- α , indicating potentially beneficial cross-talk between the two pathways which could be leveraged to act synergistically toward altering the TAM phenotype to an anti-tumor phenotype. \dagger : $P \leq 0.01$, * : $P \leq 0.005$

Figure 4 also shows modifications in the mRNA levels of cancer-context relevant cytokines produced by macrophages. IκBα siRNA increase the amount of CXCL9 mRNA in macrophages to a level that is not significantly different from levels of CXCL9 mRNA in TNF- α stimulated macrophages. CXCL9 is a chemotactic signal that is capable of recruiting CD8 $^{+}$ T-cells and NK cells. Furthermore, the combination of IκBα siRNA and TNF- α acts in an additive fashion, resulting in significantly more CXCL9 mRNA than either of the two treatments alone. Increasing CXCL9 in the tumor microenvironment has been shown to

enhance antitumor immunity in murine breast cancer models. MnNP-delivered $\text{I}\kappa\text{B}\alpha$ siRNA also decrease levels of phenotypic markers indicating a trophic and immunosuppressive macrophage phenotype. Increased levels of the mannose receptor, CD206, in macrophages indicates an alternatively activated phenotype and/or a TAM phenotype. Both TNF- α and $\text{I}\kappa\text{B}\alpha$ siRNA decrease mRNA for CD206 in macrophages. The combination of the two also significantly decreases CD206 mRNA. This effect is particularly important because the mannose receptor is the target of the mannose ligand on the MnNP surface. Transfected macrophages with $\text{I}\kappa\text{B}\alpha$ siRNA effectively decreases the amount of target on the macrophages surface. This effect could ensure that only macrophages with a strong TAM phenotype, cells with more CD206 on their surface, have enhanced, endosomal uptake of the particles. Ideally, the MnNP would preferentially transfect macrophages with high levels of CD206. Transfection would then alter the phenotype of the macrophage toward classical immune activity, reducing the amount of CD206 on the cell surface, preventing further, unnecessary transfection. The MnNP would then be free to transfect other resident macrophages with high levels of CD206 or other recruited macrophages with a trophic or TAM phenotype. The MnNP could also potentially act as a surveillance mechanism while they are retained in the tumor, re-transfected macrophages if they begin to re-adopt a TAM phenotype and express CD206 at their surface.

$\text{I}\kappa\text{B}\alpha$ siRNA also decreases IL-10 mRNA in macrophages. $\text{I}\kappa\text{B}\alpha$ siRNA decreases the amount of IL-10 mRNA in macrophages to a level that is not significantly different from levels of IL-10 mRNA in TNF- α stimulated macrophages and the combination of $\text{I}\kappa\text{B}\alpha$ siRNA and TNF- α results in significantly less IL-10 mRNA than either of the two treatments alone. IL-10 is a potent immunosuppressive cytokine and is implicated in creating the TAM phenotype by paracrine signaling from tumor cells and other TAMs, and by autocrine signaling as well. Transfection with $\text{I}\kappa\text{B}\alpha$ siRNA not only decreases IL-10 mRNA, but it also increases the transfected macrophages' ability to respond to TNF- α that would be predicted to be present in the tumor microenvironment.

Finally, our results have suggested that there is a certain amount in cross-talk between the two pathways that could be leveraged to reduce the negative effects of the TAM phenotype. This result is corroborated by the fact that mRNA levels of p52, which increase following TNF- α stimulation, are decreased by transfection with $\text{I}\kappa\text{B}\alpha$ siRNA. This effect may be the result of direct or indirect crosstalk, and could indicate the potential possibility of decreasing the trophic effects of the alternative NF- κB pathway by knocking down the $\text{I}\kappa\text{B}\alpha$ and activating the classical pathway.

To confirm that the effects of MnNP delivered siRNA shown in Figure 1 were not artifacts caused by macrophage interaction with the MnNP transfection agent, MnNP were used to transfect BMDMs with a scrambled siRNA sequence following the same protocol. Figure 5 shows that there are no significant differences between macrophages transfected with scrambled siRNA sequences and untransfected macrophages for mRNA for $\text{I}\kappa\text{B}\alpha$, p52, CXCL9, and IL-10. There is some significant **increase** in CD206 upon uptake of the MnNP. This is consistent with the reported mechanism of CD206 production following CD206 binding events. It has been reported that as the number of CD206 binding and endosomal uptake events increases, so does production of CD206. This increase in receptor production following activation helps to explain the rapid recycling of this receptor. The small increase in CD206 following scrambled siRNA MnNP delivery highlights the ability of $\text{I}\kappa\text{B}\alpha$ knockdown to reduce CD206 mRNA: MnNP-delivered, $\text{I}\kappa\text{B}\alpha$ siRNA alone reduces CD206 mRNA by approximately 95%.

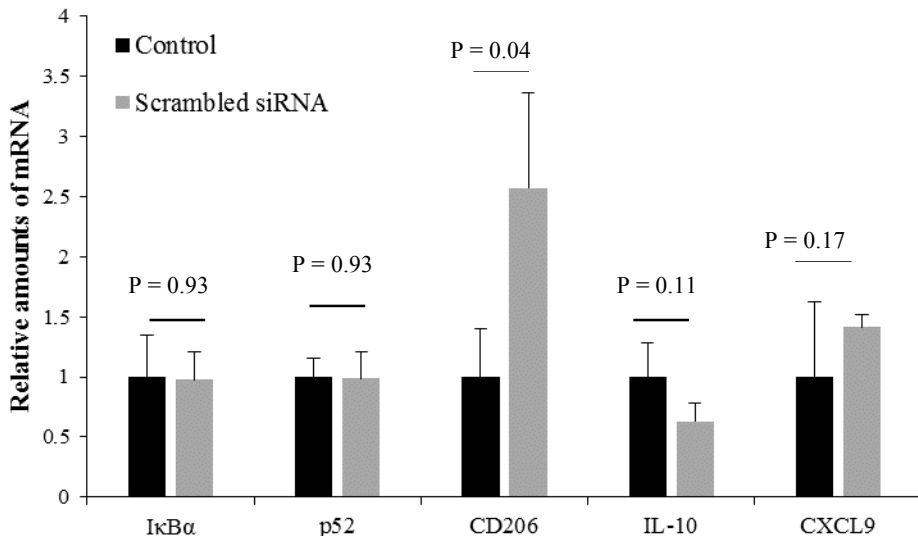


Figure 5: qRT-PCR of scrambled siRNA transfected BMDMs. There is no significant decrease in mRNA levels between the two groups for I κ B α , p52, IL-10 and CXCL9. There is a significant increase in CD206 mRNA following culture with MnNP loaded with a scrambled siRNA sequence. This is consistent with previous reports that activation and endosomal transport of the mannose receptor increases mannose receptor production in macrophages.

Milestone #1: The result of subtasks 1a-1c was the production of a material capable of quantitatively predictable uptake into BMDMs. The result of subtask 1d was the *in vitro* validation and dose-response behavior of siRNA mediated knockdown of the canonical and alternative NF- κ B pathways alone and in combination. The interplay of the canonical and alternative NF- κ B pathways in modulating BMDM phenotype was also assessed. These results have been presented as posters and published in manuscripts listed under reportable outcomes.

Specific Aim 2: Optimize delivery and efficacy of siRNA-delivering nanoparticles to inhibit canonical and alternative NF- κ B, alone and in combination, in macrophages *in vivo*.

2a. Evaluate population distribution of nanoparticles associated with macrophages *in vivo* by flow cytometry. Use the mouse model of metastatic human breast cancer provided by the FVB mice, tail-vein-injected with PyMT mammary tumor cell lines. Macrophage phenotype (M1/M2) will be correlated with high and low particle delivery following flow cytometric cell sorting. [40 FVB mice] (Months 4-8)

2b. Using optimized nanoparticle dosage from tasks 1c and 1d, in combination with *in vivo* delivery results from task 2a, evaluate pharmacokinetics of nanoparticles in NGL-reporter mice with overt lung metastases generated by tail vein injection of Polyoma-derived breast cancer cells using *in vivo* fluorescence imaging. This system enables detection of host response during tumor progression with respect to NF- κ B activity. Use model to further optimize delivery strategy of nanoparticles in terms of dispersibility, accumulation in lung tissue, dose, and duration of treatment. [32 mice] (Months 9-12)

As part of the studies in these sub-aims, we sought to determine the distribution of particles after different types of *in vivo* delivery. To do this, 0.5 million L129 PyMT tumor cells were injected via tail vein into wildtype FVB mice to create overt lung metastases. Cells were allowed to form lung metastases for 2 weeks prior to treatment with MnNP's. Then, whole lungs were removed 6 hrs post-injection from mice receiving MnNP-DNA_Cy5 via intubation (n=2) or via i.v. injection (n=2), and an untreated control mouse. Lungs were perfused and inflated with cold PBS and then imaged for Cy5 fluorescence using a Xenogen IVIS 200 bioluminescent and fluorescent imaging system and Living Image software. Imaging of lungs *ex vivo* shows intubation administration of MnNP results in more than 10 times the Cy5 fluorescence vs intravenous administration of MnNP as visualized 6 hours after delivery (Figure 6B). This image also demonstrates that delivery via intubation is capable of perfusing the MnNP solution throughout the entire lung.

Following this study, we sought to further determine exactly which types of cells within the tumor-bearing lungs the nanoparticles were being delivered to. Direct delivery of nanoparticles via intubation was chosen as the delivery method, given the promising results in our earlier study and in order to mitigate renal and hepatic clearance; a common complication associated with systemic delivery of nanoparticles. 2 weeks after tumor cell injection (via tail vein, to form lung metastases, as above), each mouse was anesthetized with isoflurane and placed on a tilted rodent work stand in the supine position and restrained in position by an incisor loop. The tongue was extruded using forceps, the mouse intubated, and given a 5 mg/kg dose of either MnNP-DNA_Cy5 complexes (n=5) or OHNP-DNA_Cy5 complexes (n=3). Control animals received a 60 ul dose of sterile PBS. After the tubing was removed, the mice were observed until normal respiration resumed. Excised lungs were perfused with sterile PBS and digested to a single cell suspension for flow cytometry. The panel of antibodies used in these experiments included CD45-PE-Cy7 (clone 10-F11), Gr1-Alexa Fluor 700 (clone RB6-8C5), and CD11B-APC (clone M1/70) (all from BD Bioscience). Flow cytometry was performed using a BD LSR II flow cytometer (BD Bioscience) and data were analyzed with FlowJo software (TreeStar). To identify the myeloid cell subset in the lung homogenate, we began by sorting cells based on CD45 expression. To further differentiate cell populations, we sorted cells based on the presence of CD11b and the presence or absence of Gr1. We defined the macrophage population as being CD45⁺/CD11b⁺/Gr1⁻ and both monocytes and polymorphonuclear (PMN) cells as being CD45⁺/CD11b⁺/Gr1⁺. These simple flow panels allowed us to isolate normal macrophages and TAMs from other myeloid cell populations that could potentially uptake delivered nanoparticles through non-specific mechanisms.

Flow cytometry analysis performed 24 hours after particles were delivered via intubation shows that approximately 40% of CD11b⁺ myeloid cells contain DNA_Cy5 formulated with MnNPs (Figure 6C). This population is primarily composed of macrophages and granulocytes with some dendritic cells (DCs) and natural killer (NK) cells. DNA_Cy5 was detected in a relatively small number of non-myeloid cells, on the order of 2% in the same samples of lung homogenate. Furthermore, DNA_Cy5 uptake by CD45⁺/CDllb⁺/Gr1⁺ macrophages is significantly increased in this model through formulation with MnNP as compared with DNA_Cy5 formulated with untargeted OHNP. DNA_Cy5 uptake is not enhanced by mannose presentation on the NP corona in PMN cells and monocytes (CD45⁺/CDllb⁺/Gr1⁺) (Figure 6D); there is no significant difference in DNA_Cy5 delivery between MnNP and OHNP formulations with these cell types. These results are consistent with strong, mannose-dependent delivery to macrophages and weak, non-specific delivery (presumably by phagocytosis) to PMN cells and monocytes. Intubation enables direct access to lung tumor TAMs for NPs, avoiding NP dilution and other challenges resulting from intravascular administration. This data demonstrates that mannose decoration mediates preferential delivery of NPs to TAMs but not non-myeloid cell types that are co-located with the TAMs in this model system.

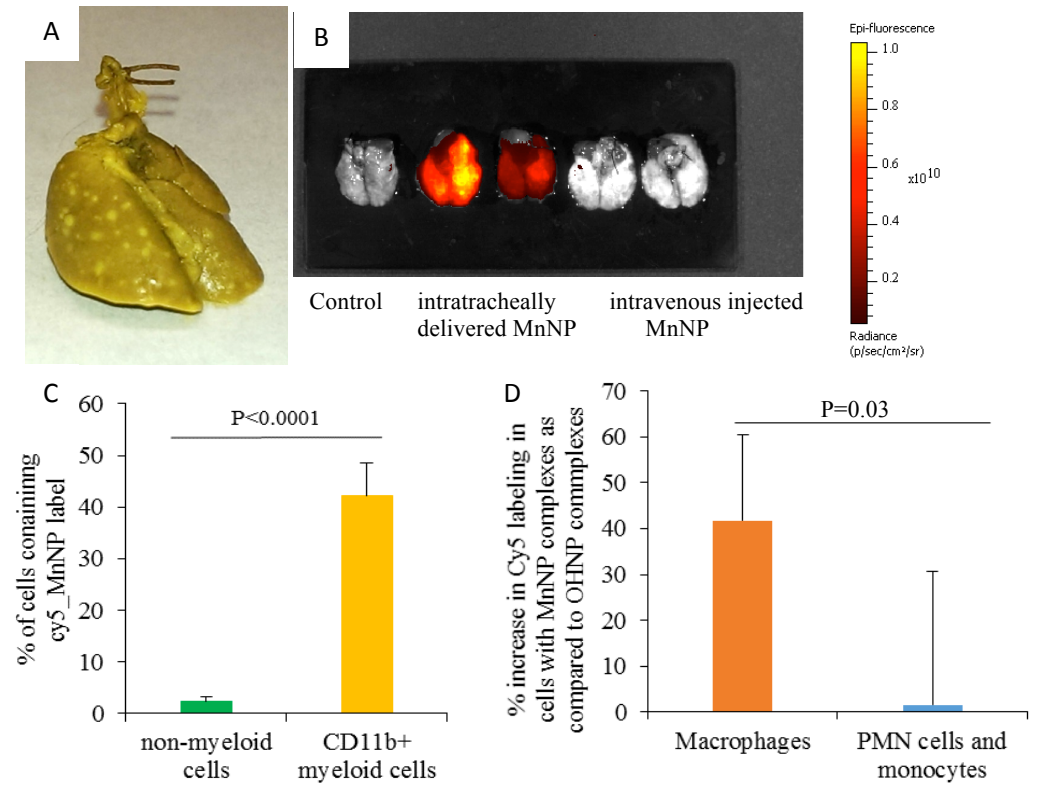


Figure 6: MnNP have enhanced uptake in TAMs associated with mammary lung metastases using an intubation delivery model. (A) Metastases are visualized in the lungs ex vivo following inflation with Bouin's fixative. Tumors appear white against the normal lung, which stains yellow. (B) IVIS imaging of lungs ex vivo shows intubation administration of MnNP results in more than 10 times the Cy5 fluorescence vs intravenous administration of MnNP as visualized 6 hours after delivery. (C) Flow cytometry reveals minimal uptake of MnNP (approximately 2%) in non-myeloid cells. There is significantly more uptake of MnNP in CD11b⁺ myeloid cells. (D) MnNP show 40% increased uptake by macrophages as compared to OHNP. There is no significant difference in nanoparticle uptake between MnNP and OHNP in PMN cells and monocytes.

macrophages is significantly increased in this model through formulation with MnNP as compared with DNA_Cy5 formulated with untargeted OHNP. DNA_Cy5 uptake is not enhanced by mannose presentation on the NP corona in PMN cells and monocytes (CD45⁺/CDllb⁺/Gr1⁺) (Figure 6D); there is no significant difference in DNA_Cy5 delivery between MnNP and OHNP formulations with these cell types. These results are consistent with strong, mannose-dependent delivery to macrophages and weak, non-specific delivery (presumably by phagocytosis) to PMN cells and monocytes. Intubation enables direct access to lung tumor TAMs for NPs, avoiding NP dilution and other challenges resulting from intravascular administration. This data demonstrates that mannose decoration mediates preferential delivery of NPs to TAMs but not non-myeloid cell types that are co-located with the TAMs in this model system.

2c. Functional amendments to the nanoparticle design will be carried out based on *in vivo* pharmacokinetic results of task 2b. The specific changes will be dictated by *in vivo* performance, but may include adjustment of the surface functionalizations for improved biodistribution and/or altered siRNA content per particle to optimize dosing based on achievable administration volumes and frequencies. (Months 10-15)

No functional amendment to the nanoparticle design was deemed necessary. However, in year 2, work funded by other sources in the Giorgio lab, with help from Dr. Craig Duvall, has produced PEG shielded, proximity activated, folate-targeted endosomal escape particles. Briefly, these particles utilize a

shape-engineered PEG layer for biological stealthing as well as a matrix metalloproteinase sensitive proximity activated folate molecule; a particle design that could be implemented in the future with our mannosylated particles.

2d. Using siRNA sequence from task 1d and optimized nanoparticle administration conditions (tasks 2a-2b), assess modulation of NF- κ B activity by luciferase assay and western blots of nuclear extracts from lung tissue containing overt lung metastases to determine translocation of p65 or p52 to the nucleus. In addition, *in vivo* imaging of reporter mice will determine if impact is sufficient to be significant in intact live animals. Determine effects on local macrophage populations by RT-PCR of RNA to quantify expression of target genes correlated with M1 (iNOS, MIP1- α , IL-12) or M2 (IL-10, CCL17, mannose receptor) phenotype. [32 mice] (Months 12-15)

We were able to complete some *in vivo* delivery studies (Aims 2a and b) but were not able to reach our original goal of testing the functional efficacy of modulation of NF- κ B activity.

2e. Isolate TAMs from lung tissue containing overt metastases using anti-CD11 antibody-mediated magnetic separation and assess NF- κ B activity by luciferase assay and westerns, and macrophage phenotype (M1/M2) by RT-PCR. [32 NGL mice] (Months 20-22)

Task 2e was completed in years 1 and 2 (see BC102696P1 annual report 2012 and 2013 for details).

Milestone #2: The result of subtasks 2a-2d was *in vivo* testing of novel multifunctional nanomaterials capable of modulating NF- κ B locally at tumor sites and location reporting by fluorescence imaging. Using the results from this aim, we have produced a manuscript that is under revision and that we are optimistic will be published in *Nanoscale*.

Specific Aim 3: Utilize siRNA-delivering nanoparticles to inhibit classical or alternative NF- κ B activity alone and in combination in macrophages and determine effects on tumor progression.

3a. Optimize generation of PyVT:NGL double transgenics. We currently have breeding colonies of PyVT and NGL transgenics. We have previously generated homozygous NGL transgenics demonstrating the feasibility of this approach. Due to the pathology of the PyVT model, only heterozygous males are competent for breeding. We will generate a breeding colony of PyVT heterozygous:NGL homozygous mice to improve the efficiency of generating experimental animals. [68 mice] (Months 5-8)

Task 3a was completed in years 1 and 2 (see BC102696P1 annual report 2012 and 2013 for details).

3b-d. Were designed to evaluate primary tumor response to treatment by measurement of tumor latency, weight, and size in two dimensions and by immunohistochemical analysis of sections, including assessment of TAM populations (anti-F4/80 antibody), cell proliferation (Ki67 staining), and survival (TUNEL staining). In addition effects of treatment on metastasis to the lungs were to be assessed by quantitation of micrometastases and immunohistochemical analysis of lung tissue sections, including assessment of TAM populations (anti-F4/80 antibody), cell proliferation (Ki67), survival (TUNEL), matrix remodeling (MMP-9 and MMP-12 zymography) and angiogenesis (vWF, VEGF staining). Nanoparticle delivery to both primary tumors and lung metastases were to be assessed by fluorescence microscopy of tumor sections. (Months 15-24).

The overall goals of Aim 3b-d were to combine the transgenics that would have spontaneously arising mammary tumors followed by lung metastasis by approximately 12 weeks with the NGL reporter transgenics and treat these animals *in vivo* with nanoparticles carrying the optimal siRNA with the most efficacious delivery route and timing and then to measure outcome in terms of tumor response in both the primary and lung metastatic sites together with impacts on NF- κ B activity and localized macrophage phenotypes. This was an ambitious goal that we have not succeeded in reaching with this initial funding. We did complete a first step towards these goals by utilizing the PyMT mice to test the *in vivo* efficacy of the TAM-targeted MnNP in this spontaneous tumor model. We delivered MnNP carrying fluorescently-tagged, scrambled DNA strands to the center of the PyMT primary mammary tumors for a well contained depot of particles that would co-localize with TAMs (Figure 7A). We observed no adverse effects of multiple, direct MnNP injections.

Formulation with MnNPs significantly increased DNA_Cy3 delivery to TAMs in murine breast tumors (Figure 7B). Intratumoral injection of a fluorescently labeled DNA mimic of siRNA resulted in nearly 2-fold greater TAM uptake compared to unformulated control DNA_Cy3 administered to another mammary tumor in the same mouse. These data suggest that the MnNP formulation is capable of interacting with TAMs in a persistent way, noting that this study was carried out as three injections, each separated by 24 hours. This demonstrates that injecting MnNPs directly into a primary tumor can successfully deliver nucleic acid material to TAMs. The direct injection approach avoids the potential issues associated with intravascular administration of MnNPs.

Now that this preliminary study has been completed, we will move forward in our future studies by replacing the fluorescent DNA with active siRNA to NF- κ B pathway components and assessing tumor outcomes.

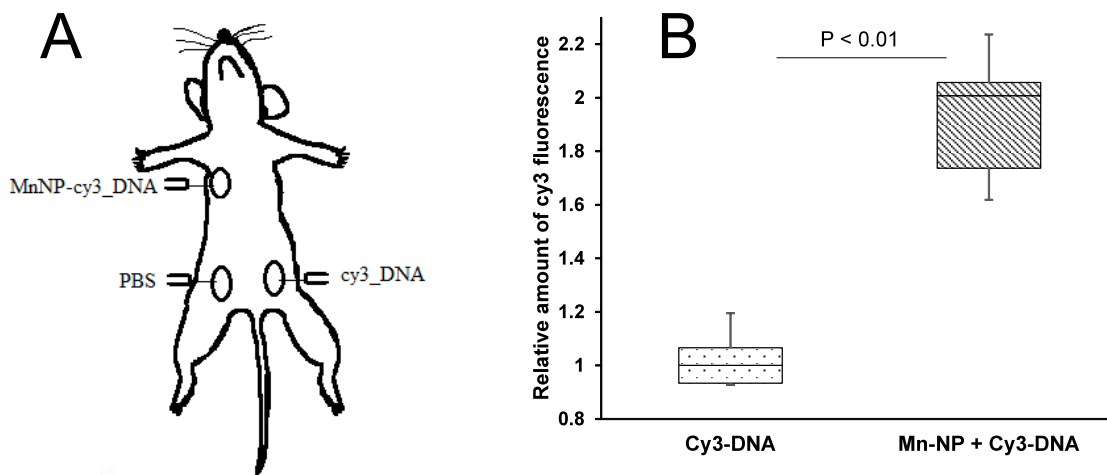


Figure 7: (A) Diagram of mammary tumor injection scheme for PyMT mice. Three isolated tumors from each mouse (N=3) were selected based on uniformity of size and shape. The tumors were injected 3 times, 24 hours apart with MnNP-DNA_Cy3 complexes, free DNA_Cy3, or PBS into the center of each selected tumor. The TAMs were isolated from each tumor and analyzed for cy3 fluorescence. (B) There was a statistically significant increase in Cy3 fluorescence in TAMs from tumors that received MnNP-DNA_Cy3 as compared to non-specific DNA_Cy3 phagocytosis.

Key Research Accomplishments

1. We maintained a highly collaborative and scientifically integrated partnership. We continue to have regular combined group meetings and Ryan Ortega (predoctoral student) represents a direct link between the two groups. This collaborative study is proving educational for members of both research teams and we have developed a shared interest in the progress and outcome of these studies.
2. We generated siRNA-delivering nanoparticles and demonstrated optimized delivery of siRNA into BMDMs *ex vivo* utilizing a mannose receptor targeting approach (Specific Aim 1a-c and Yu et al manuscript).
3. We modified our selection of genes that will be targeted with siRNA based on findings from our studies.
4. We compared the mannosylated nanoparticles to a commercial agent in an *in vitro* test for siRNA delivery and total NF-κB knockdown. The nanoparticle exhibited total NF-κB knockdown similar to the commercial agent.
5. We confirmed the biocompatibility of the nanomaterials both *in vitro* and *in vivo*. The mannosylated nanoparticles are biocompatible with cells at high doses for extended periods of time and are biocompatible in a murine model at doses as high as 5 mg/kg with repeated dosing.
6. We identified a small library of siRNA sequences that are effective at modulating NF-κB activity in bone marrow derived macrophages.
7. We have shown the highly novel result that it is possible to manipulate the NF-κB pathways in an unpredicted fashion: namely activation of the classical pathway by knocking down an inhibitor protein using nanoparticle delivered siRNA. This mechanism of NF-κB manipulation shows high therapeutic potential and merits further investigation.
8. We have isolated mRNA samples from BMDMs and TAMs that have been modulated with our various NF-kappaB component siRNA's. The mRNA will be used to analyze phenotypic differences and similarities between cell populations.
9. We have become proficient in a macrophage isolation protocol that utilizes the rapidly adhesive properties of macrophages to isolate primary macrophages from whole tissue samples. This methodology allows us to isolate these cells without external modification.
10. We have shown that the mannosylated particles are capable of transfecting TAMs more effectively than untargeted, OH- terminated nanoparticles in an *ex vivo* cell culture of mammary TAMs.
11. We have demonstrated the ability of the targeting nanoparticles to deliver nucleic acid material with specificity to TAMs *in vivo* both in primary mammary tumors and in lung metastases.
12. Several grants that would continue this collaboration have been submitted in order to carry on this work.

Conclusion

The ***hypothesis*** to be tested in these studies was that siRNA-mediated inhibition of NF-κB signaling in TAMs could decrease primary tumor growth and metastatic potential. Our ***objectives*** were (1) exploration of macrophage response to inhibition of NF-κB activation by the classical and alternative pathways, separately and in combination using siRNA knockdown *in vitro* and (2) development of a nanobiotechnology delivery vehicle with the capacity for siRNA delivery TAMs for the purpose of pathway-specific NF-κB manipulation *in vivo*.

We have successfully achieved; 1) synthesis and development of the nanoparticles (published), 2) selection of appropriate siRNA (completed), 3) optimization of delivery of nanoparticles (including initial *in vivo* delivery without toxicity and with some specificity to TAMs in both primary tumor and lung

metastases) (revised manuscript submitted). While development and characterization of this novel, targeted nanoparticle siRNA delivery system and identifying the appropriate siRNAs for treatment has been achieved, we have not reached the optimistic goal of demonstrating decreased tumor growth and inhibition of metastasis in a spontaneous *in vivo* tumor model. However, we are now poised to move forward with these efficacy studies and are very actively seeking the funding to support this next vital step.

Publications, Abstracts, and Presentations

1. Ortega RA, Barham W, McFadden ID, Kumar B, Tikhomirov O, Yull FE, Giorgio TD. *In Vivo* Targeting of Tumor Associated Macrophages Using Mannosylated Endosomal-Escape Nanoparticles. Biomedical Engineering Society annual meeting. San Antonio, TX, October 2014. {accepted abstract and podium talk to be given}
2. Ortega RA, Barham W, Kumar B, Tikhomirov O, McFadden ID, Yull FE, Giorgio TD. Biocompatible mannosylated endosomal-escape nanoparticles enhances selective delivery of short nucleotide sequences to tumor associated macrophages. *Nanoscale*. Accepted pending revisions. {scientific manuscript under revision} **[manuscript on appendix pages 18-26]**
3. Ortega RA, Barham W, Tikhomirov O, Sharman K, Yull FE, Giorgio TD. Immunoengineering of tumor associated macrophages using targeted, siRNA delivering nanoparticles. American Association for Cancer Research annual meeting. San Diego, CA, April 2014. { accepted abstract and poster presentation}
4. Ortega RA, Barham W, Tikhomirov O, Kumar B, Yull FE, Giorgio TD: A Targeted Endosomalytic Nanoparticle for Engineering Tumor Immunity in Macrophages. Biomedical Engineering Society Annual Meeting. Seattle, WA, September 2013. {accepted abstract and poster presentation}
5. Ortega RA, Barham W, Kumar B, Yull FE, Giorgio TD: Investigating the Effects of NF- κ B Pathway Modulation in Macrophages using Modular Endosomal Escape Nanoparticles. Cancer Immunotherapy annual meeting. Mainz, Germany, May 2013. {accepted abstract and poster presentation}
6. Yu SS, Lau CM, Barham W, Nelson CE, Li H, Smith CA, Yull FE, Duvall CL, Giorgio TD: Targeting Tumor-Associated Macrophages for Immunotherapy via RNA Interference using Smart, Environmentally-Responsive Nanoparticles. Cancer Immunotherapy annual meeting. Mainz, Germany, May 2013. {accepted abstract and podium talk}
7. Ortega RA, Barham W, Kumar B, Yu SS, Yull FE, Giorgio TD: Reprogramming Tumor Associated Macrophages toward an Anti-Tumor Phenotype by Targeting the NF- κ B Pathway Using Novel Targeted Nanotherapeutics. American Association for Cancer Research annual meeting. Washington, D.C., April 2013. {accepted abstract and poster presentation}
8. Barham W, Tikhomirov O, Chen L, Ortega RA, Gleaves L, Onishko H, Sherrill T, Yu S, Connelly L, Giorgio TD, Blackwell TS, Yull FE: Education of macrophages through modulation of NF- κ B: an opportunity for targeted therapy. American Association for Cancer Research annual meeting. Washington, D.C., April 2013. {accepted abstract and poster presentation}

9. Giorgio TD: Biofunctional nanomaterials for the modulation of macrophage phenotype and polarization. University of Minnesota Department of Biomedical Engineering Invited talk. Minneapolis, MN, April 2013. {invited podium talk}
10. Ortega RA, Barham W, Kumar B, Yull FE, Giorgio TD: Modular, Endosomal-Escape Nanoparticles for the Delivery of Therapeutic Agents to Tumor Associated Macrophages. Tennessee Biomaterials Day annual meeting. Nashville, TN, March 2013. {accepted abstract and podium talk}
11. Yull FE: Macrophage targeting in Benign and Malignant Disease. Vanderbilt University Department of Medicine's Dinner and Data meeting. Nashville, TN, March 2013. {invited podium talk}
12. Giorgio TD: Nanostructure Design for Modulation of Inflammation. Vanderbilt University Department of Medicine's Dinner and Data meeting. Nashville, TN, March 2013. {invited podium talk}
13. Yu SS, Lau CM, Barham WJ, Onishko HM, Nelson CE, Li H, Smith CA, Yull FE, Duvall CL and Giorgio TD: Macrophage-Specific RNA Interference Targeting via 'Click', Mannosylated Polymeric Micelles. Molecular Pharmaceutics. January 2013. {published scientific manuscript} **[manuscript on appendix pages 27-39]**
14. Li H, Duvall CL, Giorgio TD: Tissue specific, proximity-activated, folic acid dual targeting polymeric nanoparticles for siRNA drug carrier. Invention disclosure form to begin patent process.
15. Ortega RA, Barham W, Kumar B, Yull, FE, Giorgio TD: Manipulation of the NF-κB Pathway in Macrophages Using Targeted Nanotherapeutics to Achieve an Anti-Tumor Phenotype. Host-Tumor Interactions Program & Department of Cancer Biology 12th Annual Joint Retreat. Nashville, TN, November 2012. {accepted abstract and poster presentation}
16. Li H, Miteva M, Cheng MJ, Giorgio TD, Duvall CL: Dual MMP-7-Proximity-Activated and Folate Targeted Nanoparticles for siRNA Delivery. Biomedical Engineering Society Annual Meeting. Atlanta, GA, October 2012. {accepted abstract and podium talk}
17. Yu SS, Lau CM, Barham WJ, Nelson CE, Yull FE, Duvall CL, and Giorgio TD: Achieving Cancer Immunotherapy Through RNAi Interference in Tumor-Associated Macrophages via 'Click', Mannosylated Polymeric Nanoparticles. Biomedical Engineering Society Annual Meeting. Atlanta, GA, October 2012. {accepted abstract and podium talk; *winner of the 2012 Design and Research Awards from the Biomedical Engineering Society*}
18. Ortega RA, Kumar B, Yu SS, Yull FE, Giorgio TD: Targeted Knockdown of NF-κB in Tumor Associated Macrophages. Biomedical Engineering Society Annual Meeting. Atlanta, GA, October 2012. {accepted abstract and poster presentation}
19. Barham W, Chen L, Onishko H, Tikhomirov O, Sherrill T, Ortega RA, Connelly L, Blackwell TS, and Yull FE: Education of macrophages through modulation of NF-κB: an opportunity for targeted therapy. MD Anderson Symposium on Cancer Research. Houston, TX, September 2012. {accepted abstract and podium talk}
20. Swartz MA, Lida N, Roberts EW, Sangaletti S, Wong MH, Yull FE, Coussens LM, DeClerk YA: Tumor microenvironment complexity: emerging roles in cancer therapy. Cancer Research. March 2012. {published scientific manuscript} **[manuscript on appendix pages 40-47]**

21. Yu SS, Lau CM, Thomas SN, Jerome WG, Maron DJ, Dickerson JH, Hubbell JA, Giorgio TD: Size- and charge-dependent non-specific uptake of PEGylated nanoparticles by macrophages. International Journal of Nanomedicine. February 2012. {published scientific manuscript} **[manuscript on appendix pages 48-62]**

Inventions, Patents and Licenses

Nothing to report.

Reportable Outcomes

We have developed and tested a nanoparticle formulation that can deliver siRNA to macrophages with some specificity to TAMs both *in vitro* and *in vivo*. We predict that this tool will prove valuable for future studies.

Other Achievements

Employment or research opportunities applied for and/or received based on experience/training supported by this award

1. Lianyi Chen, a research assistant in Fiona Yull's laboratory was partially supported by this award. She gained experience in managing transgenic mouse colonies and in molecular techniques for the analysis of both cell lines and mouse tissue through working on the funded studies. As a result of this experience, she was able to secure a position in the Department of Anesthesiology at Vanderbilt, and was promoted to Research Assistant II.
2. Undergraduate student Cheryl Lau applied to the Graduate School of Georgia Tech based citing research experience gained while working on this project. She was accepted into the Graduate School of Georgia Tech in 2012.
3. Former Graduate Student and current PhD, Shann Yu, obtained his PhD based on work accomplished for this project. He applied for and received a post-doctoral position at the Laboratory of Lymphatic and Cancer Bioengineering at the Ecole Polytechnique Federale de Lausanne in Lausanne, Switzerland based on experience gained while funded by this grant.
4. Graduate Student and Doctoral Candidate Ryan Ortega developed a PhD thesis proposal based on work completed on and experience received from this project. His proposal was accepted by his committee of advisors and by the Graduate School of Vanderbilt University in May, 2013. [thesis proposal on 2013 Annual report pages 227-260; thesis presentation on 2013 Annual report pages 261-281]. Ryan successfully completed his thesis defense with a title of "Immunomodulation of Tumor Associated Macrophages by Targeted, siRNA-Delivering Nanoparticle" on Tuesday July 15th 2014.

Funding applied for based on work supported by this award

1. Fiona Yull. **Targeted activation of macrophages as breast cancer therapy.** NIH, NCI R01 application, submitted October 2012; re-submitted July 2013. Received 14 percentile – not funded.
2. Fiona Yull. **Induction of tumoricidal tumor-associated macrophages as lung cancer therapy.** NIH, NCI R21 application, submitted June 2013.
3. Fiona Yull. **Generation of cytotoxic tumor-associated macrophages by nanoparticle-mediated siRNA delivery as lung cancer therapy.** Department of Defense Lung Cancer Research Program (LCRP) Idea Development Award application, submitted June 2013.
4. Fiona Yull and Todd D. Giorgio. **Nanoparticle-mediated siRNA delivery to tumor-associated macrophages as metastatic breast cancer therapy.** Department of Defense Breast Cancer Research Program (BCRP) Breakthrough Award pre-application, submitted June 2013.
5. Fiona Yull. **Inducing cytotoxic functions of macrophages to limit ovarian tumor progression: Mannose receptor-targeting nanoparticles as siRNA delivery tools.** Department of Defense Ovarian Cancer Research Program (OCRP) Pilot Award application, submitted August 2013.
6. Fiona Yull. **Targeted activation of macrophages to limit ovarian cancer progression.** NIH, NCI R21 application, submitted September 2013. (32 Percentile).
7. Fiona Yull and Todd D. Giorgio. **Immunoengineering of NF-kappaB signaling in tumor associated macrophages: pre-clinical assessment.** Department of Defense Breast Cancer Research Program (BCRP) invited Expansion Award application, submitted January 2014. Not funded.
8. Fiona Yull. **Development of macrophage-based breast cancer therapy.** NIH, NCI R01 application, submitted June 2014 (pending IRG Review).

References

1. Mantovani, A., et al., *Macrophage polarization: tumor-associated macrophages as a paradigm for polarized M2 mononuclear phagocytes*. Trends Immunol, 2002. **23**:549-55.
2. Miselis, N.R., et al., *Targeting tumor-associated macrophages in an orthotopic murine model of diffuse malignant mesothelioma*. Mol Cancer Ther, 2008. **7**:788-99.
3. de Visser, K.E., A. Eichten, and L.M. Coussens, *Paradoxical roles of the immune system during cancer development*. Nat Rev Cancer, 2006. **6**:24-37.
4. Dirkx, A.E., et al., *Monocyte/macrophage infiltration in tumors: modulators of angiogenesis*. J Leukoc Biol, 2006. **80**:1183-96.
5. Murdoch, C., et al., *The role of myeloid cells in the promotion of tumour angiogenesis*. Nat Rev Cancer, 2008. **8**:618-31.
6. Pollard, J.W., *Macrophages define the invasive microenvironment in breast cancer*. J Leukoc Biol, 2008. **84**:623-30.
7. Stout, R.D., et al., *Macrophages sequentially change their functional phenotype in response to changes in microenvironmental influences*. J Immunol, 2005. **175**:342-9.
8. Watkins, S.K., et al., *IL-12 rapidly alters the functional profile of tumor-associated and tumor-infiltrating macrophages in vitro and in vivo*. J Immunol, 2007. **178**:1357-62.
9. Connelly L, Barham W, Onishko HM, Chen L, Sherrill T, Zabuwala T, Ostrowski MC, Blackwell TS, Yull FE. *NF-kappaB activation within macrophages leads to an anti-tumor phenotype in a mammary tumor lung metastasis model*. Breast Cancer Res. 2011; **13**:R83.
10. Cao, Y. and M. Karin, *NF-kappaB in mammary gland development and breast cancer*. J Mammary Gland Biol Neoplasia, 2003. **8**:215-23.
11. Eliopoulos, A.G., et al., *Epstein-Barr virus-encoded latent infection membrane protein 1 regulates the processing of p100 NF-kappaB2 to p52 via an IKKgamma/NEMO-independent signalling pathway*. Oncogene, 2003. **22**(48):7557-69.
12. Perkins, N.D., *Oncogenes, tumor suppressors and p52 NF-kappaB*. Oncogene, 2003. **22**:7553-6.
13. Romieu-Mourez, R., et al., *Roles of IKK kinases and protein kinase CK2 in activation of nuclear factor-kappaB in breast cancer*. Cancer Research, 2001. **61**:3810-8.

Appendices

Appendix materials start with Biographical Sketches for the PIs (Giorgio, Todd D. and Yull, Fiona E.) and the other major personnel contributing to this research effort during the extension year period (July 2013-July 2014)

1. Giorgio, Todd D., Biographical Sketch **[appendix pages 1-5]**
2. Yull, Fiona E., Biographical Sketch **[appendix pages 6-9]**
3. Barham, Whitney J., Biographical Sketch **[appendix page 10]**
4. Ortega, Ryan A., Biographical Sketch **[appendix pages 11-13]**
5. Tikhomirov, Oleg Y., Biographical Sketch **[appendix pages 14-17]**

Following Biographical Sketches, each completed manuscript identified as a 'reportable outcome' for this project is included in appendices. The appendix materials appear in inverse chronological order (newest first) in agreement with the order shown as 'reportable outcomes' and identified below:

6. Ortega RA, Barham W, Kumar B, Tikhomirov O, McFadden ID, Yull FE, Giorgio TD. Biocompatible mannosylated endosomal-escape nanoparticles enhances selective delivery of short nucleotide sequences to tumor associated macrophages. *Nanoscale*. Accepted pending revisions. **[appendix pages 18-26]**
7. Yu SS, Lau CM, Barham WJ, Onishko HM, Nelson CE, Li H, Smith CA, Yull FE, Duvall CL and Giorgio TD: Macrophage-Specific RNA Interference Targeting via 'Click', Mannosylated Polymeric Micelles. *Molecular Pharmaceutics*. January 2013. **[appendix pages 27-39]**
8. Swartz MA, Lida N, Roberts EW, Sangaletti S, Wong MH, Yull FE, Coussens LM, DeClerk YA: Tumor microenvironment complexity: emerging roles in cancer therapy. *Cancer Research*. March 2012. **[appendix pages 40-47]**
9. Yu SS, Lau CM, Thomas SN, Jerome WG, Maron DJ, Dickerson JH, Hubbell JA, Giorgio TD: Size- and charge-dependent non-specific uptake of PEGylated nanoparticles by macrophages. *International Journal of Nanomedicine*. February 2012. **[appendix pages 48-62]**

BIOGRAPHICAL SKETCH

Provide the following information for the Senior/key personnel and other significant contributors.
Follow this format for each person. **DO NOT EXCEED FOUR PAGES.**

NAME Giorgio, Todd D.	POSITION TITLE Professor of Biomedical Engineering, Cancer Biology, and Chemical & Biomolecular Engineering		
eRA COMMONS USER NAME (credential, e.g., agency login) giorgitd	EDUCATION/TRAINING <i>(Begin with baccalaureate or other initial professional education, such as nursing, include postdoctoral training and residency training if applicable.)</i>		
INSTITUTION AND LOCATION	DEGREE <i>(if applicable)</i>	MM/YY	FIELD OF STUDY
Lehigh University, Bethlehem, PA Rice University, Houston, TX	BS PhD	05/82 11/86	Chemical Engineering Chemical Engineering

A. Personal Statement

My work has been motivated by the quantitative understanding of living systems at increasingly refined spatial and temporal scales. Over the last twelve years, the focus of this activity has been in addressing critical problems in understanding and treating cancer and cardiovascular disease. To maximize the potential impact of my work, I have applied basic engineering and science approaches to the study of metastases, the distributed form of cancer most significantly associated with poor five year survival. I have developed a number of new nanoscale materials with biosensing surfaces, including **mannosylated micelles capable of preferential delivery of functional siRNA to macrophages**. The objective has been to **harness the enormous power of macrophage-based immunomodulation through cell-selective delivery**, avoiding the systemic responses that otherwise limit such approaches. As a Department Chair and research principal investigator, I have considerable experience in leading interdisciplinary teams toward successful outcomes. As a mentor, I can provide unique polymeric and nanoscale approaches to the development and assessment of novel biomaterials for use in living systems. I have a substantial devotion to training and education, having served as preceptor to eight postdoctoral associates and 23 graduate degree recipients.

B. Positions and Honors

Positions and Employment

2011 - pres. Professor of Cancer Biology, Vanderbilt University
2008 - pres. Chair, Department of Biomedical Engineering, Vanderbilt University (reappointed 2013)
2007 - 2008 Interim Chair, Department of Biomedical Engineering, Vanderbilt University
2006 - pres. Professor of Biomedical Engineering, Vanderbilt University
2006 - pres. Professor of Chemical and Biomolecular Engineering, Vanderbilt University
2006 - pres. Professor of Materials Science Program, Vanderbilt University
2005 - 2006 Visiting Professor, Integrative Biosciences Institute, École Polytechnique Fédérale de Lausanne
2004 - pres. Member, Vanderbilt-Ingram Cancer Center, Vanderbilt University
2001 - 2006 Associate Professor of Materials Science Program, Vanderbilt University
1996 - 2006 Associate Professor of Biomedical Engineering, Vanderbilt University
1993 - 2006 Associate Professor of Chemical Engineering, Vanderbilt University
1987 - 1993 Assistant Professor of Chemical Engineering, Vanderbilt University

Honors

2014 - Board of Directors, AIMBE
2014 - Chair, AIMBE Academic Council
2012 - Chair, Council of Biomedical Engineering Department Chairs
2011 - Fellow, Biomedical Engineering Society
2009 - Chair, ASGCT Chemical Gene and Cell Therapy Committee
2007 - Fellow, American Institute for Medical and Biological Engineering (AIMBE)
2006 - Member, ASGT Nonviral Gene Transfer Vectors Committee
2003 - Research Paper Competition Award, Vanderbilt Engineering Research Council
2003 - Executive Committee, Vanderbilt Institute for Nanoscale Science and Engineering
2001 - Research Paper Competition Award, Vanderbilt Engineering Research Council

1996 -	Research Paper Competition Award, Vanderbilt Engineering Research Council
1995 -	Elected Councilor, North American Society of Biomechanics (two-year term)
1995 -	Outstanding Teaching Award, Vanderbilt School of Engineering
1994 -	Research Paper Competition Award, Vanderbilt Engineering Research Council
1990 -	Professional Engineer, registration number 021993, State of Tennessee
1990 -	Sigma Xi
1985 -	President, Graduate Student Association, Rice University
1982 -	Engineer-in-Training, Commonwealth of Pennsylvania
1982 -	Tau Beta Pi

Professional Membership

American Association for Cancer Research (AACR); American Institute for Medical and Biological Engineering (AIMBE); American Society of Engineering Educators (ASEE); American Society of Gene and Cell Therapy (ASGCT); Biomedical Engineering Society (BMES); New York Academy of Sciences (NYAS); Sigma Xi (SX)

C. Selected Peer-Reviewed Publications

- Evans BC, Nelson CE, Yu SS, Beavers KR, Kim AJ, Li H, Nelson HM, **Giorgio TD** and Duvall CL: Ex Vivo Red Blood Cell Hemolysis Assay for the Evaluation of pH-responsive Endosomolytic Agents for Cytosolic Delivery of Biomacromolecular Drugs. *Journal of Visualized Experiments* 2013, 73, e50166. doi:10.3791/50166. PMID:23524982
- Li H, Yu SS, Miteva M, Nelson CE, Werfel T, **Giorgio TD**, Duvall CL: Matrix Metalloproteinase Responsive, Proximity-Activated Polymeric Nanoparticles for siRNA Delivery. *Advanced Functional Materials* 2013, 23, 3040-3052. doi:10.1002/adfm.201202215. PMID:None
- Yu SS, Lau CM, Barham WJ, Onishko HM, Nelson CE, Li H, Yull FE, Duvall CL and **Giorgio TD**: Macrophage-Specific RNAi Targeting via 'Click', Mannosylated Polymeric Micelles. *Molecular Pharmaceutics* 2013, 10, 975-987. doi: 10.1021/mp300434e. PMID:23331322
- Zachman AL, Crowder SW, Ortiz O, Zienkiewicz KJ, Bronikowski CM, Yu SS, **Giorgio TD**, Guelcher SA, Kohn JB and Sung HJ: Pro-Angiogenic and Anti-Inflammatory Regulation by Functional Peptides Loaded in Polymeric Implants for Soft Tissue Regeneration. *Tissue Engineering A* 2013, 19, 437-447. doi: 10.1089/ten.tea.2012.0158. PMID:22953721
- Yu SS, Lau CM, Thomas SN, Jerome WG, Maron DJ, Dickerson JH, Hubbell JA and **Giorgio TD**: Size- and Charge-Dependent Non-Specific Uptake of PEGylated Nanoparticles by Macrophages. *International Journal of Nanomedicine* 2012, 7, 799-813. doi:10.2147/IJN.S28531. PMID:22359457
- Ortega RA and **Giorgio TD**: A Mathematical Model of Superparamagnetic Iron Oxide Nanoparticle Magnetic Behavior to Guide the Design of Novel Nanomaterials. *Journal of Nanoparticle Research* 2012, 14, 1282-1293. doi: 10.1007/s11051-012-1282-x. PMID:None
- Gupta MK, Walthal JM, Venkataraman R, Crowder SW, Jung DK, Yu SS, Feaster TK, **Giorgio TD**, Hong CC, Baudenbacher FJ, Hatzopoulos AK and Sung HJ: Combinatorial Electrospun Matrices Promote Physiologically-Relevant Cardiomyogenic Stem Cell Differentiation. *PLoS ONE* 2011, 6, e28935, 1-12. doi:10.1371/journal.pone.0028935. PMID:22216144
- Yu SS, Koblin R, Zachman A, Perrien D, Hofmeister L, **Giorgio TD** and Sung HJ: Physiologically-relevant oxidative degradation of oligo(proline)-crosslinked polymeric scaffolds. *Biomacromolecules* 2011, 12, 4357-4366. doi:10.1021/bm201328k. PMID:22017359
- Yu SS, Ortega RA, Reagan BW, McPherson JA, Sung HJ and **Giorgio TD**: Emerging Applications of Nanotechnology for the Diagnosis and Management of Vulnerable Atherosclerotic Plaques. *WIREs Nanomedicine and Nanobiotechnology* 2011, 3, 620-646. doi: 10.1002/wnan.158. PMID:21834059
- Bell CS, Yu SS and **Giorgio TD**: The MultiStrata Nanoparticle: An AuFeOx Core Enveloped in a Silica-Gold Shell. *Small* 2011, 7, 1158-1162. doi: 10.1002/smll.201002100. PMID:21456084
- Yu SS, Scherer RL, Ortega RA, Bell CS, O'Neil CP, Hubbell JA and **Giorgio TD**: Enzymatic- and temperature-sensitive controlled release of ultrasmall superparamagnetic iron oxides (USPIOs). *Journal of Nanobiotechnology* 2011, 9, 7-16. doi:10.1186/1477-3155-9-7. PMID:21352596
- Sewell SL, Higgins MM, Bell CS and **Giorgio TD**: Quantification of Quantum Dot Concentration Using Inductively Coupled Plasma-Mass Spectrometry (ICP-MS). *Journal of Biomedical Nanotechnology* 2011, 7, 685-690. doi: 10.1166/jbn.2011.1328. PMID:22195486
- Thomas SN, van der Vlies AJ, O'Neil CP, Reddy RT, Yu SS, **Giorgio TD**, Swartz MA, Hubbell JA: Engineering complement activation on polypropylene sulfide vaccine nanoparticles. *Biomaterials* 2011,

32, 2194-3303. doi:10.1016/j.biomaterials.2010.11.037. PMID:21183216

- Soman CP and **Giorgio TD**: Kinetics of Molecular Recognition Mediated Nanoparticle Self-Assembly. Nano Research 2009, 2, 78-84. doi:10.1007/s12274-009-9005-z. PMID:None
- Smith RA and **Giorgio TD**: Quantitative measurement of multifunctional quantum dot binding to cellular targets using flow cytometry. Cytometry A 2009, 75, 465-474. doi:10.1002/cyto.a.20677. PMID:19034921
- Soman CP and **Giorgio TD**: Sensitive and Multiplexed Detection of Proteomic Antigens via Quantum Dot Aggregation. Nanomedicine: Nanotechnology, Biology, and Medicine 2009, 5, 402-409. doi:10.1016/j.nano.2009.01.010. PMID:None
- Sewell SL and **Giorgio TD**: Synthesis and Enzymatic Cleavage of Dual-Ligand Quantum Dots. Materials Science & Engineering C 2009, 29, 1428-1432. doi:10.1016/j.msec.2008.11.015. PMID:None
- Soman CP and **Giorgio TD**: Quantum dot self-assembly for protein detection with femtomolar sensitivity. Langmuir 2008, 24, 4399-4404. doi:10.1021/la704078u. PMID:18335969
- Salaklang J, Steitz B, Finka A, O'Neil CP, Moniatte M, van der Vlies AJ, **Giorgio TD**, Hofmann H, Hubbell JA and Petri-Fink A: Superparamagnetic Nanoparticles as a Powerful Systems Biology Characterization Tool in the Physiological Context. Angewandte Chemie International Edition 2008, 47, 7857-7860. doi:10.1002/anie.200800357. PMID:18792049
- Smith RA, Sewell SL and Giorgio TD: Proximity-activated nanoparticles: In vitro performance of specific structural modification by enzymatic cleavage. International Journal of Nanomedicine 2008, 3, 95-103. PMID:18488420 PMCID: PMC2526364
- Kuhn SJ, Finch SK, Hallahan DE and **Giorgio TD**: Facile production of multivalent enzyme-nanoparticle conjugates. Journal of Magnetism and Magnetic Materials 2007, 311, 68-72. PMID:None
- Kuhn SJ, Finch SK, Hallahan DE and **Giorgio TD**: Proteolytic surface functionalization enhances in vitro magnetic nanoparticle mobility through extracellular matrix. NanoLetters 2006, 6, 306-312. PMID:16464055
- Kuhn SJ, Hallahan DE and **Giorgio TD**: Characterization of superparamagnetic nanoparticle interactions with extracellular matrix in an in vitro system. Annals of Biomedical Engineering 2006, 34, 51-58. PMID:16477503
- Harris SS and **Giorgio TD**: Convective flow increases lipoplex delivery rate to in vitro cellular monolayers. Gene Therapy 2005, 12, 512-520. PMID:15690063
- Smith RA and **Giorgio TD**: Cell-based screening: a high throughput flow cytometry platform for identification of cell-specific targeting molecules. Combinatorial Chemistry and High Throughput Screening 2004, 7, 141-151. PMID:15032661

D. Research Support

Ongoing Research Support

W81XWH-11-1-0344 Giorgio (PI) 07/01/11-06/30/14 (1 year NCE)

Department of Defense

Assessment of Nanobiotechnology-targeted siRNA Designed to Inhibit NF-KappaB Classical and Alternative Signaling in Breast Tumor Macrophages

The research focuses on developing smart nanomaterials to modulate breast cancer development and progression through inhibition of NF- B mediated macrophage activation. Expansion of the current application; no overlap based on expected end/start dates.

Role: Principal Investigator

W81XWH-13-1-0397 Giorgio (PI) 09/30/13-08/31/16

Department of Defense

Using Antibiotics as a Nanoparticle Targeting Motif to Treat Multi-Drug Resistant *Acinetobacter baumannii* Induced Bacteremia in Iraq War Veterans

This work seeks to characterize the materials and methods best suited for bacterial separation from whole blood as an approach to limit the progression of sepsis. No overlap with the current application.

Role: Principal Investigator

W81XWH-13-1-0231 Giorgio (PI) 08/01/13-07/31/15

Department of Defense

High-Intensity Focused Ultrasound for Noninvasive, Controlled Modulation of Immune Response against Breast Cancer in Vivo

This study aims to understand the relationships that control immune stimulation induced by focal, acute thermal injury under controlled conditions. No overlap with the current application.

Role: Principal Investigator

Pending Research Support

BC131239 Giorgio (PI) 10/01/2014-09/30/2016

Department of Defense

Rapid Advancement in Understanding Immunoregulation of Breast Cancer Metastases Through Crowd-Sources, Internet-Based Models

This work aims to create a browser-based graphical model of human cancer immunity to enable interested investigators and consumers the opportunity to test hypotheses using relevant clinical data. No overlap with the current application.

BC131417 Giorgio (PI) 10/01/2014-09/30/2017

Department of Defense

Reactivation of the Anti-Tumor Immune Response in Nanotechnology-Enabled Combination Inhibition of JAK/STAT Signaling in Breast Tumor-Associated Macrophages

This study hypothesizes that IL-6 is a pivotal modulator of breast cancer immunosuppression, proposes nanotechnology-based approaches to modulate IL-6 secretion in the microenvironment and advanced single cell assessments. No overlap with the current application.

BC131417 Giorgio (PI) 10/01/2014-09/30/2019

Department of Defense

Validation and Clinical Translation of a Second-Generation, Breast Cancer Metastasis-Targeted, Combination Therapy Nanocarrier Particle

This work seeks to translate a proteolytic-triggered nanoscale siRNA delivery system to a Phase 0 clinical trial following additional preclinical assessments. No overlap with the current application.

Completed Research Support

W81XWH-10-1-0445 Giorgio (PI) 08/25/10-08/31/12

Department of Defense

Surface Functionalized Nanoparticles for Proximity Activated Targeting of Dual-Mode Therapy for Multidrug Resistant Breast Cancer and Breast Cancer Metastases

The research focuses on the translation of new molecular targeting approaches for the delivery of chemotherapies and gene therapies as treatments for multidrug resistant metastatic breast cancer.
Role: Principal Investigator

W81XWH-10-1-0684 Giorgio (PI) 09/01/10-08/31/12

Department of Defense

Nanomaterials for Modulation of Macrophage Characteristics and Immune Response to Metastatic Breast Cancer

The research focuses on developing smart nanomaterials to modulate macrophage phenotype using IL-4 and induce immune response to breast cancer.

Role: Principal Investigator

BIOGRAPHICAL SKETCH

Provide the following information for the Senior/key personnel and other significant contributors in the order listed on Form Page 2. Follow this format for each person. **DO NOT EXCEED FOUR PAGES.**

NAME Yull, Fiona Elizabeth, D.Phil.	POSITION TITLE Associate Professor of Cancer Biology		
eRA COMMONS USER NAME (credential, e.g., agency login) FIONA_YULL			
EDUCATION/TRAINING (Begin with baccalaureate or other initial professional education, such as nursing, include postdoctoral training and residency training if applicable.)			
INSTITUTION AND LOCATION	DEGREE (if applicable)	MM/YY	FIELD OF STUDY
University of St. Andrews, St. Andrews, UK	B.Sc. (Hons)	1985	Biochemistry w/Microbiology
University of Oxford, Oxford, U.K.	D.Phil.	1989	Biochemistry

A. Personal Statement

I have a longstanding 24-year experience with the design, generation and characterization of multi-mutation transgenic and knockout mice. My group develops murine models to investigate the role of the NF-κB family of transcription factors in disease, particularly cancer. Development of these murine models represents a major investment but we have shared the resulting models with more than 60 groups worldwide, resulting in successful collaborative studies relating to the contribution of NF-κB signaling in several types of cancer including lung, breast, prostate and skin. To address the roles of NF-κB in cancer initiation, promotion and progression we have developed a modular inducible “tool kit” of transgenics. These enable up and down-regulation of canonical NF-κB signaling directed to specific cell types (mammary epithelium, macrophages and lung epithelium) providing the opportunity to address the roles of NF-κB in specific cells in the tumor microenvironment and defined stages of progression. My main interests have been on mammary cancer progression from primary tumor, through metastasis in the circulation to the establishment of final metastatic tumors in a secondary site and on how inflammation contributes to lung cancer. Given the potential for macrophages to play a critical role in cancer progression and our exciting preliminary data, everything is finally in place, apart from funding, to investigate methodologies to modulate NF-κB signaling specifically within macrophages to define exciting new therapeutic approaches.

B. Positions and Honors

Positions and Employment

1985-1989 Predoctoral Fellow under the direction of Drs. A. and S. Kingsman, Oxford University, UK
 1989-1995 Postdoctoral Fellow under the direction of Dr. J. Clark, The Roslin Institute, Roslin, Edinburgh, UK
 1995-1998 Postdoctoral Fellow, Dept. of Microbiology and Immunology, under the direction of Dr. L. Kerr, Vanderbilt University Medical Center, Nashville, Tennessee
 1998-1998 Research Instructor, Dept. of Cell Biology, working with Dr. L. Kerr, Vanderbilt University. Awarded US Army Breast Cancer Research Program Fellowship
 1998-1999 Research Asst. Professor, Dept. of Cell Biology. Acting Principal Investigator during absence of Dr. L. Kerr on Robert Woods Johnson Fellowship in Washington. Awarded American Cancer Society Institutional Research Grant
 2000-2004 Research Assistant Professor, Department of Cancer Biology, Vanderbilt University Medical Center, Nashville, Tennessee
 2004-2010 Assistant Professor of Cancer Biology, Department of Cancer Biology, Vanderbilt University Medical Center, Nashville, Tennessee
 2010-Pres. Associate Professor, Dept. of Cancer Biology, VUMC, Nashville, TN

Other Experience and Professional Memberships

2000-2007 Deputy Director, Department of Medicine PPG Core B
 2003 Deputy Director of Cancer Biology Graduate Course

2004-2006 Reviewer for Susan G Komen Foundation Postdoctoral Fellowships
2004-Pres. Director of Cancer Biology Graduate Course
2007-Pres. Member of Research Safety Subcommittee
2009-Pres. Member of Vanderbilt University IACUC Committee
2010,11,13,14 Ad hoc member, DOD BCRP FY10 Programmatic Review Panel
2011,13 Ad hoc reviewer NIH MESH study section
2012-2014 Member of Editorial Board of ISRN Inflammation
2013,14 Ad hoc reviewer NIH SEP Cancer Health Disparities and Diversity in Basic Cancer Research

1986-Pres. Member of Society of General Microbiology
1997-Pres. Member of Society of Developmental Biology
1998-Pres. Member of American Association of Cancer Research
2012-Pres Member of Metastasis Research Society
2014 Member of International Society for Transgenic Technologies

Honors

2000-2004 Aventis Leadership Development Program Fellow

C. Selected Peer-reviewed Publications (from 71 peer-reviewed publications)

1. Connelly L, Robinson-Benion C, Chont M, Saint-Jean L, Li H, Polosukhin VV, Blackwell TS, Yull FE, A transgenic model reveals important roles for the NF- κ B alternative pathway (p100/p52) in mammary development and links to tumorigenesis. *J Biol Chem.* 282: 10028-35, 2007. PMID: 17261585.
2. Yang J, Splitterber R, Yull FE, Kantrow S, Ayers GD, Karin M, Richmond A. Conditional ablation of IKKB inhibits melanoma tumor development in mice. *J Clin Invest* 120:2563-74, 2010. PMCID: PMC2898608
3. Connelly, L., Barham, W., Pigg, R., Saint-Jean, L., Sherrill, T., Cheng, D-S., Chodosh, L.A., Blackwell, T.S. Yull FE. 2010. Activation of NF- κ B in mammary epithelium promotes milk loss during mammary development and infection. *Journal of Cellular Physiology* 222:73-81. PMCID: PMC2783968.
4. Connelly L, Barham W, Onishko HM, Sherrill T, Chodosh LA, Blackwell TS, Yull FE. Inhibition of NF- κ B activity in mammary epithelium increases tumor latency and decreases tumor burden. *Oncogene* 30:1402-12, 2010. PMCID: PMC3063854
5. Zaynagetdinov R, Stathopoulos GT, Sherrill TP, Cheng DS, McLoed AG, Ausborn JA, Polosukhin VV, Connelly L, Zhou W, Fingleton B, Peebles RS, Prince LS, Yull FE, Blackwell TS. Epithelial nuclear factor-B signaling promotes lung carcinogenesis via recruitment of regulatory T lymphocytes. *Oncogene*. 2012; 31: 3164-76. PMID: 22002309. PMCID: PMC3266969.
6. Zaynagetdinov R, Sherrill TP, Polosukhin VV, Han W, Ausborn JA, McLoed AG, McMahon FB, Gleaves LA, Degryse AL, Stathopoulos GT, Yull FE, Blackwell TS. A critical role for macrophages in promotion of urethane-induced lung carcinogenesis. *J Immunol.* 2011; 187:5703-11. PMID: 22048774. PMCID: PMC3221921.
7. Blackwell, TS, Hipps, AN, Yamamoto, Y, Han, W, Barham, WJ, Ostrowski, MC, Yull, FE, Prince, LS. NF- κ B Signaling in Fetal Lung Macrophages Disrupts Airway Morphogenesis. *J Immunol.* 2011; 187:2740-7. PMID: 21775686. PMCID: PMC3159744.
8. Connelly L, Barham W, Onishko HM, Chen L, Sherrill T, Zabuwala T, Ostrowski MC, Blackwell TS, Yull FE. NF- κ B activation within macrophages leads to an anti-tumor phenotype in a mammary tumor lung metastasis model. *Breast Cancer Res.* 13:R83. 2011. PMID: 21884585. PMCID: PMC3236346.
9. Swartz MA, Iida N, Roberts EW, Sangaletti S, Wong MH, Yull FE, Coussens LM, Declerck YA. Tumor Microenvironment Complexity: Emerging Roles in Cancer Therapy. *Cancer Res.* 2012; 72: 2473-80. PMID: 22414581. PMCID: PMC3653596.
10. Barham W, Sherrill T, Connelly L, Blackwell TS, Yull FE. Intraductal Injection of LPS as a Mouse Model of Mastitis: Signaling Visualized via an NF- B Reporter Transgenic. *J Vis Exp.* (67). pii: 4030. 2012. PMID:22971993. PMCID: PMC3490260.
11. Han W, Li H, Cai J, Gleaves LA, Polosukhin VV, Segal BH, Yull FE, Blackwell TS. 2013. NADPH Oxidase Limits Lipopolysaccharide-Induced Lung Inflammation and Injury in Mice through Reduction-Oxidation Regulation of NF- B Activity. *J Immunol* 190:4786-94. PMID:23530143 PMCID: PMC3633681

12. Yu SS, Lau CM, Barham WJ, Onishko HM, Nelson CE, Li H, Smith CA, Yull FE, Duvall CL, Giorgio TD. Macrophage-Specific RNAi Targeting via 'Click', Mannosylated Polymeric Micelles. *Mol Pharm.* 2013; 10:975-87. PMID: 23331322 PMCID: PMC3595119.
13. Stouch AN, Zaynagetdinov R, Barham WJ, Stinnett AM, Slaughter JC, Yull FE, Hoffman HM, Blackwell TS, Prince LS. I β kinase activity drives fetal lung macrophage maturation along a non-M1/M2 paradigm. *J Immunol.* 2014; 193:1184-93. PMID: 24981452. PMCID: PMC4108541.
14. Jin R, Yi Y, Yull FE, Blackwell TS, Clark PE, Koyama T, Smith JA Jr, Matusik RJ. NF- κ B gene signature predicts prostate cancer progression. *Cancer Res.* 2014; 74:2763-72. PMID: 24686169. PMCID: PMC4024337.
15. Barham W, Frump AL, Sherrill TP, Garcia CB, Saito-Diaz K, VanSaun MN, Fingleton B, Gleaves L, Orton D, Capecchi MR, Blackwell TS, Lee E, Yull F, Eid JE. Targeting the Wnt pathway in synovial sarcoma models. *Cancer Discov.* 2013; 3:1286-301. PMID: 23921231. PMCID: PMC3823757.

D. Research Support

Ongoing Research Support

1 R01 HL 116358-01 (Blackwell/Prince, Co-PI's)

09/25/12 - 06/30/15

NIH/NHLBI

Imaging Activated Macrophages in the Lungs

Lung macrophages are critical for initiating the innate immune response to microbial and environmental stimuli, resolving acute inflammation, and promoting repair following injury. We hypothesize that developing molecular imaging techniques to identify functional subsets of activated macrophages will advance understanding of inflammatory lung diseases leading to novel, macrophage-targeted therapies. We will optimize imaging probes based on FR κ B expression exploring new imaging targets present on the surface of activated macrophages. These new strategies can then be applied to the study of inflammatory lung diseases in humans.

5 R01 HL 085317 (Blackwell)

04/01/12 - 02/28/16

NIH/NHLBI

“Epithelial-Fibroblast Interactions in Lung Fibrosis”

Goal: Use novel mouse models to test the hypothesis that specific phenotypic alterations in alveolar epithelial cells affect the response to injurious stimuli, impact fibroblast activation, and determine the severity and progression of lung fibrosis. Aims: To define the extent of epithelial-mesenchymal transition as a source of fibroblasts in experimental pulmonary fibrosis. We will determine the proportion of lung fibroblasts derived from epithelium via EMT and examine the phenotypic characteristics of epithelial-derived fibroblasts.

VA MERIT (Richmond)

10/01/13-9/30/2017

Department of Veterans Affairs

“Modeling New Therapeutic Approaches for Malignant Melanoma”. Specific aims: 1) Characterize effectiveness of combined therapy with the MDM2 antagonist, Nutlin-3a, and the AURKA inhibitor, MLN8237, for treatment of BRAF WT /p53 WT , NRas mutant/p53 WT , NRas WT /p53 WT Melanoma and examine the effect of the Nutlin-3a and MLN8237 combination treatment on the growth of BRAF $V600$ mutant /p53 WT melanoma tumor implants from patients with resistance to BRAF inhibitor. 2) Characterize effects of combined treatment with Nutlin-3a and MLN8237 on tumor microenvironment and on melanoma metastasis and to evaluate the potential for boosting the antitumor response of myeloid cells to enhance melanoma tumor cell death in association with MLN8237 and Nutlin-3a. Express constitutively active IKK κ B in myeloid cells to induce an antitumor phenotype and evaluate the response of melanoma tumors to therapy with MLN8237 and Nutlin-3a. 3) To characterize the therapeutic effectiveness of combining agonist for death receptors DR4 and DR5 with MLN8237 for treatment of BRAF WT , NRAS WT or NRAS mutant melanoma tumors and to evaluate the effectiveness of combined DR5/DR4 agonists with MLN-8237 for BRAF inhibitor resistant BRAF $V600$ melanoma.

Recently Completed

W81XWH-11-1-0242 (Yull Partnering PI) Department of Defense Assessment of nanobiotechnology-Targeted siRNA Designed to Inhibit NF-kappaB Classical and Alternative signaling in Breast Tumor Macrophages Goals are; 1) exploration of macrophage response to inhibition of NF- κ B activation by the canonical and alternative pathways using siRNA <i>in vitro</i> , 2) develop nanobiotechnology delivery vehicle for specific delivery of siRNA to tumor associated macrophages <i>in vivo</i> to modulate NF- κ B activity.	07/01/11-06/30/13 (No cost extension – 06/30/14)
W81XWH-11-1-0509 (Wilson) Department of Defense Nuclear factor-kappaB Activity in the Host-tumor Microenvironment of Ovarian Cancer Study the patterns of NF- κ B activity in the host versus the tumor epithelium during progression of ovarian cancer in a murine model. Bioluminescent reporters in ovarian cancer cell lines or transgenic mice will determine patterns of NF- κ B activity and responses to pharmacologic interventions during tumor progression.	07/25/11-08/24/13 (No cost extension – 08/24/14)
5 R01 HL 097195-02 (Prince) NIH/NHLBI Role of Fetal Lung Macrophages in Bronchopulmonary Dysplasia Goal: This proposal tests the role of fetal lung macrophages in bronchopulmonary dysplasia pathogenesis. Specifically, we will test if macrophages are required for inhibition of normal lung development by innate immune stimuli, if NF- κ B activation in macrophages mediates global fetal lung inflammation, and how early exposure of fetal lung macrophages to inflammatory stimuli alters macrophage phenotype as lungs mature. Aims: To identify role of NF- κ B in inhibition of lung development following innate immune activation. Determine if early activation of fetal lung macrophages alters the macrophage phenotype as lungs mature.	09/14/09 - 07/31/14
5 R01 CA 113734-05 (Yull) NIH/NCI Epithelial NF-KappaB Signaling in Mammary Tumorigenesis Goal: The proposed project will define the role of NF-kappaB signaling as a master regulator of these processes, integrating multiple processes and thereby determining ultimate physiological outcome. Aims: Evaluate effects of modulation of NF- κ B activity in mammary epithelium on mammary development. Use a number of existing and novel transgenic and knockout mice to investigate the differential effects of increasing or decreasing NF- κ B activity in the mammary epithelium or of over-expressing p100/p52 a family member correlated with human mammary adenocarcinoma on mammary development.	07/01/07 - 05/31/12 (No cost extension – 05/31/13)
5 R01 CA 076142-14 (Matusik) NIH/NCI Transgenic Animal Models for Prostate Cancer Goal: The overall goal of this proposal is to study the pathways that contribute to prostate tumor progression to castrate resistant prostate cancer (CRPC). Aims: To determine the contribution of Pten and NF- κ B signaling to AR action <i>in vitro</i> . The proposed research of this aim is to identify targets in the prostate for therapeutic intervention and to understand the mechanism whereby NF- κ B activation results in castrate resistant prostatic cells.	08/11/09 – 06/30/13
Overlap: There is no overlap between the currently funded grants listed above and this application. If all of Dr. Yull's pending proposals are approved and funded, Dr. Yull will adjust her effort so as not to exceed the maximum allowed.	

BIOGRAPHICAL SKETCH

NAME Barham, Whitney Jo	POSITION TITLE Research Assistant II		
INSTITUTION AND LOCATION Rhodes College	DEGREE (if applicable) B.S. (Hons.)	YEAR(s) 2004-2008	FIELD OF STUDY Chemistry(Biochemistry)

A. Positions and Honors

2005-2008 Teaching Assistant, Rhodes College Chemistry Department. Mentor Dr. D. Jeter, Rhodes College, Memphis, TN

2007-2008 Undergraduate Research Assistant, Dept. Pharmacology. Mentor Dr. Leonard Lothstein, University of Tennessee Health Science Center (UTHSC), Memphis, TN.

2008-Pres Research Assistant, Dept. Cancer Biology. Principal Investigator Fiona Yull, Vanderbilt University Medical Center (VUMC), Nashville, TN

B. Peer-reviewed publications in chronological order.

1. Connelly, L., **Barham, W.**, Pigg, R., Saint-Jean, L., Sherrill, T., Cheng, D-S., Chodosh, L.A., Blackwell, T.S. Yull, F.E. Activation of NF-kappaB in mammary epithelium promotes milk loss during mammary development and infection. *Journal of Cellular Physiology* 2010. 222:73-81. PMID: 19746431. PMCID: PMC2783968.
2. Connelly, L., **Barham, W.**, Onishko, H.M., Sherrill, T., Chodosh, L.A., Blackwell, T.S., Yull, F.E. Inhibition of NF-kappaB activity in mammary epithelium increases tumor latency and decreases tumor burden. *Oncogene* 2011. 30(12):1402-12. PMID: 21076466. PMCID: PMC3063854.
3. Blackwell, T.S., Hipps, A.N., Yamamoto, Y., **Barham, W.J.**, Ostrowski, M.C., Yull, F.E., Prince, L.S. NF- B signaling in fetal lung macrophages disrupts airway morphogenesis. *Journal of Immunology* 2011. 187(5):2740-7. PMID: 21775686. PMCID: PMC3159744.
4. Connelly, L.*., **Barham, W.***, Onishko, H.M., Chen, L., Sherrill, T.P., Zabuawala, T., Ostrowski, M.C., Blackwell, T.S., and Yull, F.E. NF-kappaB activation within macrophages leads to an anti-tumor phenotype in a mammary tumor lung metastasis model. *Breast Cancer Research* 2011. 13(4):R83. PMID: 21884585. PMCID:PMC3236346. (*these authors contributed equally).
5. **Barham, W.**, Sherrill, T., Connelly, L., Blackwell, T.S., Yull, F.E. Intraductal injection of LPS as a mouse model of mastitis: signaling visualized via an NF- B reporter transgenic. *Journal of Visualized Experiments* 2012. 4(67):e4030. doi: 10.3791/4030. PMID: 22971993. PMCID: PMC3490260
6. Yu, S.S., Lau, C.M., **Barham, W.J.**, Onishko, H.M., Nelson, C.E., Li, H., Smith, C.A., Yull, F.E., Duvall, C.L., Giorgio, T.D. Macrophage-specific RNA interference targeting via “click”, mannosylated polymeric micelles. *Molecular Pharmacology* 2013. 4;10(3):975-87. PMID: 23331322. PMCID: PMC3595119.
7. **Barham, W.**, Frump, A.L., Sherrill, T.P., Garcia, C. B., VanSaun, M.N., Fingleton, B., Gleaves, L., Orton, D., Capecchi, M.R., Blackwell, T.S., Lee, E., Yull, F.E., Eid, J.E. Targeting the Wnt Pathway in Synovial Sarcoma Models. *Cancer Discovery* 2013. 3(11):1286-301. PMID: 23921231.
8. Wilson AJ, **Barham W**, Saskowski J, Tikhomirov O, Chen L, Lee HJ, Yull F, Khabele D. Tracking NF- B activity in tumor cells during ovarian cancer progression in a syngeneic mouse model. *Journal of Ovarian Research* 2013. 6(1):63. PMCID: PMC3846584.
9. Stouch AN, Zaynagetdinov R, **Barham WJ**, Stinnett AM, Slaughter JC, Yull FE, Hoffman HM, Blackwell TS, and Prince LS. IkB kinase activity drives fetal lung macrophage maturation along a non-M1/M2 paradigm. *Journal of Immunology* 2014. 193(3):1184-93. PMCID: PMC4108541.

BIOGRAPHICAL SKETCH

Provide the following information for the key personnel and other significant contributors in the order listed on Form Page 2.
Follow this format for each person. **DO NOT EXCEED FOUR PAGES.**

NAME Ryan Ortega	POSITION TITLE Graduate Student Researcher
eRA COMMONS USER NAME	

EDUCATION/TRAINING (Begin with baccalaureate or other initial professional education, such as nursing, and include postdoctoral training.)			
INSTITUTION AND LOCATION	DEGREE (if applicable)	YEAR(s)	FIELD OF STUDY
Vanderbilt University	B.E.	2004-2008	Biomedical Engineering
Vanderbilt University	M.S.	2008-2010	Biomedical Engineering
Vanderbilt University	Ph.D.	2014 (expected)	Biomedical Engineering

A. Positions and Honors.**Positions and Employment**

2013-2014	Teaching Affiliate at the Vanderbilt Center for Teaching
2008-present	Graduate Student Researcher at Vanderbilt University Department of Biomedical Engineering, working with Dr. Todd D. Giorgio in Bionanotechnology
2011-present	Graduate Student Researcher at Vanderbilt Medical Center Department of Cancer Biology, working with Dr. Fiona Yull in Cancer Immunology
2007-2008	Undergraduate Student Researcher at Vanderbilt University Department of Biomedical Engineering, working with Dr. V. Prasad Shastri in tissue engineering and biomaterials.
2005	Undergraduate Student Researcher at Vanderbilt University Department of Molecular Biology, working with Dr. D. J. Funk in speciation and evolutionary biology.

Honors

2008-2013	Provost's Graduate Fellowship, Vanderbilt University
2008	Graduated <i>cum laude</i> , Vanderbilt University
2004-2008	Chancellor's Scholar, Vanderbilt University

B. Selected peer-reviewed publications (in reverse chronological order).

R.A. Ortega, T.E. Yankeelov, T.D. Giorgio. Magnetic nanoparticles in magnetic resonance imaging: a translational push toward theranostics. Ed. R. Bawa, G. F. Audette, I. Rubinstein. Handbook of Clinical Nanomedicine – From Bench to Bedside. Pan Stanford Series in Nanomedicine, Pan Stanford Publishing, Singapore, 2015.

R.A. Ortega and T.D. Giorgio. A Mathematical Model of Superparamagnetic Iron Oxide Nanoparticle Magnetic Behavior to Guide the Design of Novel Nanomaterials. *Journal of Nanoparticle Research.* 14: 1282. 2012.

S.S. Yu, R.A. Ortega, B.W. Reagan, J.A. McPherson, H.J. Sung, T.D. Giorgio. Emerging applications of nanotechnology for the diagnosis and management of vulnerable atherosclerotic plaques. *WIREs Nanomedicine and Nanobiotechnology.* 3:6. 2011

S.S. Yu, R.L. Scherer, R.A. Ortega, C.S. Bell, C.P. Soman, C.P. O'Neil, J.A. Hubbell, and T.D. Giorgio.

Enzymatic- and temperature-sensative controlled release of ultrasmall superparamagnetic iron oxides (USPIOs). *Journal of Nanobiotechnology*. 9:7. 2011.

T. Soike, A.K. Streff, C. Guan, R. Ortega, M. Tantawy, C. Pino, V.P. Shastri. Engineering a Material Surface for Drug Delivery and Imaging using Layer-by-Layer Assembly of Functionalized Nanoparticles. *Adv. Mater.* 22, 1392-1397. 2010.

C. Talks

R.A. Ortega, W. Barham, B. Kumar, F.E. Yull, T.D. Giorgio. Modular, Endosomal-Escape Nanoparticles for the Delivery of Therapeutic Agents to Tumor Associated Macrophages. *Tennessee Biomaterials Day annual meeting*. Nashville, TN, March 2013.

R.A. Ortega, T.D. Giorgio. A New Model of Iron Oxide Nanoparticle Magnetic Properties to Guide Design of Novel Nanomaterials. *Biomedical Engineering Society annual meeting*. 2010.

D. Posters

R.A. Ortega, W. Barham, O. Tikhomirov, K. Sharman, F.E. Yull, T.D. Giorgio. Immunoengineering of tumor associated macrophages using targeted, siRNA delivering nanoparticles. *American Association for Cancer Research annual meeting*. San Diego, CA, April 2014.

R.A. Ortega, W. Barham, O. Tikhomirov, B. Kumar, F.E. Yull, T.D. Giorgio. A Targeted Endosomalytic Nanoparticle for Engineering Tumor Immunity in Macrophages. *Biomedical Engineering Society Annual Meeting*. Seattle, WA, September 2013.

R.A. Ortega, W. Barham, B. Kumar, F.E. Yull, T.D. Giorgio. Investigating the Effects of NF- B Pathway Modulation in Macrophages using Modular Endosomal Escape Nanoparticles. *Cancer Immunotherapy annual meeting*. Mainz, Germany, May 2013.

R.A. Ortega, W. Barham, B. Kumar, S.S. Yu, F.E. Yull, T.D. Giorgio. Reprogramming Tumor Associated Macrophages toward an Anti-Tumor Phenotype by Targeting the NF- B Pathway Using Novel Targeted Nanotherapeutics. *American Association for Cancer Research annual meeting*. Washington, D.C., April 2013.

R.A. Ortega, B. Kumar, S.S. Yu, T.D. Giorgio. Targeted Knockdown of NF- B in Tumor Associated Macrophages. *Biomedical Engineering Society annual meeting*. Atlanta, GA, October 2012

C.S. Bell, A. Stevenson, R.A. Ortega, T.D. Giorgio. Biomagnetophotonic Mutilayered Metalldielectric Nanoparticles for Theranostic Applications. *Biomedical Engineering Society annual meeting*. Atlanta, GA, October 2012

R.A. Ortega, S.S. Yu, T.D. Giorgio. Improving early detection of breast cancer metastases with enhanced magnetic resonance imaging using cross-linked iron oxide nanoparticle clusters. *Era of Hope breast cancer meeting*. 2011.

R.A. Ortega, S.S. Yu, T.D. Giorgio. Modeling the magnetic properties of superparamagnetic iron oxide nanoparticles arranged in ordered clusters. *Tennessee Biomaterials Day annual meeting*. Memphis, TN, 2011.

E. Research Support

Completed Research Support

BC102696 Giorgio (PI) Yull (co-PI) 7/1/2011 – 6/30/2014
Assessment of Nanobiotechnology-Targeted siRNA Designed to Inhibit NF-KappaB Classical and Alternative Signaling in Breast Tumor Macrophages
This work seeks to achieve targeted knock down of key proteins in the NF- κ B pathway to repurpose tumor associated macrophages to adopt of tumor killing phenotype.

BC076499 Giorgio (PI) 7/1/2008 – 9/25/2010
Improving Early Detection of Breast Cancer Metastases with Enhanced Magnetic Resonance Imaging Using Novel, Cross-Linked Iron Oxide Nanoparticle Clusters
This work attempted to synthesize and characterize a novel bio-responsive nano-composite for early breast cancer and metastasis detection by magnetic resonance (MR) imaging.

CURRICULUM VITAE

OLEG Y. TIKHOMIROV

Professional Address: B3302 MCN, Vanderbilt University, Vanderbilt University School of Medicine, Nashville, TN, 37232

Telephone:

E-mail: oleg.tikhomirov@vanderbilt.edu

Education: M.D., 2^d Moscow State Medical Academy, Moscow, Russia, 1975-1982

Professional Experience:

2011-present Research Instructor, Department of Cancer Biology, Vanderbilt University

2008-2011 Research Assistant Professor, Vanderbilt University School of Medicine, Department of Biochemistry

2005-2008 Research Assistant Professor, Vanderbilt University School of Medicine, Department of Medicine, Division of Hematology/Oncology

2003-2005 Research Assistant Professor, Vanderbilt University School of Medicine, Department of Biochemistry

2002-2003 Research Instructor, Vanderbilt University School of Medicine, Department of Biochemistry

1997-2002 Research Fellow, Vanderbilt University School of Medicine, Department of Biochemistry

1995-1997 Research Fellow, Vanderbilt University Medical Center, Department of Medicine, Division of Rheumatology and Immunology.

1989-1994 Researcher, Institute of Experimental Cardiology, Cardiology Research Center, Moscow, Russia

1986-1988 Researcher, Institute of Agricultural Biotechnology, Moscow, Russia

1985-1986 Junior Researcher, Institute of Epidemiology, Moscow, Russia

1982-1985 Microbiologist, Mechnikov Institute of Vaccine and Sera, Moscow, Russia

PUBLICATIONS

1. Ermolin G.A., Dikov M.M., Tikhomirov O.Y. Enzyme immunoassay in evaluation of homeostasis and diagnostics of its disorders. In: New in Cardiology. (ed. Chazov E.I.) Moscow, Vneshtorgizdat, 1985, 141-144.
2. Tikhomirov O.Yu., Ermolin G.A., Dikov M.M. Detection of myoglobin by enzyme immunoassay. USSR Pharm. Art. 42-39BC-1986.
3. Efremov E.E., Ermolin G.A., Dikov M.M., Tikhomirov O.Y. Detection of fibronectin by enzyme immunoassay. USSR Pharm. Art. 42-28BC-1986.
4. Ermolin G.A., Tikhomirov O.Y., Dikov M.M. Detection of fibrinogen and fibrin-fibrinogen degradation products by enzyme immunoassay. USSR Pharm Art. 42-37BC-1986.
5. Ermolin G.A., Shelepova T.M., Dikov M.M., Tikhomirov O.Y. Application of enzyme immunoassay for detection of myoglobin, fibronectin, fibrinogen and fibrin-fibrinogen degradation products in diagnostics of somatic diseases. Bull. Cardiol. Cent USSR(1):33-37, (1987).
6. Plaksin D.Yu., Ermolin G.A., Dikov M.M., Tikhomirov O.Y. Ultramicromethod of erythrocytes immunoabsorption in screening for somatic antigens in acute myocardial infarction. Bull. Cardiol. Cent USSR(2):21-25, (1987).
7. Dikov M.M., Tikhomirov O.Y., Ratner G.M., Ermolin G.A. Detection of antibodies to myoglobin by enzyme immunoassay. USSR Pharm. Art. 42-17BC-1991.
8. Dikov M.M., Tikhomirov O.Y., Ratner G.M. Detection of insulin and antibodies to insulin by enzyme immunoassay. USSR Pharm Art. 42-86BC-1992.
9. Lakeev Iu.V., Kosykh V.A., Kozenkov E.I., Tsibul'skii V.P., Tikhomirov O.Y., Antonov I.A., Repin V.S. Probucol and alpha-tocopherol stimulate the synthesis of bile acids in cultured rabbit hepatocytes. Biochemistry (Moscow) (1993), 58(3): 406-415.

10. Kazantseva I.A., Kalinin A.P., Polyakova G.A., Davydova I.Y., Tikhomirov O.Yu. A retrospective clinico-morphologic study of insulinoma. *Arkhiv Patologii USSR* (1995), 57(3): 31-35.
11. Khaspekova S.G., Byzova T.V., Lukin V.V., Tikhomirov O.Y., Berndt M., Kouns W., Mazurov A.V. Conformational changes of the platelet membrane glycoprotein IIb-IIIa complex stimulated by a monoclonal antibody to the N-terminal segment of glycoprotein IIIa. *Biochemistry (Moscow)* (1996), 61(3): 412-428.
12. Mazurov A.V., Khaspekova S.G., Byzova T.V., Tikhomirov O.Y., Berndt M.C., Steiner B., Kouns W.C. Stimulation of platelet glycoprotein IIb-IIIa (alpha IIb beta 3-integrin) functional activity by a monoclonal antibody to the N-terminal region of glycoprotein IIIa. *FEBS Letters* (1996), 391(1-2): 84-88.
13. Tsibulsky V.P., Yakushkin V.V., Tikhomirov O.Y., Preobrazhensky S.N. Immunoenzyme assessment of human apoB-lipoprotein binding to immobilized receptor of low density lipoproteins. 1. Preparation of anti-receptor monoclonal antibodies. *Biochemistry* (1997), 62(6): 596-602.
14. Tikhomirov O.Y., Thomas J.W. Restricted V gene repertoire in the secondary response to insulin in young BALB/c mice. *Journal of Immunology* (1997), 158(9): 4292-4300.
15. Semenov A.V., Romanov Y.A., Loktionava S.A., Tikhomirov O.Y., Khachikian M.V., Vasil'ev S.A., Mazurov A.V. Production of soluble P-selectin by platelets and endothelial cells. *Biochemistry (Moscow)* (1999), 64(11): 1326-35.
16. Tikhomirov O.Y., Thomas J.W. Alanine scanning mutants of rat proinsulin I show functional diversity of antiinsulin monoclonal antibodies. *Journal of Immunology* (2000), 165(7): 3876-82.
17. Tikhomirov O.Y., Thomas J.W. Preference for IgG mAb binding insulin in solution or on surfaces is related to immunoglobulin variable region structures. *Journal of Autoimmunity* (2000), 10(6): 541-549.
18. Tikhomirov O., Carpenter G. Geldanamycin induces ErbB-2 degradation by proteolytic fragmentation. *The Journal of Biological Chemistry* (2000), 275(34): 26625-31.
19. Tikhomirov O., Carpenter G. Caspase-dependent cleavage of ErbB-2 by geldanamycin and staurosporin. *The Journal of Biological Chemistry* (2001), 276(36): 33675-33680.

20. Tikhomirov O., Carpenter G. Identification of ErbB-2 kinase domain motifs required for geldanamycin-induced degradation. *Cancer Research* (2003), 63, 39-43.
21. Tikhomirov O., Carpenter G. Epidermal growth factor (EGF) signaling. In: "Encyclopedia of hormones and related cell regulators" (H.L.Henry and A.W. Norman, eds), Academic Press (2003), Vol.I, 549-556.
22. Qiu-Chen Cheng, Tikhomirov O., Zhou W., Carpenter G. Ectodomain cleavage of ErbB-4: Characterization of the cleavage site and m80 fragment. *The Journal of Biological Chemistry* (2003), 278, 38421-38427.
23. Tikhomirov O., Carpenter G. Ligand-induced p38-dependent apoptosis in cells expressing high levels of EGFR and ErbB-2. *The Journal of Biological Chemistry* (2004), 279, 12988-12996.
24. Tikhomirov O., Carpenter G. Identification of the proteolytic fragments from ErbB-2 that induce apoptosis. *Oncogene* (2005), 24:3906-3913.
25. Tikhomirov O., Carpenter G. Bax activation and translocation to mitochondria mediate EGF-induced programmed cell death. *Journal of Cell Science* (2005), 118:5681-90.
26. Sergey V. Novitskiy, Sergey Ryzhov, Rinat Zaynagetdinov, Anna E. Goldstein, Yuhui Huang, Oleg Y. Tikhomirov, Michael R. Blackburn, Italo Biaggioni, David P. Carbone, Igor Feoktistov, Mikhail M. Dikov. Adenosine receptors in regulation of dendritic cell differentiation and function. *Blood* (2008), 112: 1822-1831. PMID: 18559975. PMCID: PMC2518889.
27. Tracking NF-kappaB activity in tumor cells during ovarian cancer progression in a syngeneic mouse model. Wilson AJ, Barham W, Saskowski J, Tikhomirov O, Chen L, Lee HJ, Yull F, Khabele D. *J Ovarian Res.* 2013 Sep 10;6(1):63. PMID: 24020521. PMCID: PMC3846584.

ARTICLE

Biocompatible mannosylated endosomal-escape nanoparticles enhance selective delivery of short nucleotide sequences to tumor associated macrophages

Cite this: DOI: 10.1039/x0xx00000x

Received 00th January 2012,
Accepted 00th January 2012

DOI: 10.1039/x0xx00000x

www.rsc.org/

Ryan A. Ortega^{abc}, Whitney J. Barham^c, Bharat Kumar^a, Oleg Tikhomirov^c, Ian D. McFadden^{abc}, Fiona E. Yull^{c*}, Todd D. Giorgio^{abc*}

Tumor associated macrophages (TAMs) can modify the tumor microenvironment to create a pro-tumor niche. Manipulation of the TAM phenotype is a novel, potential therapeutic approach to engage anti-cancer immunity. siRNA is a molecular tool for knockdown of specific mRNAs that is tunable in both strength and duration. The use of siRNA to reprogram TAMs to adopt an immunogenic, anti-tumor phenotype is an attractive alternative to ablation of this cell population. One current difficulty with this approach is that TAMs are difficult to specifically target and transfect. We report here successful utilization of novel mannosylated polymer nanoparticles (MnNP) that are capable of escaping the endosomal compartment to deliver siRNA to TAMs *in vitro* and *in vivo*. Transfection with MnNP-siRNA complexes did not significantly decrease TAM cell membrane integrity in culture, nor did it create adverse kidney or liver function in mice, even at repeated doses of 5 mg/kg. Furthermore, MnNP effectively delivers labeled nucleotides to TAMs in mice with primary mammary tumors. We also confirmed TAM targeting in the solid tumors disseminated throughout the peritoneum of ovarian tumor bearing mice following injection of fluorescently labeled MnNP-nucleotide complexes into the peritoneum. Finally, we show enhanced uptake of MnNP in lung metastasis associated macrophages compared to untargeted particles when using an intubation delivery method. In summary, we have shown that MnNP specifically and effectively deliver siRNA to TAMs *in vivo*.

Introduction

The tumor supportive stroma has been identified as an attractive target for therapeutic intervention in solid tumors. While most tumors exhibit a large degree of cellular heterogeneity, the tumor stroma is potentially more homogenous with respect to local stromal cell phenotype.¹ Macrophages, for example, play an important trophic role in tissue development and a growing body of evidence suggests that these trophic roles are recapitulated in the tumor microenvironment.² Tumor associated macrophages (TAMs) are directly involved in establishing a pro-tumorigenic local microenvironment in many tumor types. TAMs stimulate angiogenesis, promote tumor growth and metastasis, and suppress the normal immune response.^{3, 4} Concordantly, an increase in TAMs at the site of tumor progression is predictive of poor prognosis and survival in mouse models of human breast cancer and in multiple human cancers.^{5, 6}

TAMs exhibit characteristics that are a blend of the two defined categories of macrophage phenotype. Like the classically immunogenic (M1) macrophage, TAMs produce low levels of inflammatory cytokines which results in pro-tumorigenic, smoldering inflammation.^{7, 8} Like the typical tissue remodeling (M2) macrophage, TAMs break down the surrounding extracellular matrix, secrete growth factors, and inhibit the adaptive immune response.⁹ Data show that TAMs are a viable therapeutic target in cancer treatment and that ablating these cells can have a powerful anti-tumor effect.³ Rather than ablate these important modulators of immunity, another proposed solution is to target pro-tumor macrophages with a therapeutic agent that can alter their behavior to induce an acute, but strong

immunogenic phenotype capable of stimulating anti-tumor immunity.^{10, 11}

Recent decades have brought great advances in gene therapy technologies, specifically the emergence of siRNA. siRNAs can be used to inhibit the translation of specific mRNAs without significant off-target side effects by RNA interference (RNAi).¹² RNAi results in loss of target protein expression by siRNA binding to complementary mRNA strands, leading to mRNA degradation.¹³ The clinical translation potential of these nucleotides has been demonstrated by the targeted delivery of therapeutic siRNA in humans.^{14, 15} Another advantage of siRNA is that the degree of knockdown can be tuned to varying degrees of specificity, potency, duration by taking advantage of the transient nature of siRNA inhibition.¹⁶ One of the current obstacles therapeutic siRNA faces is the delivery of active siRNA to specific cell types. Free siRNA is rapidly degraded *in vivo* by circulating RNases. In addition, the strong polyanionic charge and significant molecular mass limits cellular entry of unformulated nucleotides. An siRNA delivery vehicle that provides preferential localization to particular tissues and/or target cell types as well as superior nucleotide protection and cellular entry is required for optimal and spatially specific protein knockdown.

Targeted nanoparticles have been used in clinical trials of siRNA therapeutics as a delivery device to reach specific cell populations.¹⁷ The generation of a charge-neutral or near-neutral surface of a nanoparticle carrier of siRNA improves biocompatibility, as well as allowing for the potential attachment of a targeting ligand to the surface of the particle, improving cellular specificity. To

address this, we have developed and characterized a tri-block polymer nanoparticle capable of targeting TAMs for nucleotide delivery. The core of the particle is comprised of a hydrophobic, pH responsive block that triggers endosomal escape and cytoplasmic delivery of the siRNA.¹⁷ One advantage of this core block design is its self-assembly into particles in an aqueous solution due to its tunable hydrophobicity.¹⁸ The second block is a poly(DMAEMA) polymer with a polycationic charge that condenses polyanionic oligonucleotides within the particle and serves to carry and protect siRNA for delivery to a target cell. A distal, azide-presenting block serves as a modular platform for further functionalization with targeting ligands or other biomolecules of interest and represents novelty in the nanoparticle synthesis scheme relative to our previous work.

Using ‘click’ chemistry, we previously functionalized the surface of these nanoparticles with a mannose ligand (MnNP) to specifically target TAMs via the mannose receptor, CD206.¹⁹ The mannose receptor is highly specific to mature macrophages and has been shown previously to be upregulated on the surface of TAMs.²⁰⁻²² MnNPs are systematically designed to condense and shield siRNA in the interior of the particle for optimal systemic transport, enter the tumor vasculature via the enhanced permeability and retention (EPR) effect, specifically target TAMs in the tumor microenvironment, and escape the low pH late endosome to deliver functional siRNA into the cytoplasm. In this study, we build upon previously published work to demonstrate that these MnNP are biocompatible *in vitro* and *in vivo* at physiologically relevant doses, provide evidence for the efficacy of the CD206-targeting mannose ligand on the surface of the particles, and demonstrate the effective delivery of protected nucleotides to TAMs.

Materials and Methods

Materials

Fabrication of nucleotide loaded MnNP. MnNP were fabricated as previously described.¹⁹ Briefly: the core of the particle is created by RAFT polymerization of butyl methacrylate (BMA), 2-propylacrylic acid (PAA), and 2-(Dimethylamino)ethyl methacrylate (DMAEMA) to create a hydrophobic, terpolymer with tunable endosomal escape properties. Next, a polycationic DMAEMA block is added by RAFT polymerization to add the capability to condense polyanionic therapeutics onto the particle. Finally, a 2-Azidoethyl methacrylate (AzEMA) block is polymerized onto the diblock polymer to form a triblock polymer terminated in an AzEMA block to support further functionalization. In order to create a mannose functionalized polymer, click chemistry is performed with alkyne –functionalized mannose to attach a mannose moiety to the end of the polymer. The completed polymer assembles into positively charged micelles when reconstituted in an aqueous solution, forming mannosylated nanoparticles.

For experiments using MnNP to deliver siRNA or short, fluorescently labeled DNA strands, MnNP polymer was reconstituted in sterile PBS at a concentration of 4 mg/ml and sonicated for 10 minutes. The MnNP in aqueous solution were used immediately or stored in aliquots at -20 °C. For complexation with the MnNP, all nucleotides were diluted to 50 μM in sterile, nuclease-free water. In order to form MnNP-nucleotide complexes with the optimal N:P ratio as described in our previous work, the 4 mg/ml MnNP solution was combined with 50 μM nucleotide solution in a 2:1, vol:vol ratio (160 ng of MnNP polymer per pmol of siRNA). The nucleotides were

allowed to complex with the MnNP for 1 hour at room temperature, then used in *in vivo* and *in vitro* experiments. Nucleotide loaded, hydroxyl-capped nanoparticles (OHNP) were also formulated using this protocol.

Methods

Particle zeta potential measurements. Average nanoparticle zeta potential (ζ) was determined by laser Doppler electrophoresis (LDE) using a Malvern Zetasizer Nano ZS (Malvern Inst. Ltd., Malvern, UK). Briefly, siRNA oligomer solution (50 μM, deionized water) was mixed with two times the volume of mannosylated nanoparticle solution (4 mg/mL, PBS) and reacted at room temperature to allow complexation. Aliquots were removed and diluted approximately 200-fold in molecular biology grade water for zeta potential measurement at time points relative to initiation of the nanoparticle-siRNA complexation reaction. Zetasizer measurements were performed at 25 °C with a scattering angle of 175°.

Cell culture. Unless otherwise stated, all primary cells isolated for use in this study were maintained in DMEM (Corning, MT-10-13-CV) with the addition of 10% (vol:vol) FBS and 1% Pen Strep (Gibco) at 37°C in a 5% CO₂ humidified atmosphere.

In vitro biocompatibility measurements. Bone marrow derived macrophages (BMDMs) were made by harvesting bone marrow from wild type mice on an FVB background. The media for these cells was supplemented with media from L-129 fibroblasts as a source of M-CSF.²³ The bone marrow was cultured for 6 days in the M-CSF supplemented media and the resultant BMDMs were scraped from their plates and re-plated as necessary for further experiments. For *in vitro* viability experiments, BMDMs were plated in 12-well plates at a density of 300,000 cells per well. BMDMs were transfected for 24 hours at 37°C with MnNP-siRNA complexes with a scrambled siRNA sequence at 10 nM and 50 nM concentrations of siRNA with accompanying MnNP concentrations as described above, with and without 6 hours of TNF- stimulation (10 ng/ml) following transfection. A second set of BMDMs were transfected with the same siRNA using Lipofectamine 2000 (10:1, vol:vol, Lipofectamine:siRNA) (Ambion) for 24 hours with and without TNF- stimulation. 2 minutes of incubation with Triton x-100 was used as a negative control for cell membrane viability. To stain cell membranes for an exclusion viability assay, samples were incubated with Trypan Blue for 5 minutes, and the number of viable and non-viable cells were counted (over 1000 cells per sample, N=3 for each condition).

In vivo biocompatibility measurements. All animal experiments were approved by the Vanderbilt University Institutional Animal Care and Use Committee. Wild type FVB mice were i.v. injected via the retro-orbital route with MnNP-scrambled siRNA complexes (siRNA: scrambled negative control sequence, Ambion) at 5 mg/kg of particles every 24 hours for 3 doses. 24 hours after the final injection, blood serum was taken from the mice and analyzed at the Vanderbilt Translational Pathology Core Laboratory. Alanine transaminase (ALT) and aspartate transaminase (AST) levels were measured as an indicator of hepatic function and blood urea nitrogen (BUN) and serum creatinine (CREAT) as an indicator of renal function.

Rapid adhesion enrichment of TAMs. In order to enrich the TAM population from solid mammary and ovarian tumors, the tumors were removed and homogenized in cell culture media with Collagenase A (5 mg/ml, Roche) and DNaseI (5 mg/ml, Roche) for 2 hours. After 2 hours of incubation with gentle rocking, the

homogenate was filtered through 70 micron filters and the cells were pelleted via centrifugation at 1000 g for 10 minutes. The pellet was then resuspended in 2 ml of ACK red blood cell lysis buffer (Gibco) for 2 minutes. The cell suspension was then diluted to 20 ml, pelleted, and the pellet resuspended in culture media. The tumor homogenate was then added to 6- or 12-well plates with 10 million, or 3 million cells per well, respectively. The homogenate was incubated in the well plates for 45 minutes, and the non-adhered cells vigorously washed from the wells with PBS (3 washes), leaving the cells adhered to the plate at approximately 80-90% coverage.²⁴⁻²⁶

***In vitro* transfection of murine mammary PyMT TAMs.**

Spontaneously arising murine mammary tumors were harvested at a palpable stage from 12 week old mice with a mammary epithelium targeted polyoma middle T oncogene (PyMT, FVB strain background).³¹ TAMs were enriched into 12-well plates with a 45 minute, rapid-adhesion protocol. After the TAMs were enriched, they were transfected with FAM-labeled, scrambled siRNA (Ambion) for 2 and 6 hours using MnNP, alcohol-capped (non-targeted) endosomal escape nanoparticles (OHNP), or Lipofectamine. A control set of TAMs were incubated with free, FAM-labeled siRNA alone. After transfection, the cells were gently washed three times with sterile PBS and fixed in 4% paraformaldehyde for 30 minutes at 4°C. FAM fluorescence was measured in each sample with a Tecan Infinite M1000-Pro plate reader as an indicator of siRNA delivery with 12 measurements per well in a filled circular pattern.

***In vivo* delivery of fluorescently labeled DNA to murine mammary PyMT TAMs.**

Palpable tumors from 12-week old PyMT mice were used to examine the nucleotide delivery efficacy of MnNP *in vivo*. A 21 base pair, Cy3-labeled DNA sequence was purchased from Sigma as a plentiful source for nucleotides for complexation with MnNP. The sequence was designed to have the same sequence as the scrambled siRNA, and the same charge characteristics, such that particle complexation with the DNA sequence would not differ from complexation with siRNA. Three ellipsoidal tumors were selected from each mouse from three separate glands with an average tumor volume of $5.2 \pm 1.9 \text{ cm}^3$. Tumors were selected based on their isolation from any other large tumor and on uniformity of size and shape. One tumor from each mouse received an injection of MnNP-DNA_Cy3 complexes into the centroid of the tumor at a dose of 5 mg/kg, one tumor received an equivalent dose of cy3-labeled DNA, and one tumor received a 100 μl PBS injection. The tumors were injected in this fashion every 24 hours for three total doses. 24 hours after the final dose, the tumors were removed, homogenized, and the TAM population was enriched with a 45 minute rapid adhesion protocol. Cy3 fluorescence was measured in each sample with a Tecan Infinite M1000-Pro plate reader as an indicator of DNA delivery with 12 measurements per well in a filled circular pattern. The data are shown after background subtracting fluorescent averages from the tumors receiving MnNP-DNA_Cy3 complexes normalized to the tumor samples receiving free DNA_Cy3.

***In vivo* delivery of fluorescently labeled DNA to murine solid ovarian tumor TAMs.**

ID8 cells were generously gifted by Drs. D. Khabele and A. Wilson of the Vanderbilt Ingram Cancer Center. Cy5-labeled DNA was purchased from Sigma (21 base pairs). ID8 cells were injected into the peritoneal cavity of mature C57B16 female mice (10 million cells per mouse). 60 days after ID8 cell injection, the mice began to present with increased total mass and distended abdomens, indicating the beginning stages of ascites development. The mice received 2 injections, 24 hours apart of untargeted particles with DNA_cy5 (5 mg/kg, 3 mice) or mannose receptor targeted particles with DNA_cy5 (5 mg/kg, 3 mice). 24 hours after the last injection, the mice were euthanized and the tumors on the peritoneum

were removed and homogenized. The TAMs were enriched with a 45 minute rapid adhesion protocol. Cy5 fluorescence was measured in each sample with a Tecan Infinite M1000-Pro plate reader as an indicator of DNA delivery with 12 measurements per well in a filled circular pattern.

Imaging of *ex vivo* ovarian ascites TAMs.

Ascites fluid was harvested from the ovarian tumor bearing mice described previously.²⁷ TAMs were enriched with a 45 minute rapid adhesion protocol on glass slides. MnNP-DNA_Cy3 complexes were delivered to the adhered cells for 24 hours. F4/80 antibody was purchased from Serotec (clone: CI:A3-1) and mannose receptor antibody was purchased from Abcam (ab64693). The TAMs were fixed in 4% PFA for 30 min and permeabilized in 0.4% Triton X-100 for 10 min. The slides were then washed twice in TBS with 0.05% Tween 20 (TBSTw, 10 min) and once with TBS (5 min). The cells were then blocked for 1 hr in 0.01M Tris-HCl, pH7.4, 2% BSA, 2% goat serum. The samples were incubated with primary antibodies overnight in blocking buffer at 4°C, washed 3x in TBSTw, and incubated with secondary antibodies for 2 hrs. The slides were then washed 3x with TBSTw, once in TBS, and mounted using Molecular Probes ProlongGold antifade reagent (Invitrogen). Images were acquired with an LSM 510 Meta confocal microscope in the Vanderbilt Medical Center Imaging Core facility.

Murine lung metastasis tumor model and delivery of nanoparticles via intubation. 0.5 million L129 PyMT tumor cells were injected via tail vein into wildtype FVB mice.²⁸ 2 weeks after injection, each mouse was anesthetized with isoflurane and placed on a tilted rodent work stand in the supine position and restrained in position by an incisor loop. The tongue was extruded using forceps, the mouse intubated, and given a 5 mg/kg dose of either MnNP-DNA_Cy5 complexes (n=5) or OHNP-DNA_Cy5 complexes (n=3). Control animals received a 60 μl dose of sterile PBS. After the tubing was removed, the mice were observed until normal respiration resumed.

IVIS imaging of whole lungs.

Whole lungs were removed 6 hrs post-injection from mice receiving MnNP-DNA_Cy5 via intubation (n=2) or via i.v. injection (n=2), and an untreated control mouse. All lungs were tumor bearing. Lungs were perfused and inflated with cold PBS and then imaged for Cy5 fluorescence using a Xenogen IVIS 200 bioluminescent and fluorescent imaging system and Living Image software at the Vanderbilt University Institute of Imaging Science.

Isolation of lung cells and flow cytometry.

Lungs were perfused with sterile PBS and digested as described above. Single cell suspensions were kept at 4°C and incubated with 1% BSA in PBS to reduce non-specific antibody binding. The panel of antibodies used in these experiments included CD45-PE-Cy7 (clone 10-F11), Gr1-Alexa Fluor 700 (clone RB6-8C5), and CD11B-APC (clone M1/70) (all from BD Bioscience). Flow cytometry was performed using a BD LSR II flow cytometer (BD Bioscience) and data were analyzed with FlowJo software (TreeStar) and significant differences were determined using the Student's T-test. To identify the myeloid cell subset in the lung homogenate, we began by sorting cells based on CD45 expression. To further differentiate cell populations, we sorted cells based on the presence of CD11b and the presence or absence of Gr1. We defined the macrophage population as being CD45⁺/CD11b⁺/Gr1⁻ and both monocytes and polymorphonuclear (PMN) cells as being CD45⁺/CD11b⁺/Gr1⁺.²⁹ These simple flow panels allowed us to isolate normal macrophages and TAMs from other myeloid cell populations that could uptake delivered nanoparticles through non-specific mechanisms.^{30, 31}

Results and Discussion

Particle-siRNA complexation and biocompatibility. MnNPs were synthesized as previously reported.¹⁹ The chemical structure of the particles is shown in Figure 1A.

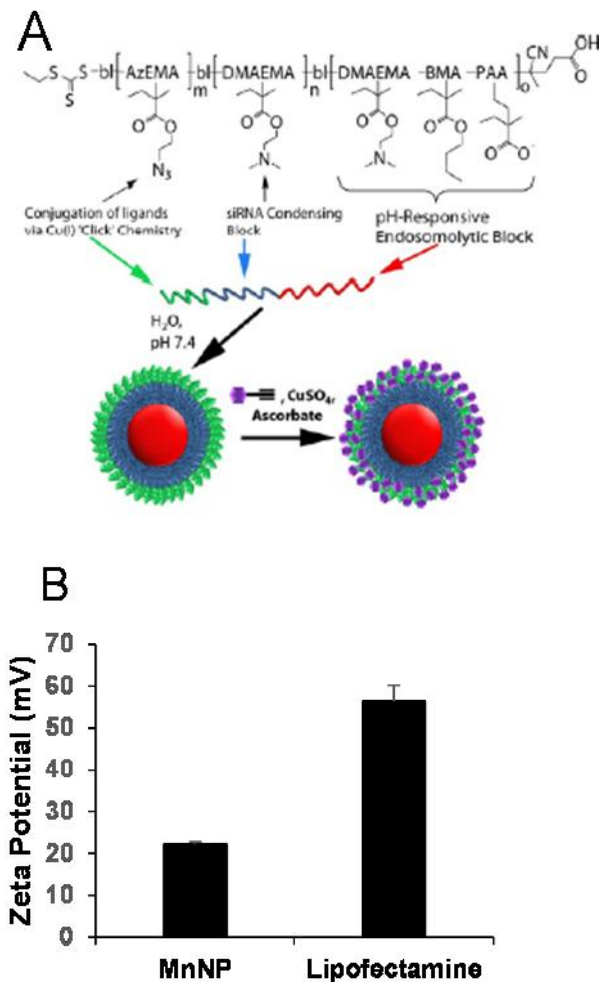


Fig. 1 (A) Schematic representation of the mannosylated endosomal escape nanoparticle illustrating the pH-responsive core (red), the siRNA condensing block (blue), the modular 'clickable' surface (green), and the mannose surface functionalization (purple). (B) Zeta potential measurements of MnNP show a significantly milder surface charge as compared to commercial transfection agent, Lipofectamine 2000. ($P = 0.003$, $N=3$)

Commercial transfection agents, such as Lipofectamine, possess strong, positive surface charges which facilitate their ability to deliver siRNA and other nucleotides into cells. This same surface charge renders commercial transfection agents unacceptable for *in vivo* use; they exhibit low biocompatibility due to aggregate formation and cytotoxicity. Strongly cationic structures have the potential to adsorb anionic serum proteins and lose function through aggregation or become opsonized and rapidly cleared from the blood compartment. Therefore, net surface charge of the formulated delivery system is known to be an important determinate of *in vivo* function. The cationic charges in MnNPs are designed to be largely shielded from surface presentation to optimize their potential for *in vivo* use. The success of this shielding strategy was confirmed by the moderately positive zeta potential of approximately +20 mV as

measured by dynamic light scattering (Figure 1B) in comparison with Lipofectamine 2000, a commonly used commercial transfection agent with a zeta potential of more than +50 mV. Charge-based considerations are of paramount importance in the context of intravascular administration; however, similar considerations are operative for the intraperitoneal and tracheal delivery used in these studies. Thus, the low cationicity MnNPs may optimize successful siRNA delivery to TAMs by the routes of administration considered here.

Cationic charge mediates strong interactions with anionic cell membranes to facilitate delivery of cargo *in vitro*, but also may destabilize cells and be responsible for dose-limiting toxicity. We determined the effect of MnNP on membrane viability in bone marrow derived macrophages (BMDMs) as an *in vitro* measurement of the biocompatibility of the MnNP-siRNA complexes (Figure 2). siRNA was delivered at low (10 nM) and high (50 nM) concentrations in the presence or absence of a second immunostimulatory cytokine, TNF- α (10 ng/ml), a common tumor promoter in the tumor microenvironment.^{32, 33} After 24 hours of incubation with MnNP-siRNA there was no significant decrease in BMDM membrane viability in samples transfected with MnNP as measured by Trypan Blue staining.³⁴ The high siRNA concentration had a slight effect on BMDM membrane viability in the context of the addition of TNF- α , but this effect was not significant. In contrast, in the presence of TNF- α , transfection with the commercial agent, Lipofectamine 2000, resulted in a significant decrease in viability (21-23%). Lipofectamine is a mixture of positively charged lipids; the strongly positive surface charge on the lipid transfection complex results in an efficacious *in vitro* transfection agent, but significantly decreased biocompatibility *in vivo* due to strong interactions with the plasma membrane of non-targeted cells.³⁵ In contrast, MnNP-siRNA complexes possess only a mildly positive surface charge, resulting in increased biocompatibility and suitability for both *in vitro* and *in vivo* transfection.

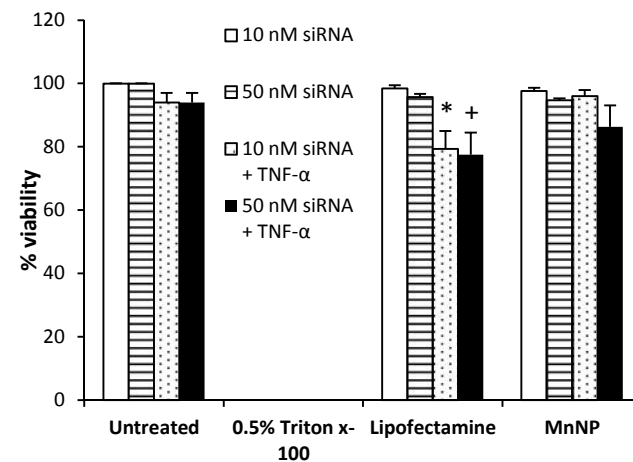


Fig. 2 Transfection of BMDMs *in vitro* with MnNP-siRNA complexes results in no significant loss in membrane viability, even with secondary stimulation from 10 ng/ml TNF- α stimulation for 6 hours. There is significant loss in viability associated with the use of Lipofectamine as a transfection agent under these conditions. (*, +: $P < 0.05$ by T-test, $N=3$ for each condition)

To test *in vivo* biocompatibility, wild type FVB mice were intravenously (i.v.) injected with MnNP-scrambled siRNA complexes at 5 mg/kg once daily for 3 consecutive days. This route of administration was chosen for the biocompatibility study because systemic administration is expected to potentially induce any off target, negative effects more strongly than other, more spatially contained administration routes such as intraperitoneal injection or

intratracheal delivery. 24 hours after the final injection, blood serum was analyzed for alanine transaminase (ALT) and aspartate transaminase (AST) levels as an indicator of hepatic function and blood urea nitrogen (BUN) and serum creatinine (CREAT) as an indicator of renal function. No significant change in liver or kidney function was observed following 3 sequential doses every 24 hours with MnNP, consistent with a lack of acute, organ level toxicity (Table 1). Average serum creatinine was slightly lower than the normal range, but the difference is not large enough to indicate renal damage.³⁶ Since we anticipate that MnNPs will clear the vasculature primarily through liver/spleen/reticuloendothelial mechanisms and that molecular components from disassembled micelles (if any) will be sufficiently small for renal excretion, the lack of significant dysregulation in liver and kidney characteristics suggests both nontoxicity and serum stability. Also by utilizing spatially confined routes of administration many of the complications potentially associated with systemic delivery of nanoparticles can be mitigated.

	Mouse Number				Average	—	normal
	1	2	3	4			
ALT (U/L)	37	49	73	105	66	30	26-120
AST (U/L)	96	86	213	140	133.8	57.8	69-191
BUN (mg/dL)	21	23	27	23	23.5	2.51	19-34
CREAT (mg/dL)	0.4	0.3	0.3	0.4	0.35	0.05	0.4-0.6

Table 1 Analysis of blood serum enzyme levels revealed no acute changes in liver or kidney function indicating poor MnNP biocompatibility in mice receiving three, 5 mg/kg i.v. doses of MnNP-siRNA complexes, 24 hours apart.

MnNPs enhance delivery of fluorescently labeled siRNA to TAMs *ex vivo*. Spontaneously arising murine mammary tumors were harvested from 12 week old mice containing a mammary epithelium targeted polyoma middle T oncogene (PyMT).³⁷ *Ex vivo* TAMs were transfected with FAM-labeled siRNA for 2 or 6 hours with either MnNP, hydroxyl-capped (non-targeted) endosomal escape nanoparticles (OHNP), or Lipofectamine (Figure 3) and intracellular FAM fluorescence was used as an indicator of nanoparticle uptake in the transfected TAMs.

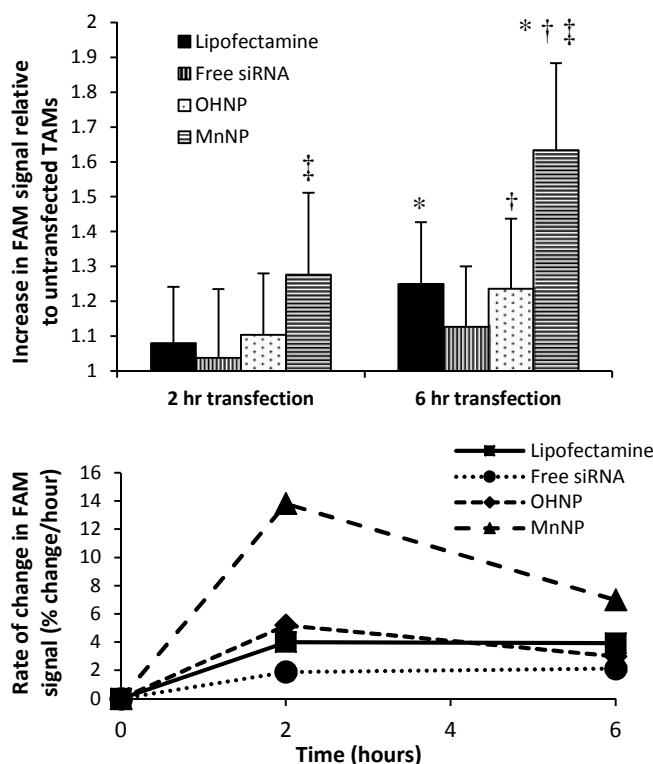


Fig 3 In vitro transfection of TAMs isolated from murine mammary PyMT tumors with MnNP results in greater uptake of FAM labeled siRNA as compared to other transfection agents. MnNP creates a significantly greater increase in FAM fluorescence in the TAMs from the 2 hr to the 6 hr time point as compared to Lipofectamine or the non-targeted OHNP (*, †, ‡: P < 0.05, by T-test) and the high rate of change of FAM fluorescence in these cells indicates a rapid burst effect in delivery using MnNP. The two non-targeted agents have similar delivery efficacies.

After 6 hours of transfection, TAMs exposed to MnNP-siRNA_FAM had significantly higher FAM fluorescence than TAMs transfected with Lipofectamine (1.6-fold increase in FAM fluorescence vs 1.25-fold increase). Furthermore, fluorescence measured in TAMs transfected with the non-targeted OHNP was not significantly different than the fluorescence measured in TAMs transfected with the highly cationic Lipofectamine (also possessing no specificity for TAMs). For all samples, siRNA delivery increased from 2 to 6 hours, with the greatest increase occurring in the MnNP transfected samples. The rate of MnNP uptake by the TAMs is also increased at the 2 hour time point compared to the untargeted transfection agents. We observed a burst effect in delivery during the first few hours in the MnNP transfected samples indicating rapid, mannose-mediated uptake. Without the aid of transfection complexes, a small amount of free siRNA is taken up by the TAMs. This is likely due to phagocytosis of the siRNA molecules by the macrophages following binding of serum proteins to the siRNA. It is important to note that while unmodified siRNA may be taken up by cells in a non-specific manner both *in vitro* and *in vivo*, siRNA delivered in this fashion exhibits little to no activity. The transfection efficacy of the untargeted nucleotide, OHNP and Lipofectamine, are similar. Previously, we have demonstrated enhanced siRNA delivery to murine BMDMs *ex vivo* by MnNPs to be mannose dependent. Results of this study, with TAMs, are consistent with earlier findings confirming MnNP recognition by CD206 in BMDMs.¹⁹

MnNPs deliver fluorescently labeled nucleotides to murine TAMs *in vivo*. In order to test the *in vivo* efficacy of the TAM-targeted MnNP, we delivered MnNP carrying fluorescently tagged, scrambled DNA strands to murine tumors in several tumor models. PyMT mice have spontaneously developed palpable mammary tumors with dimensions 1 cm at 12 weeks and the tumors have a necrotic core with significant immune cell infiltration and TAM population.^{37, 38} Due to the poorly vascularized nature of this tissue, cells and fluid entering the tumor are retained in the local microenvironment longer than they would be retained in normal tissue.^{39, 40} We directly injected MnNP-DNA conjugates into the center of the tumor for a well contained depot of particles that would co-localize with TAMs (Figure 4A). We observed no adverse effects of multiple, direct MnNP injections.

Formulation with MnNPs significantly increased DNA_Cy3 delivery to TAMs in murine breast tumors (Figure 4B). Intratumoral injection of a fluorescently labeled DNA mimic of siRNA resulted in nearly 2-fold greater TAM uptake compared to unformulated control DNA_Cy3 administered to another mammary tumor in the same mouse. These data suggest that the MnNP formulation is capable of interacting with TAMs in a persistent way, noting that this study was carried out as three injections, each separated by 24 hours. This demonstrates that injecting MnNPs directly into a primary tumor can successfully deliver nucleic acid material to TAMs. The direct injection approach avoids the potential issues associated with intravascular administration of MnNPs.

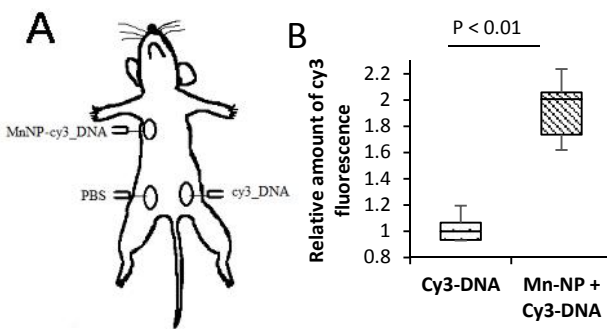


Fig 4 (A) Diagram of mammary tumor injection scheme for PyMT mice. Three isolated tumors from each mouse (N=3) were selected based on uniformity of size and shape. The tumors were injected 3 times, 24 hours apart with MnNP-DNA_Cy3 complexes, free DNA_Cy3, or PBS into the center of each selected tumor. The TAMs were isolated from each tumor and analyzed for cy3 fluorescence. (B) There was a statistically significant increase in Cy3 fluorescence in TAMs from tumors that received MnNP-DNA_Cy3 as compared to non-specific DNA_Cy3 phagocytosis.

MnNPs facilitated a similar increase in *in vivo* delivery of DNA_Cy5 to TAMs in a murine ovarian tumor model (Figure 5A).⁴¹ The solid tumors in this implanted ovarian tumor model contain a significant TAM population and the ascites fluid generated contains a large amount of blood and immune cell infiltrate composed largely of TAMs.^{27, 42-45} Evidence specifically supports mannose interaction of the MnNPs with TAMs in peritoneal tumors as DNA_Cy5 fluorescence is significantly elevated following MnNP delivery in comparison with identical, but non-mannosylated, hydroxyl-capped NPs. This result confirms the persistence of DNA_Cy5 delivery over two intraperitoneal injections spaced 24 hours apart. The environment of the ovarian tumors is somewhat unique in that prior to extremely late stages of progression, tumors are confined within the peritoneal

compartment. This data provides evidence that an approach in which MnNPs are injected directly into the peritoneal cavity can successfully deliver nucleic acid material to TAMs without the potential complications associated with intravascular delivery.

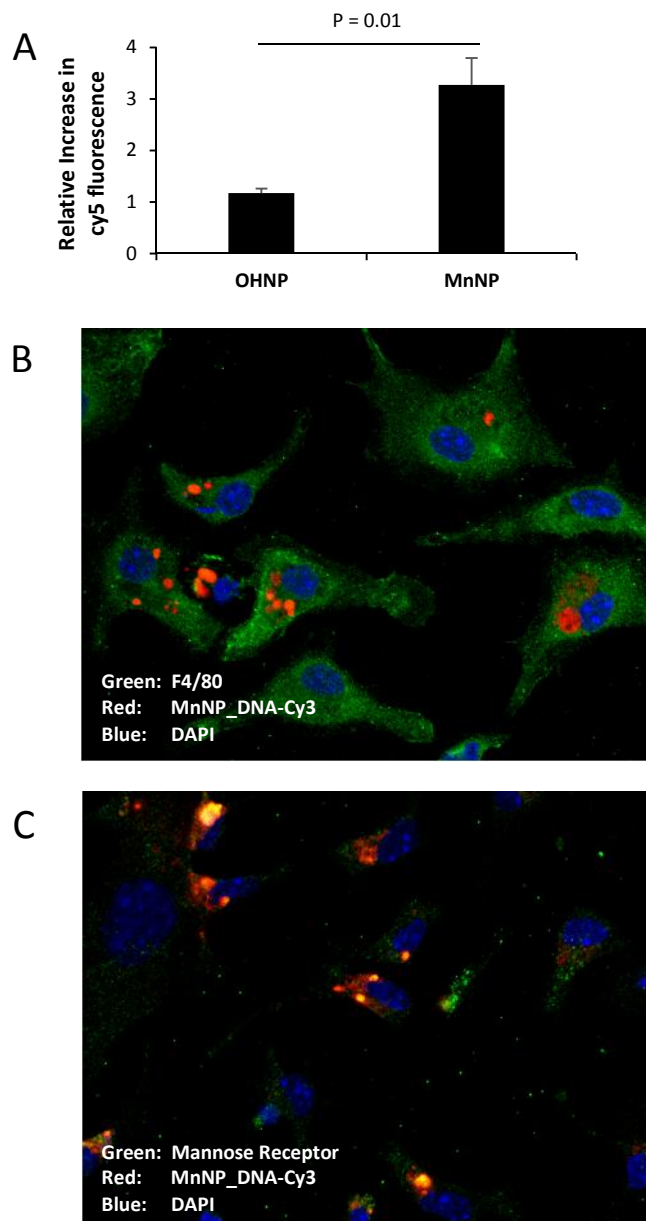


Fig 5 (A) Cy5 fluorescence is significantly increased in murine ovarian tumor TAMs when Cy5-labeled DNA is delivered with mannosylated nanoparticles in vivo as compared to labeled DNA delivered with non-targeted nanoparticles (T-test for significance, n=3 mice). (B & C) *Ex vivo* ascites TAMs incubated with MnNP-DNA_Cy3 for 24 hours show uptake and retention of fluorescently labeled nucleotides. (Blue DAPI nuclear stain) (B) Green, F4/80 labeling on the cell membrane confirms that the adhered cells are macrophages. Red, Cy3 labeling can be seen retained in the cytoplasm of the macrophages. (C) The mannose receptor (green) can be seen on the cell surface and co-localized with Cy3 fluorescence (red: DNA-Cy3, yellow: co-localization).

Figures 5B and 5C show confocal images of *ex vivo* ovarian ascites TAMs labeled for macrophage marker F4/80 (5B, green) or

M2 macrophage marker and MnNP target, mannose receptor (5C, green).^{22, 29} Nanoparticle fluorescence patterns show punctate staining indicative of endosomes containing small numbers of MnNP as well as larger aggregate staining consistent with cytoplasmic release of the MnNP contents. These images confirm that the MnNP are taken up and retained by TAMs. Furthermore, MnNP are internally co-localized with the mannose receptor, as seen by the green-red overlap (yellow) in 5C. Unbound mannose receptor can be seen at the cell surface. The mannose receptor facilitates endosomal uptake of bound ligands (in this case the MnNP) and the bond ligand-receptor complex is transported into the cytoplasm inside the resultant endosome.

The third *in vivo* model used to demonstrate MnNP targeting of TAMs was a model in which PyMT mammary tumor cells are injected via the tail vein to establish tumors in the lungs (Figure 6A). Lung metastases are one of the most common, potentially deadly sites for breast cancer metastases.⁴⁶ The murine tail vein metastasis model simulates primary mammary tumor cells that have seeded into the lungs and established metastatic growth, though this method of delivery would also be applicable for MnNP delivery to primary lung cancer as well. DNA_Cy5 carrying nanoparticles were delivered directly into the metastasis bearing lungs via intubation. This delivery method was chosen for multiple reasons: not only are the nanoparticles spatially contained within the lungs, but intubation is a clinically relevant delivery method that results in longer lung retention of the delivered therapeutic compared to systemic delivery.⁴⁷

Figure 6B shows that 6 hours after administration, MnNP delivered via intubation are detected in the lungs in greater amounts than MnNP delivered i.v. This image also demonstrates that delivery via intubation is capable of perfusing the MnNP solution throughout the entire lung. Flow cytometry analysis performed 24 hours after particles were delivered via intubation shows that approximately 40% of CD11b⁺ myeloid cells contain DNA_Cy5 formulated with MnNPs (Figure 6C). This population is primarily composed of macrophages and granulocytes with some dendritic cells (DCs) and natural killer (NK) cells. DNA_Cy5 was detected in a relatively small number of non-myeloid cells, on the order of 2% in the same samples of lung homogenate. Furthermore, DNA_Cy5 uptake by CD45⁺/CD11b⁺/Gr1⁺ macrophages is significantly increased in this model through formulation with MnNP as compared with DNA_Cy5 formulated with untargeted OHNP (Figure 6D). DNA_Cy5 uptake is not enhanced by mannose presentation on the NP corona in PMN cells and monocytes (CD45⁺/CD11b⁺/Gr1⁺) (Figure 6D); there is no significant difference in DNA_Cy5 delivery between MnNP and OHNP formulations with these cell types. These results are consistent with strong, mannose-dependent delivery to macrophages and weak, non-specific delivery (presumably by phagocytosis) to PMN cells and monocytes. Intubation enables direct access to lung tumor TAMs for NPs, avoiding NP dilution and other challenges resulting from intravascular administration. These data demonstrate that mannose decoration of the endosomal escape nanoparticle mediates preferential delivery of NPs to TAMs but not non-myeloid cell types which are co-localized with the TAMs in this model system.

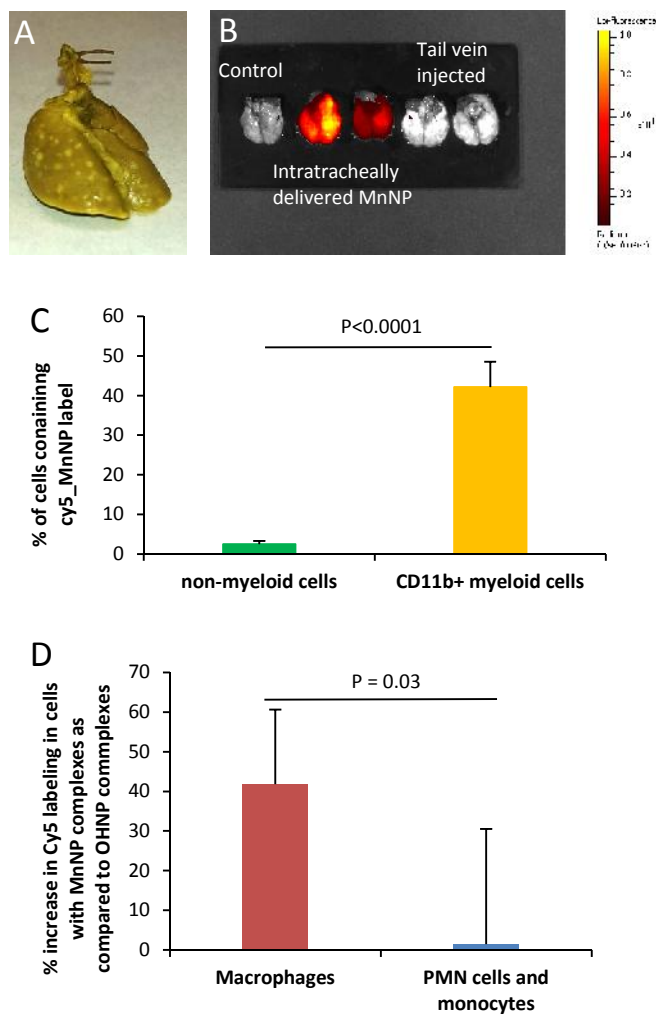


Fig 6 MnNP have enhanced uptake in TAMs associated with mammary lung metastases using an intubation delivery model. (A) Metastases are visualized in the lungs ex vivo following inflation with Bouin's fixative. Tumors appear white against the normal lung, which stains yellow. (B) IVIS imaging of lungs ex vivo shows intubation administration of MnNP results in more than 10 times the Cy5 fluorescence vs intravenous administration of MnNP as visualized 6 hours after delivery. (C) Flow cytometry reveals minimal uptake of MnNP (approximately 2%) in non-myeloid cells. There is significantly more uptake of MnNP in CD11b⁺ myeloid cells. (D) MnNP show 40% increased uptake by macrophages as compared to OHNP. There is no significant difference in nanoparticle uptake between MnNP and OHNP in PMN cells and monocytes.

The design of siRNA delivery vehicles intended for intravascular administration leading to tissue-specific accumulation is an enormous, multidimensional challenge. Such a construct must sequester and protect siRNA, avoid adverse effects resulting from interactions with serum proteins and the formed elements of the blood, possess sufficient blood compartment half-life for robust extravasation and delivery in the target tissues and offer a mechanism for preferential retention. Nonspecific toxicity must also be low. In addition, once localized, the carrier must facilitate cellular entry and endosomal escape to provide optimal conditions for effective intracellular RNAi. Despite the significant and broad potential clinical applications of RNAi, these barriers limit practical use of siRNA in humans.

Many potential clinical uses of siRNA may be approachable from other, non-intravascular, routes of administration. In this study, we assessed the capacity of an advanced nanoscale delivery system, designed for siRNA protection, preferential interaction with cells displaying CD206 and endosomal escape to facilitate efficient RNAi in models with clinical relevance using methods that avoid intravascular administration.

This study is the first to demonstrate mannose-mediated preferential siRNA delivery to TAMs *in vivo*. *Ex vivo* studies inform three subsequent *in vivo* treatment approaches, each employing local/regional routes of administration that avoid the significant obstacles and design challenges associated with intravascular administration. Some additional advantages common to NP delivery approaches that are confined to local/regional tissues is avoidance of the liver delivery and rapid urinary clearance that are significant limiters for successful intravascular administration of siRNA delivery vehicles. Importantly, the characterizations obtained in *ex vivo* experiments with TAMs are predictive of potential *in vivo* efficacy.

We demonstrated that formulation of an siRNA surrogate into the MnNP construct enables preferential delivery to TAMs following intratumoral injection. Many characteristics likely contribute to this result, including the slightly positive zeta potential of the MnNP relative to free polynucleotide and protection against enzymatic degradation. *In vivo* stability and biocompatibility of the MnNP is also inferred from this result, consistent with previous studies and confirmed explicitly in this work by a more rigorous, intravascular study. Intratumoral administration has potential as an adjuvant therapy for primary, recurrent breast cancers, but likely is more suitable for other cancers that can be individually identified and present near the skin surface, such as head and neck cancers or melanoma.

MnNPs administered intraperitoneally effectively deliver nucleotide payloads to TAMs in the distributed tumor burden associated with ovarian cancers. This study provides the clearest evidence that mannosylation is responsible for TAM selectivity *in vivo*, in agreement with previous work and the known surface display of CD206 on macrophages, especially pro-tumor TAMs. Multiple doses of MnNPs were well tolerated. Spatial confinement of the MnNP dose in the peritoneal cavity presumably enhances the opportunity for interaction with ovarian TAMs relative to intravascular dosing through greater proximity and longer persistence. The ability of MnNPs to preferentially localize in lung metastasis TAMs following intubation delivery implies transport of the nanomaterials from the alveolar side of the tissue into the tumors. Mannose-dependent interaction of MnNPs with TAMs is demonstrated from a different perspective in this study relative to the ovarian results in that flow cytometry confirms both strong nucleotide delivery to TAMs and lack of delivery to non-myeloid cells. All animals tolerated the intubation and delivery of MnNPs, despite a brief, acute response to the significant fluid burden administered to the lungs in both experimental and control groups. MnNPs reformulated as a more concentrated suspension will be explored to minimize the acute response through minimization of the liquid volume required, although careful attention must be devoted to the consequent stability of MnNPs in a more concentrated solution.

Conclusions

These studies demonstrate the biocompatibility of MnNP both *in vitro* and *in vivo*, and provide evidence for enhanced TAM-targeting generated through the use of mannose as a targeting ligand on the particle surfaces. Here we provide evidence that

these MnNP produce no significant toxicity when used *in vivo*. Incubating BMDMs with MnNP did not significantly decrease cell membrane viability and repeated treatments in adult mice creates no acute kidney or liver damage. Furthermore, we showed that MnNP are effective at delivering fluorescently-labeled nucleotides to TAMs in spontaneously formed, primary mammary tumors. Additionally, mannose-targeting on the surface of the MnNP results in greater delivery of labeled nucleotides to ovarian tumor TAMs compared to non-targeted, hydroxyl-capped nanoparticles with the same core structure.

Future studies will aim to further develop MnNP for biological applications and eventual clinical use, specifically utilizing MnNP to deliver active siRNAs to TAMs *in vivo* to knock down specific target proteins in key transcriptional pathways essential for creating the TAM phenotype. Potential targets include proteins of the NF- B or JAK-STAT transcriptional pathways, both of which have been implicated in generating the TAM phenotype. By manipulating these pathways with MnNP-delivered siRNA, it may be possible to mitigate pro-tumor contributions from TAMs or to activate an immunogenic, anti-tumor phenotype in this macrophage population. Immune modulation could be confirmed by direct cytotoxicity assay and an analysis of changes in tumor cytokine levels.

Acknowledgements

The work performed in this study was funded in part by a Collaborative Idea Award through the Department of Defense CDMRP Breast Cancer Research Program (W81XWH-11-1-0242, W81XWH-11-1-0344). The ovarian tumor experiment was partially funded by a Translational Pilot Award through the Department of Defense CDMRP Ovarian Cancer Research Program (W81XWH-11-1-0509). Nanoparticle characterization was performed at the Vanderbilt Institute of Nanoscale Science and Engineering, using facilities renovated under National Science Foundation Grant ARI-R2 DMR-0963361. Flow Cytometry experiments were performed in the VMC Flow Cytometry Shared Resource supported by the Vanderbilt Ingram Cancer Center (P30 CA68485) and the Vanderbilt Digestive Disease Research Center (DK058404). Analysis of blood serum enzyme levels was performed at the Vanderbilt Translational Pathology shared resource. The authors would like to thank Andrew Wilson and Dineo Khabele from the Vanderbilt Ingram Cancer Center for instruction in setting up the ovarian tumor model and for providing the ID8 cells for that experiment. We would also like to thank Rinat Zaynagetdinov and Wei Han, Division of Allergy, Pulmonary and Critical Care Medicine, Vanderbilt University Medical Center, for advice and instruction for performing the rapid adhesion isolation of TAMs and for advice and assistance regarding intratracheal delivery of nanoparticles and the following flow cytometry. Finally, we would like to thank Kellye Kirkbride, Vanderbilt Department of Biomedical Engineering, for her assistance with manuscript editing.

Notes and references

^a Department of Biomedical Engineering, Vanderbilt University, Nashville, TN 37235, United States

^b Vanderbilt Institute for Nanoscale Science and Engineering, Vanderbilt University, Nashville, TN 37235, United States

^c Department of Cancer Biology, Vanderbilt-Ingram Cancer Center, Nashville, Tennessee 37232, United States

* Corresponding authors: todd.d.giorgio@vanderbilt.edu, fiona.yull@vanderbilt.edu

1. Y. Mao, E. T. Keller, D. H. Garfield, K. Shen and J. Wang, *Cancer metastasis reviews*, 2013, **32**, 303-315.
2. J. W. Pollard, *Nature reviews. Immunology*, 2009, **9**, 259-270.
3. J. Condeelis and J. W. Pollard, *Cell*, 2006, **124**, 263-266.
4. B. Z. Qian and J. W. Pollard, *Cell*, 2010, **141**, 39-51.
5. L. S. Ojalo, W. King, D. Cox and J. W. Pollard, *The American journal of pathology*, 2009, **174**, 1048-1064.
6. M. Heusinkveld and S. H. van der Burg, *Journal of translational medicine*, 2011, **9**, 216.
7. L. M. Coussens and Z. Werb, *Nature*, 2002, **420**, 860-867.
8. F. R. Greten, L. Eckmann, T. F. Greten, J. M. Park, Z. W. Li, L. J. Egan, M. F. Kagnoff and M. Karin, *Cell*, 2004, **118**, 285-296.
9. A. Mantovani, S. Sozzani, M. Locati, P. Allavena and A. Sica, *Trends in immunology*, 2002, **23**, 549-555.
10. W. Han, M. Joo, M. B. Everhart, J. W. Christman, F. E. Yull and T. S. Blackwell, *American journal of physiology. Lung cellular and molecular physiology*, 2009, **296**, L320-327.
11. R. Zaynagetdinov, T. P. Sherrill, V. V. Polosukhin, W. Han, J. A. Ausborn, A. G. McLoed, F. B. McMahon, L. A. Gleaves, A. L. Degryse, G. T. Stathopoulos, F. E. Yull and T. S. Blackwell, *Journal of immunology*, 2011, **187**, 5703-5711.
12. S. M. Elbashir, J. Harborth, W. Lendeckel, A. Yalcin, K. Weber and T. Tuschl, *Nature*, 2001, **411**, 494-498.
13. A. Fire, S. Xu, M. K. Montgomery, S. A. Kostas, S. E. Driver and C. C. Mello, *Nature*, 1998, **391**, 806-811.
14. M. E. Davis, *Molecular pharmaceutics*, 2009, **6**, 659-668.
15. M. E. Davis, J. E. Zuckerman, C. H. Choi, D. Seligson, A. Tolcher, C. A. Alabi, Y. Yen, J. D. Heidel and A. Ribas, *Nature*, 2010, **464**, 1067-1070.
16. A. D. Judge, M. Robbins, I. Tavakoli, J. Levi, L. Hu, A. Fronda, E. Ambigia, K. McClintock and I. MacLachlan, *The Journal of clinical investigation*, 2009, **119**, 661-673.
17. A. J. Converte, D. S. Benoit, C. L. Duvall, A. S. Hoffman and P. S. Stayton, *Journal of controlled release : official journal of the Controlled Release Society*, 2009, **133**, 221-229.
18. H. Li, S. S. Yu, M. Miteva, C. E. Nelson, T. Werfel, T. D. Giorgio and C. L. Duvall, *Advanced Functional Materials*, 2013, **23**, 3040-3052.
19. S. S. Yu, C. M. Lau, W. J. Barham, H. M. Onishko, C. E. Nelson, H. Li, C. A. Smith, F. E. Yull, C. L. Duvall and T. D. Giorgio, *Molecular pharmaceutics*, 2013, **10**, 975-987.
20. P. Allavena, M. Chieppa, G. Bianchi, G. Solinas, M. Fabbri, G. Laskarin and A. Mantovani, *Clinical & developmental immunology*, 2010, **2010**, 547179.
21. Y. Luo, H. Zhou, J. Krueger, C. Kaplan, S. H. Lee, C. Dolman, D. Markowitz, W. Wu, C. Liu, R. A. Reisfeld and R. Xiang, *The Journal of clinical investigation*, 2006, **116**, 2132-2141.
22. P. D. Stahl and R. A. Ezekowitz, *Current opinion in immunology*, 1998, **10**, 50-55.
23. L. Connelly, A. T. Jacobs, M. Palacios-Callender, S. Moncada and A. J. Hobbs, *The Journal of biological chemistry*, 2003, **278**, 26480-26487.
24. L. A. Dethloff and B. E. Lehnert, *Journal of leukocyte biology*, 1988, **43**, 80-90.
25. M. A. Schonhegrad and P. G. Holt, *Journal of Immunological Methods*, 1981, **43**, 169-173.
26. J. B. Yee and J. C. Hutson, *Biology of reproduction*, 1983, **29**, 1319-1326.
27. A. J. Wilson, W. Barham, J. Saskowski, O. Tikhomirov, L. Chen, H. J. Lee, F. Yull and D. Khabele, *Journal of ovarian research*, 2013, **6**, 63.
28. L. Connelly, W. Barham, H. M. Onishko, L. Chen, T. P. Sherrill, T. Zabuawala, M. C. Ostrowski, T. S. Blackwell and F. E. Yull, *Breast cancer research : BCR*, 2011, **13**, R83.
29. R. Zaynagetdinov, T. P. Sherrill, P. L. Kendall, B. H. Segal, K. P. Weller, R. M. Tighe and T. S. Blackwell, *American journal of respiratory cell and molecular biology*, 2013, **49**, 180-189.
30. D. Pilling, T. Fan, D. Huang, B. Kaul and R. H. Gomer, *PloS one*, 2009, **4**, e7475.
31. W. Xu, N. Schlagwein, A. Roos, T. K. van den Berg, M. R. Daha and C. van Kooten, *European journal of immunology*, 2007, **37**, 1594-1599.
32. P. Szlosarek, K. A. Charles and F. R. Balkwill, *European journal of cancer*, 2006, **42**, 745-750.
33. P. W. Szlosarek and F. R. Balkwill, *The lancet oncology*, 2003, **4**, 565-573.
34. W. Strober, *Current protocols in immunology / edited by John E. Coligan ... [et al.]*, 2001, **Appendix 3**, Appendix 3B.
35. R. Mauisse, D. D. Semir, H. Emamekhoo, B. Bedayat, A. Abdolmohammadi, H. Parsi and D. C. Gruenert, *BMC Biotechnology*, 2010, **10**.
36. F. C. Brosius, 3rd, C. E. Alpers, E. P. Bottinger, M. D. Breyer, T. M. Coffman, S. B. Gurley, R. C. Harris, M. Kakoki, M. Kretzler, E. H. Leiter, M. Levi, R. A. McIndoe, K. Sharma, O. Smithies, K. Suszak, N. Takahashi, T. Takahashi and C. Animal Models of Diabetic Complications, *Journal of the American Society of Nephrology : JASN*, 2009, **20**, 2503-2512.
37. E. Y. Lin, J. G. Jones, P. Li, L. Zhu, K. D. Whitney, W. J. Muller and J. W. Pollard, *The American journal of pathology*, 2003, **163**, 2113-2126.
38. R. D. Leek, R. J. Landers, A. L. Harris and C. E. Lewis, *British journal of cancer*, 1999, **79**, 991-995.
39. K. Greish, *Journal of drug targeting*, 2007, **15**, 457-464.
40. H. Maeda, *Advances in enzyme regulation*, 2001, **41**, 189-207.
41. J. Greenaway, R. Moorehead, P. Shaw and J. Petrik, *Gynecologic oncology*, 2008, **108**, 385-394.
42. T. Hagemann, J. Wilson, F. Burke, H. Kulbe, N. F. Li, A. Pluddemann, K. Charles, S. Gordon and F. R. Balkwill, *Journal of immunology*, 2006, **176**, 5023-5032.
43. E. Schuttyser, S. Struyf, P. Proost, G. Opdenakker, G. Laureys, B. Verhasselt, L. Peperstraete, I. Van de Putte, A. Saccani, P. Allavena, A. Mantovani and J. Van Damme, *The Journal of biological chemistry*, 2002, **277**, 24584-24593.
44. A. Sica, A. Saccani, B. Bottazzi, S. Bernasconi, P. Allavena, B. Gaetano, F. Fei, G. LaRosa, C. Scotton, F. Balkwill and A. Mantovani, *Journal of immunology*, 2000, **164**, 733-738.
45. M. J. Turk, D. J. Waters and P. S. Low, *Cancer letters*, 2004, **213**, 165-172.
46. A. T. Berman, A. D. Thukral, W. T. Hwang, L. J. Solin and N. Vapiwala, *Clinical breast cancer*, 2013, **13**, 88-94.
47. O. B. Garbuzenko, M. Saad, S. Betigeri, M. Zhang, A. A. Vetcher, V. A. Soldatenkov, D. C. Reimer, V. P. Pozharov and T. Minko, *Pharmaceutical research*, 2009, **26**, 382-394.

Macrophage-Specific RNA Interference Targeting via “Click”, Mannosylated Polymeric Micelles

Shann S. Yu,^{†,‡} Cheryl M. Lau,[†] Whitney J. Barham,[§] Halina M. Onishko,[§] Christopher E. Nelson,^{†,‡} Hongmei Li,^{†,‡} Chelsey A. Smith,[†] Fiona E. Yull,[§] Craig L. Duvall,^{†,‡} and Todd D. Giorgio*,^{†,‡,§,||}

[†]Department of Biomedical Engineering, Vanderbilt University, Nashville, Tennessee 37235, United States

[‡]Vanderbilt Institute for Nanoscale Science and Engineering, Vanderbilt University, Nashville, Tennessee 37235, United States

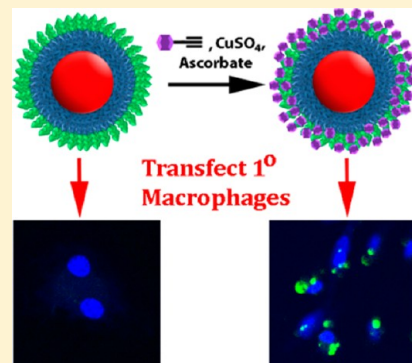
[§]Department of Cancer Biology, Vanderbilt-Ingram Cancer Center, Nashville, Tennessee 37232, United States

^{||}Department of Chemical and Biomolecular Engineering, Vanderbilt University, Nashville, Tennessee 37235, United States

Supporting Information

ABSTRACT: Macrophages represent an important therapeutic target, because their activity has been implicated in the progression of debilitating diseases such as cancer and atherosclerosis. In this work, we designed and characterized pH-responsive polymeric micelles that were mannosylated using “click” chemistry to achieve CD206 (mannose receptor)-targeted siRNA delivery. CD206 is primarily expressed on macrophages and dendritic cells and upregulated in tumor-associated macrophages, a potentially useful target for cancer therapy. The mannosylated nanoparticles improved the delivery of siRNA into primary macrophages by 4-fold relative to the delivery of a nontargeted version of the same carrier ($p < 0.01$). Further, treatment for 24 h with the mannose-targeted siRNA carriers achieved $87 \pm 10\%$ knockdown of a model gene in primary macrophages, a cell type that is typically difficult to transfect. Finally, these nanoparticles were also avidly recognized and internalized by human macrophages and facilitated the delivery of 13-fold more siRNA into these cells than into model breast cancer cell lines. We anticipate that these mannose receptor-targeted, endosomolytic siRNA delivery nanoparticles will become an enabling technology for targeting macrophage activity in various diseases, especially those in which CD206 is upregulated in macrophages present within the pathologic site. This work also establishes a generalizable platform that could be applied for “click” functionalization with other targeting ligands to direct siRNA delivery.

KEYWORDS: mannose, nanoparticles, macrophages, siRNA, drug delivery, immunotherapy



INTRODUCTION

Macrophages perform diverse functions, some of which have cytotoxic effects (i.e., when fighting infection) and others that promote cell growth, matrix remodeling, and wound healing.¹ However, the dysregulation of these multifaceted activities can initiate pathogenesis and promote disease progression. For example, in many cancers, significant levels of resident macrophages have been observed, and this has been correlated with poor prognoses.² This is hypothesized to occur because tumor-associated macrophages (TAMs) overexpress angiogenic growth factors such as VEGF, and matrix-remodeling enzymes, including cathepsins and metalloproteinases, promoting tumor growth and invasiveness.³ Macrophages also secrete immunosuppressive cytokines, including IL-10 and TGF- β , which discourage the infiltration of antitumor lymphocytes and further promote an environment conducive to unchecked tumor progression.⁴ Therefore, macrophages potentially represent a viable therapeutic target that can address a major underlying cause of cancer progression. On the basis of this hypothesis, technologies that allow cell-specific phenotypic modulation of aberrant macrophage activity would have an especially strong impact in cancer research.

A promising strategy for reprogramming macrophage behavior is through the use of RNA interference (RNAi) therapy. One approach to therapeutically harnessing RNAi involves the delivery of small interfering RNA (siRNA). siRNA is processed by the target cell's inherent transcriptional regulation machinery, with the ultimate effect of gene silencing through cleavage and degradation of mRNA complementary to the antisense strand of the delivered siRNA duplex.⁵ By silencing master genes that regulate undesirable macrophage activity, RNAi therapy has the potential to directly block macrophage functions that lead to disease progression. A number of studies in genetically engineered knockout models suggest that genes within the Jak/Stat pathways drive pathologic macrophage polarization and activity in a variety of diseases.^{6–9} Recently, Kortylewski et al. showed that siRNA-mediated silencing of Stat3 in tumor-infiltrating leukocytes drove immune-mediated tumor rejection.¹⁰ In a related

Received: August 7, 2012

Revised: December 20, 2012

Accepted: January 19, 2013

approach, it has also been shown that siRNA-mediated knockdown of CCR2 in monocytes weakens their ability to enter tumor sites, resulting in fewer TAMs and reduced tumor volumes.¹¹ Finally, in a study aimed at reducing the level of classically activated, pro-inflammatory macrophages, Aouadi et al. showed that siRNA-mediated silencing of Map4k4 suppressed systemic inflammation by reducing the level of production of TNF α by macrophages.¹² The authors note that this approach can be applied to autoimmune diseases and atherosclerosis, where classically activated macrophages promote disease progression. These studies provide a strong precedent for the use of RNAi to modulate macrophage function and further motivate the broad applicability of macrophage-targeted siRNA nanocarriers for the treatment of a variety of diseases.

Because of their highly degradative phagocytic, endosomal, and lysosomal compartments, delivery and cytoplasmic release of siRNA in macrophages are particularly challenging, especially in primary cells.¹³ Conventional transfection methods have led to limited success, because many of these methods are based on strongly cationic materials that can be cytotoxic and have been largely restricted to the laboratory bench.¹⁴ While strategies exist for targeting macrophages at pathologic sites, some of these strategies require prior knowledge of their locations so that local delivery can be achieved by injection directly into the site of the macrophages.^{10,15} For example, intratumoral or peritumoral injections may be useful when treating a primary tumor site but are poorly translated to the treatment of dispersed, metastatic cancers. Alternative strategies require expensive technologies with uncertain practical clinical applicability, such as macrophage extraction, ex vivo modification, and adoptive transfer;⁸ antibody–nanoparticle conjugates;^{16,17} or custom phospholipids,¹⁸ as reviewed elsewhere.¹⁹ Very few of these proposed approaches can be practically scaled for pharmaceutical purposes. Some of these methods deliver drugs to multiple cell types nonspecifically, and systemic interference with macrophage behavior may lead to unintended side effects, including autoimmune manifestations. Therefore, the clinical translation of macrophage-targeted drug delivery is complicated by barriers, including targeting method, synthesis, and cost.

We designed and evaluated a polymeric glycoconjugate that can be assembled into pH-responsive, endosomolytic nanocarriers for macrophage-specific siRNA delivery (Figure 1). These agents expand on a nontargeted polymeric formulation previously reported by Convertine et al.,²⁰ which is capable of mediating the escape of its cargo from the endosomal pathway, because of their ability to disrupt phospholipid membranes in the acidic environment characteristic within late endosomes (pH <6.5).

The macromolecular structure includes a hydrophobic, pH-responsive block, a cationic, siRNA-condensing block, and a terminal block with reactive sites for “click” bioconjugation (Figure 1). These multifunctional polymers were synthesized via reverse addition–fragmentation chain transfer (RAFT) polymerization, which has the advantage of allowing the polymerization of a variety of monomers displaying a wide range of chemical functionalities.²¹ Additionally, RAFT yields highly monodisperse polymers and is an industrially scalable method, making it appropriate for pharmaceutical applications. In aqueous media at pH 7.4, the polymers self-assemble into stable micelles that can be surface-functionalized with a wide range of possible molecular structures through the azide–

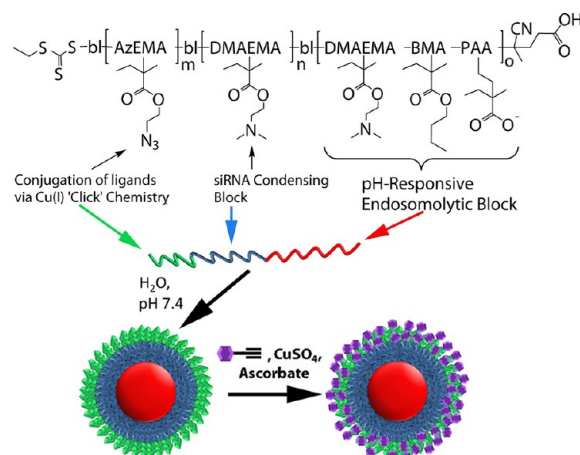


Figure 1. Smart polymeric nanoparticles for mannose receptor-targeted cytosolic delivery of siRNA. Schematic representation of the triblock copolymers and formulation into multifunctional nanoscale siRNA delivery vehicles. The blocks include a pH-responsive block that is capable of disrupting endosomes at low pH (red), a cationic block for condensation of nucleic acids (blue), and an azide-displaying block (green) for conjugation of targeting motifs (purple) via click chemistry.

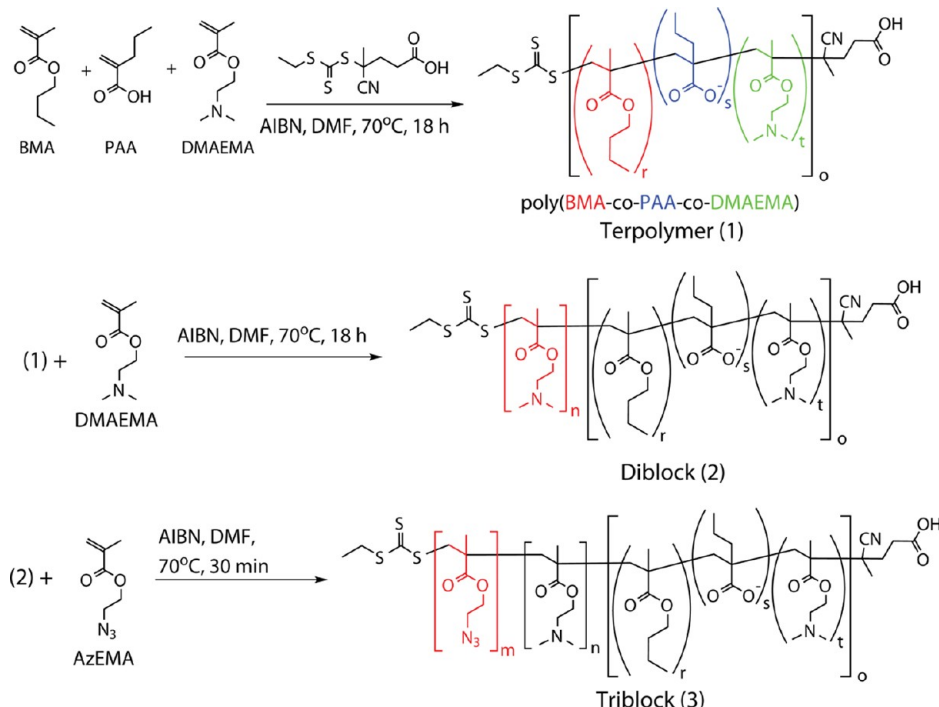
alkyne click reaction chemistry. Because of their orthogonality, specificity, speed, and efficiency,²² “click” reactions have been widely employed to perform covalent conjugations for biological applications.

Mannose was chosen as the targeting motif, because mannose receptor (CD206) is primarily expressed by alternatively activated, M2-like macrophages and some dendritic cells.^{23,24} In these cells, CD206 mediates the recognition and endocytosis of mannosylated, fucosylated, or N-acetylglucosaminated substrates, which occurs via clathrin-coated vesicles.²⁵ While most macrophages express low baseline levels of CD206, mannose receptor is upregulated in TAMs, and the potential to directly target this specific macrophage subset via mannose has not been explored.^{4,26} Mannose is also readily available at significantly lower costs than most alternative targeting motifs (i.e., antibodies and peptides), improving the practicality of the approach. We believe that coupling mannose-mediated targeting with pH-responsive endosomolytic polymers will lead to a reliable and translatable platform for macrophage-targeted RNAi therapies and investigational reagents.

In this study, the capabilities of the mannose receptor-targeted nanoparticles (ManNPs) were evaluated for cytosolic delivery and gene knockdown in primary, murine bone marrow-derived macrophages (BMDMs). The specificity of the carriers was examined on the basis of the ability of the glycoconjugated nanoparticles to preferentially deliver siRNA into immortalized human macrophages relative to cancer cell lines. Results support the idea that the described carrier offers significant opportunities for targeting of drugs and siRNA to TAMs.

EXPERIMENTAL SECTION

Materials. All reagents and materials were purchased from Sigma-Aldrich (St. Louis, MO) and used as received unless described otherwise. Monomers for radical polymerization, including BMA, DMAEMA, PAA, and AzEMA, were all purified by vacuum distillation and stored at 4 °C in

Scheme 1. RAFT Polymerizations^a

^aSynthetic scheme for RAFT polymerization of triblock copolymers composed of blocks of 2-azidoethyl methacrylate (AzEMA), 2-dimethylaminoethyl methacrylate (DMAEMA), and the BMA-co-PAA-co-DMAEMA terpolymer (BMA, butyl methacrylate; PAA, 2-propylacrylic acid).

inhibitor-free containers. Riboshredder RNase blend was purchased from Epicenter (Madison, WI). Immortalized cell lines were acquired from American Type Culture Collection (Manassas, VA). Cell culture supplies, including media, fetal bovine serum, antibiotics, and nonessential amino acids, were obtained from Life Technologies (Carlsbad, CA). The following siRNA sequences were purchased for transfections: FAM-labeled anti-GAPDH siRNA (FAM-siRNA, Life Technologies) and anti-PPIB siRNA (Integrated DNA Technologies, Coralville, IA). Horse serum was purchased from Atlanta Biologicals (Norcross, GA).

Synthesis of 2-Azidoethyl Methacrylate (AzEMA). In a 500 mL round-bottom flask, 15.6 g of sodium azide (0.24 mol) was dissolved in 100 mL of nanopure water, followed by the addition of 5.67 mL of 2-bromoethanol [10 g, 0.08 mol (Figure S1 of the Supporting Information)]. After the flask had been capped with a septum, the reaction mixture was heated to 80 °C and allowed to stir overnight, during which the color of the reaction mixture changed from yellow to orange. Next, the reaction mixture was allowed to cool to room temperature, and the product was extracted four times with 75 mL of diethyl ether. Following two extractions, the color of the aqueous phase changed from orange to clear. The pooled organic fractions were concentrated by rotary evaporation to yield pure 2-azidoethanol (>90% by HPLC, UV trace at 215 nm), which is a clear, colorless oil: 95% yield (6.66 g, 27.6137 g – 20.9532 g); ¹H NMR [400 MHz, (CD₃)₂SO] δ 3.20–3.27 (t, 2H, CH₂N₃), 3.44 (s, 1H, OH), 3.54–3.60 (q, 2H, CH₂O); FT-IR (KBr pellet) 3380 (broad, O–H), 2100 (N₃), 1295 (C–N), 1050 cm⁻¹ (C–O).

In a round-bottom flask, 10 g of 2-azidoethanol (0.11 mol) was mixed with 30.6 mL of Et₃N (22.3 g, 0.22 mol) in 50 mL of CH₂Cl₂ in a dry ice/acetone bath [–78 °C (Figure S1 of the

Supporting Information)]. The reaction vessel was capped with a septum and degassed by alternating evacuation of the vessel and equilibration with nitrogen gas (six times). Next, 8.6 mL of methacryloyl chloride (9.2 g, 0.088 mol) was injected into the system dropwise, and the reaction was allowed to proceed overnight. **Caution:** Azide compounds may become shock-sensitive above 75–80 °C, and this step is highly exothermic. The dry ice/acetone bath was allowed to warm to room temperature during this reaction. The crude product was extracted three times with 1 N hydrochloric acid to remove excess Et₃N, extracted twice with 1 N aqueous NaOH, and precipitated in nanopure water. After the organic fraction had been dried over MgSO₄, the product was concentrated under rotary evaporation to yield a dark red-orange liquid, which was further distilled under high vacuum to produce pure 2-azidoethyl methacrylate. RAFT polymerization kinetics of AzEMA are shown in Figure S2 of the Supporting Information: ¹H NMR (400 MHz, CDCl₃) δ 1.97 (s, 3H, CH₃), 3.5 (t, 2H, CH₂N₃), 4.33 (t, 2H, CH₂O), 5.62 (s, 1H), 6.18 (s, 1H).

Synthesis of Alkyne-Functionalized Mannose. The reaction diagram is shown in Figure S3A of the Supporting Information. In a round-bottom flask, 11 g of D-mannose (60 mmol) was dissolved in 30 mL of dimethyl sulfoxide (DMSO). To activate the sugar into a nucleophile, 10 mL of Et₃N (triethylamine, 72 mmol) was added to the reaction mixture, followed by the addition of 5 g of propargyl chloride (67 mmol). After the mixture had been purged with argon, the reaction proceeded for 24 h at 40 °C. Excess reagents were removed by extraction into diethyl ether (five times). The remaining ether-insoluble phase was dissolved into nanopure water and further extracted five times with dichloromethane to remove other byproducts and DMSO. The product was flash-frozen in liquid N₂ and lyophilized. HPLC characterization and

Table 1. Characterization of Polymers Synthesized via RAFT Polymerization

polymer	abbreviation	dn/dc (mL/g) ^a	target M_n (Da)	M_n (Da) ^b	M_w (Da) ^b	PDI	D_h (nm)	ζ -potential (mV)
poly(BMA-co-PAA-co-DMAEMA) ^c	terpolymer	0.081	14000	11400	13900	1.22		
poly(BMA-co-PAA-co-DMAEMA)-bl-poly(DMAEMA)	diblock	0.049	21000	16800	20700	1.23	32.2 ± 6.8	15.0 ± 5.3
poly(BMA-co-PAA-co-DMAEMA)-bl-poly(DMAEMA)-bl-poly(AzEMA)	triblock	—	22000	22300	28900	1.29	28.0 ± 1.5	19.6 ± 11.7

^aMeasured in off-line batch mode in a Shimadzu RID-10A differential refractive index (dRI) detector, with DMF and 0.1 M LiBr as the solvent.

^bMeasured via gel-permeation chromatography with MALS and dRI in-line with columns. ^cThe terpolymer was insoluble in aqueous buffer at pH 7.4, so no D_h or ζ -potential could be measured via DLS.

¹H and ¹³C NMR are presented in Figure S3B–D of the Supporting Information.

RAFT Polymerizations. Syntheses of the RAFT chain transfer agent (CTA) 4-cyano-4-(ethylsulfanylthiocarbonyl)-sulfanylpentanoic acid (ECT) and 2-propylacrylic acid monomer have been described in detail previously.^{20,27} Block copolymers were synthesized on the basis of the reaction shown in Scheme 1.

Polymerization of the 47%BMA–25%PAA–28%DMAEMA terpolymer (**1** in Scheme 1, compositions based on the ¹H NMR of the product; target composition was 50%BMA–25%PAA–25%DMAEMA) was conducted at 70 °C under N₂ for 18 h with DMF as the solvent (90 wt % in feed), an initial monomer:CTA molar ratio of 100, and a CTA:initiator molar ratio of 10. After the reaction mixture had been rapidly cooled in an ice bath, the organic mixture was mixed in a 1:1 ratio (by volume) with aqueous HCl at pH 2, which initially results in a turbid mixture that quickly turns clear-yellowish. Next, the polymer was precipitated seven times in hexanes and twice in diethyl ether to remove residual, unreacted monomers. Finally, the polymers were dialyzed across a 10 kDa molecular mass cutoff membrane (Pierce, Rockford, IL) against nanopure water (pH 5) overnight. Lyophilization yielded the pure terpolymer, which was a yellowish powder (Table 1).

The same monomer:macroCTA:I molar ratios and 90 wt % DMF conditions were used to polymerize the DMAEMA block onto the terpolymer macroCTA (**1**). To purify the poly(BMA-co-PAA-co-DMAEMA)-bl-poly(DMAEMA) diblock copolymers (**2** in Scheme 1, henceforth termed diblock), the reaction mixture was precipitated in diethyl ether at –20 °C for 1 h and then pelleted by centrifugation at 800g for 5 min. The polymer was dialyzed against deionized water for 48 h using a 10 kDa molecular mass cutoff membrane, and lyophilization yielded a light yellow powder.

Finally, the AzEMA block was polymerized from the diblock (**2**) to form poly(BMA-co-PAA-co-DMAEMA)-bl-poly(DMAEMA)-bl-poly(AzEMA) triblock copolymers (**3** in Scheme 1, henceforth termed triblock) using similar reaction conditions. This mixture was then dialyzed against nanopure water across a 10 kDa molecular mass cutoff membrane overnight to yield pure triblock. The triblock copolymer was dissolved in deionized water at a concentration of 1 mg/mL and stored at –20 °C until it was ready for use in click reactions.

¹H NMR spectra for all polymers are shown in Figure S4 of the Supporting Information.

Mannose Click Functionalization. In a scintillation vial, 1 mL of poly(BMA-co-PAA-co-DMAEMA)-bl-poly(DMAEMA)-bl-poly(AzEMA) copolymer (**3**, 1 mg/mL in nanopure H₂O) was mixed with 6 mg of alkyne-functionalized mannose (27.5 mmol). After the addition of CuSO₄ and sodium ascorbate to final concentrations of 1 and 5 mM, respectively, the reaction

was allowed to proceed at 37 °C on an orbital shaker in the dark for 48 h. Excess copper was removed by treating the crude product with Chelex 100 Resin (Bio-Rad Laboratories, Hercules, CA) according to the manufacturer's instructions. The product was filtered through a 0.45 μm Teflon filter to remove the resin and then dialyzed through a 2 kDa molecular mass cutoff membrane against deionized water to remove excess reactants. Lyophilization yielded the ManNPs, which were reconstituted in nuclease-free water at a concentration of 1–4 mg/mL before being used in experiments. ¹H NMR characterization of the micelles before and after click chemistry is shown in Figure S5 of the Supporting Information.

Characterization of Polymer-Mediated siRNA Complexation and Nuclease Protection. FAM-labeled siRNA (50 pmol) was complexed with mannosylated nanoparticles at N:P (NH⁺:PO₄[–]) ratios of: 1:2, 1:1, 2:1, and 4:1. Ratios were calculated by using the concentration of NH⁺ (based on the degree of polymerization of the DMAEMA homopolymer block) and PO₄[–] (based on the number of siRNA base pairs). Because the pK_a of DMAEMA is ~pH 7.5, we assumed that the DMAEMA polymer block was 50% charged for the calculation of N:P ratios. The complexes were loaded onto a 2% agarose gel containing 1.5 μM ethidium bromide.

By measuring the hyperchromic effect, protection of siRNA from RNase degradation was assessed in untargeted nanoparticles comprised of the diblock copolymers or mannosylated nanoparticles (1:2 or 4:1 N:P ratios), as described previously.²⁸

Hemolysis Assays. Assays were performed as described previously.²⁹ Briefly, human blood samples were obtained from consenting, anonymous, healthy adults under a protocol approved by the Vanderbilt University Institutional Review Board (IRB). Plasma was removed, and RBCs were washed with 150 mM NaCl. RBCs were ultimately diluted into phosphate buffers adjusted to pH 5.6, 6.2, 6.8, or 7.4, and the percent hemolysis in these buffers was assessed for polymers at concentrations of 1, 5, and 40 μg/mL. PBS (negative control) or 20% Triton X-100 (positive control) was used as a control. Polymer/RBC solutions were incubated at 37 °C in a 5% CO₂ incubator for 1 h and centrifuged at 1500 rpm for 5 min, and supernatants were transferred to a new plate. The percent RBC lysis was quantified on the basis of the absorbance at 450 nm relative to samples treated with Triton X-100 (assume 100% lysis) and PBS (to subtract background absorbance).

Animals and Cell Lines. Animal work was approved by the Vanderbilt University Institutional Animal Care and Use Committee. All mice were on an FVB background strain. Bone marrow-derived macrophages were isolated from tibiae and femurs immediately after the mice had been sacrificed and cultured as described previously.³⁰ Cells were seeded at a density of 300000 cells/cm² for all experiments. Detailed information about culturing of immortalized cell lines can be found in the Supporting Information.

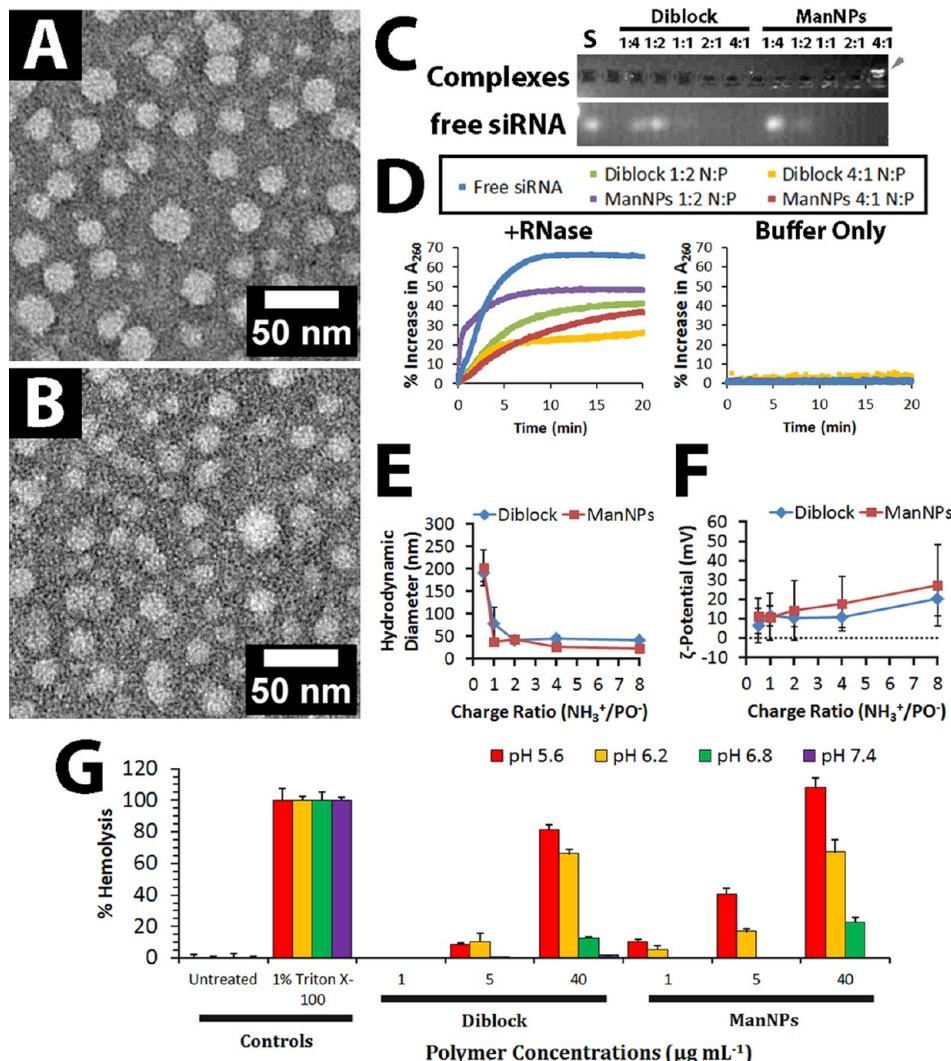


Figure 2. Morphologic and functional characterization of micelles composed of diblock copolymers and mannosylated triblock copolymers. (A and B) Uranyl acetate-counterstained transmission electron micrographs. (A) Dehydrated micelles of diblock copolymers (see 2 in Scheme 1) had an average diameter of 13.0 ± 6.1 nm ($n = 367$). (B) Dehydrated ManNPs had an average diameter of 9.7 ± 6.2 nm ($n = 415$). Scale bars are 50 nm. (C) Gel retardation assay of siRNA-loaded ManNPs confirmed an increased level of complexation of siRNA with increasing N:P ratios. Free FAM-labeled siRNA (S) appears as a control. (D) Protection of siRNA from degradation by RNases. Micelle–siRNA complexes were incubated with RNase cocktails. RNase-mediated degradation of siRNA was characterized by a hyperchromic effect at 260 nm, and within 10–15 min, all siRNA in each sample had completely degraded as signified by asymptotic behavior of the results. siRNA and micelle–siRNA complexes that were left in buffer without RNases did not exhibit this hyperchromic effect. (E and F) Dynamic light scattering was used to analyze the (E) hydrodynamic diameters and (F) ζ -potentials of the polymeric micelles following complexation with siRNA. (G) Both polymers exhibit pH- and concentration-dependent hemolysis, with minimal disruption of erythrocyte phospholipid membranes at physiologic pH, but an increased level of disruption in pH ranges mimicking the endosomal pH (pH < 6.5). Error bars represent the standard deviation of four replicates.

Transfections. ManNP formulations were prepared as described above, and Lipofectamine RNAiMAX (Life Technologies) was used according to the manufacturer's instructions as a commercially available benchmark. Cells were rinsed twice with PBS and given serum-free medium, which is composed of DMEM with 4.5 g/L glucose, 1 unit/mL penicillin, 1 $\mu\text{g/mL}$ streptomycin, and 2 mM L-glutamine. Complexes were then added to the wells such that the final concentration of siRNA in the wells was 50 nM (10-fold dilution from stock). For some experiments, cells were co-incubated with complexes and 100 mg/mL free D-mannose (Sigma-Aldrich) to examine the CD206 dependence of nanoparticle-mediated siRNA delivery. At set time points, wells were rinsed with PBS and processed according to the desired experiment as described below.

Transfected cells were analyzed for cell viability using a Live-Dead kit (Life Technologies) according to the manufacturer's instructions. Quantification of live and dead cells was conducted by flow cytometry.

Quantitative Real-Time PCR. Total RNA was isolated from cell samples using the RNeasy Kit and QiaShredder columns (Qiagen). After the removal of genomic contamination through DNase treatment (DNA-free kit, Life Technologies), cDNA libraries were constructed using a reverse transcriptase kit (Life Technologies).

For qRT-PCR, primers were purchased from Integrated DNA Technologies: PPIB, 5'-TTCCATCGTGTCAAG-3' (sense) and 5'-GAAGAACTGTGAGCCATT-3' (antisense); GAPDH, 5'-TGAGGACCAGGTTGTCTCCT-3' (sense) and 5'-CCCTGTTGCTGTAGCCGTAT-3' (antisense). qRT-PCR

was conducted using SYBR Green PCR Master Mix. Details of data analysis for relative GAPDH expression can be found in the Supporting Information.

Flow Cytometry. Flow cytometry was performed on a BD (Franklin Lakes, NJ) FACSCalibur system, operated via BD Cellquest Pro, version 5.2. The FL1 channel (emission filter at 530 ± 15 nm) was used for the quantification of the FAM emission of each cell.

Confocal Microscopy. Transfections were performed as described above for 1, 2, or 4 h. To prepare cells for confocal microscopy, they were washed with PBS, fixed for 15 min with 10% buffered formalin, rinsed three times with PBS, and then stained with DAPI (Invitrogen, Carlsbad, CA) for 10 min. After the cells had been rinsed three times with PBS, slides were mounted with the Invitrogen ProLong Antifade kit. Imaging was performed on a Zeiss (Oberkochen, Germany) LSM 710 system. Image processing is described in the Supporting Information.

Statistical Analysis. For all experiments, statistical significance was assessed using the unpaired Student's *t* test or one-way ANOVA as appropriate and indicated in the text, with $p < 0.05$ considered significantly different.

■ RESULTS

Modular Design, Synthesis, and Characterization of Mannosylated siRNA Delivery Vehicles. The synthesis of the mannosylated delivery vehicles was successfully completed through three stages. (I) The polymeric components were synthesized in three sequential iterations of RAFT polymerization and purification (Figure 1 and Scheme 1). (II) Alkyne-functionalized mannose was separately synthesized (Figure S3 of the Supporting Information). (III) The polymers from stage I are formed into micelles and reacted with the alkyne-functionalized mannose from stage II. These steps result in immobilization of mannose onto the micelle corona through reaction with the distal azide groups via click chemistry (Figure 1).

The polymers that make up the ManNPs were synthesized via RAFT polymerization. These modules include a pH-responsive block (Figure 1, red), a cationic block for condensing nucleic acids (blue), and an azide-presenting block (green) for the attachment of alkyne-functionalized ligands. First, a ~ 14 kDa random terpolymer block composed of 47% butyl methacrylate (BMA), 25% 2-propylacrylic acid (PAA), and 28% 2-dimethylaminoethyl methacrylate (DMAEMA) was synthesized (Scheme 1 and Table 1). The percentages represent the molar composition of each monomer in the copolymer structure, as determined by ^1H NMR (Figure S4 of the Supporting Information). The terpolymer forms a turbid suspension upon being exposed to aqueous media at pH 7.4 but dissolves effectively when the pH is lowered to <6.0 , consistent with the pH-sensitive characteristics of this block.

To form a hydrophilic, corona-forming segment, a cationic DMAEMA block (8.9 kDa by ^1H NMR) was polymerized from the terpolymer macroCTA, yielding a diblock copolymer [22.8 kDa (Figure 1, red and blue, and Table 1)]. This diblock copolymer self-assembles into micellar nanoparticles upon being exposed to aqueous media (Figure 2A), consistent with previous work by others.^{20,31–33} Diameters of the diblock copolymer micelles were measured to be 13.0 ± 6.1 nm in a dehydrated state by TEM and 32.2 ± 6.8 nm in a hydrated state by DLS.

Finally, an azide-presenting block composed of 2-azidoethyl methacrylate (AzEMA) was extended from the DMAEMA terminus of these polymers (Figure S4 of the Supporting Information). The synthetic route for AzEMA (Figure S1 of the Supporting Information) was modified from published schemes for the synthesis of 3-azidopropyl methacrylate, a similar monomer.^{34,35} The controlled polymerization kinetics of AzEMA are also presented (Figure S2 of the Supporting Information).

The resulting triblock copolymers retained the ability to self-assemble into micelles in aqueous media. Morphologically, the triblock copolymers are expected to form assemblies as depicted in Figure 1, where the azide-presenting block effectively shields the DMAEMA block in the final micellar structures. Because addition of the final, AzEMA block to the base diblock leads to a 4 nm decrease in the hydrodynamic diameter of the resulting micelles and a slight increase in the ζ -potential (Table 1), NMR spectra of the micelles were obtained in D_2O to improve our understanding of the particle morphology in aqueous environments (Figure S4 of the Supporting Information). The base diblock micelles [poly-(BMA-co-PAA-co-DMAEMA)-bl-poly(DMAEMA), 2] featured peaks in chemical shift regions characteristic of pure poly(DMAEMA), while the micelles composed of the triblock [poly(BMA-co-PAA-co-DMAEMA)-bl-poly(DMAEMA)-bl-poly(AzEMA), 3] produced peaks corresponding to the azido protons in addition to poly(DMAEMA) peaks (Figures S4 and S5 of the Supporting Information). Therefore, micelles consisting of the diblocks display a corona of DMAEMA, while the triblock copolymers form micelles that present azide groups at their corona, allowing the facile immobilization of alkyne-functionalized ligands onto the micelles.

The synthesis of alkyne-functionalized mannose (Figure S3A of the Supporting Information) was adapted from a synthetic scheme for derivatized sugars presented by Plotz and Rifai.³⁶ The resulting NMR spectra of the product indicated the successful alkyne functionalization of the monosaccharide (Figure S3C,D of the Supporting Information). HPLC confirmed that the product is 70–80% pure following synthesis. No further purification was conducted, and nonfunctionalized mannose was subsequently removed via dialysis of the final ManNPs.

Following the click reaction to functionalize the polymers with mannose, the polymers retained the ability to form micellar nanoparticles, similar to those formed by the diblock copolymers lacking the azide block and mannose (Figure 2A,B). The ManNPs exhibited diameters of 9.7 ± 6.2 nm in a dehydrated state by TEM and 21.8 ± 2.6 nm in a hydrated state by DLS. The ManNPs also exhibited a distinct NMR signature compared to that of the micelles made of triblock copolymer before the click mannosylation reaction (Figure S5 of the Supporting Information). This is particularly evident in the 3.2–3.7 ppm region, where the appearance of peaks corresponding to mannose is consistent with the success of the click reaction.

ManNPs Form Complexes with siRNA and Protect Cargo from Degradation. Like the diblock copolymers, the completed ManNPs are able to complex siRNA in an N:P ratio-dependent fashion as evidenced by a gel retardation assay (Figure 2C). The brightness of the free, uncomplexed siRNA band apparent in the gel decreased with an increased N:P ratio. We also performed experiments to characterize the ability of ManNPs to protect siRNA cargo from nuclease degradation

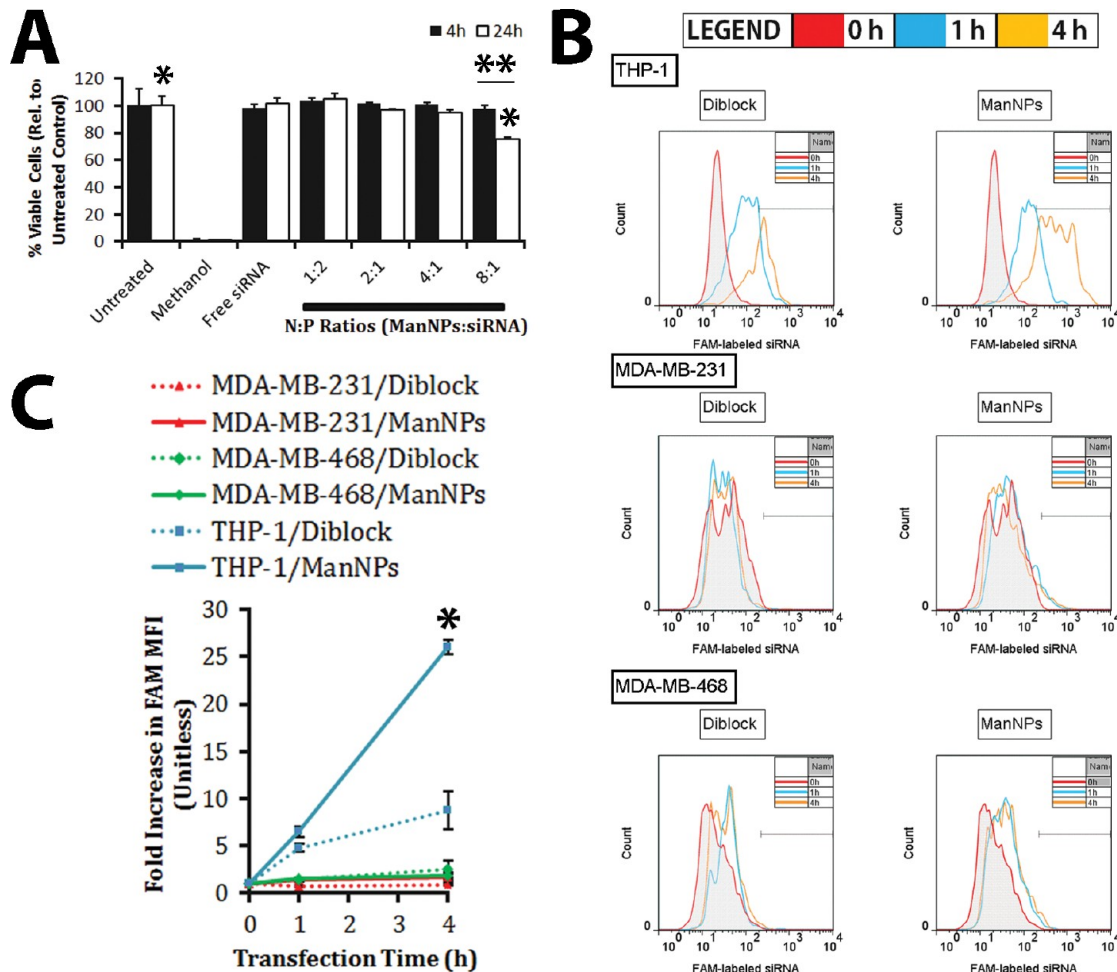


Figure 3. ManNPs are cytocompatible and selectively enhance the delivery of siRNA into immortalized human macrophages. (A) Cytotoxicity assay of immortalized THP-1 macrophages, treated with ManNPs complexed with siRNA at various N:P ratios. Error bars represent the standard deviation from three experiments (*, ** $p < 0.01$; $n = 3$). (B) Representative flow cytometry histograms of THP-1, MDA-MB-231, and MDA-MB-468 cells 0 (red), 1 (blue), or 4 h (orange) after transfection with FAM-siRNA loaded into diblock micelles (left) or ManNPs (right). (C) Mean fluorescence intensities of all of the groups in panel B have been quantified and are shown. Error bars represent the standard deviation of three experiments. ManNPs enhanced the delivery of siRNA into macrophages up to 26-fold over two model breast cancer cell lines and 3-fold in macrophages relative to untargeted diblock carriers, as measured via flow cytometry (* $p < 0.01$ vs all other treatment groups at the 4 h time point).

(Figure 2D). In this study, the degradation of siRNA results in a hyperchromic effect, which is characterized by increased sample absorbance at 260 nm.²⁸ The 65% increase in Abs_{260} of free siRNA within 10 min of RNase treatment is a demonstration of this effect and is used as a positive control. The same siRNA incubated in buffer alone did not exhibit this trend, confirming that RNase activity is necessary for the hyperchromic effect. Both polymers were able to protect their cargo from rapid degradation by RNases, and this ability is enhanced at higher N:P ratios.

Finally, dynamic light scattering confirmed that the hydrodynamic diameter of the siRNA–polymer complexes increased with a decreasing N:P ratio [less polymer per siRNA, from 8:1 to 1:2 (Figure 2E)]. However, at N:P ratios of <2 , these complexes became less stable, and >100 nm diameter aggregates were measured. Decreasing N:P ratios also corresponded to decreasing nanoparticle ζ -potential (Figure 2F). Both polymers formed complexes with siRNA that exhibited ζ -potentials of <25 mV, and these complexes remain colloidally stable if left at room temperature for at least 24 h without any observable flocculation.

ManNPs Exhibit pH-Dependent Hemolysis and Are Cytocompatible.

We next sought to investigate the ability of the ManNPs to create pH-dependent membrane disruption of red blood cells as a surrogate measure for escape from acidified endosomes following endocytotic uptake. Erythrocyte hemolysis assays are commonly employed to model polymer–endosome interactions because relative membrane disruption can be quantified through the release of hemoglobin from the cells (Figure 2G).²⁹ Neither the diblock nor the ManNPs caused significant levels of hemolysis at pH 7.4 (1.8 ± 2 and $0.0 \pm 0.1\%$, respectively, at a $40 \mu\text{g/mL}$ dose, relative to detergent-treated erythrocytes; $n = 4$). However, as the environmental pH was decreased to 6.2, significantly higher levels of hemolysis were measured (66.1 ± 2.7 and $67.3 \pm 7.6\%$ for diblocks and ManNPs, respectively). This effect was even greater at pH 5.6 ($81.5 \pm 3.1\%$ for diblock and $108.2 \pm 6.1\%$ for ManNPs), which is similar to pH ranges encountered in late endosomes and lysosomes.²⁹ These data suggest that, during circulation, the nanoparticles are unlikely to cause adverse effects because of cell membrane lysis. Importantly, these results also suggest that, following endocytosis, the polymeric components will be

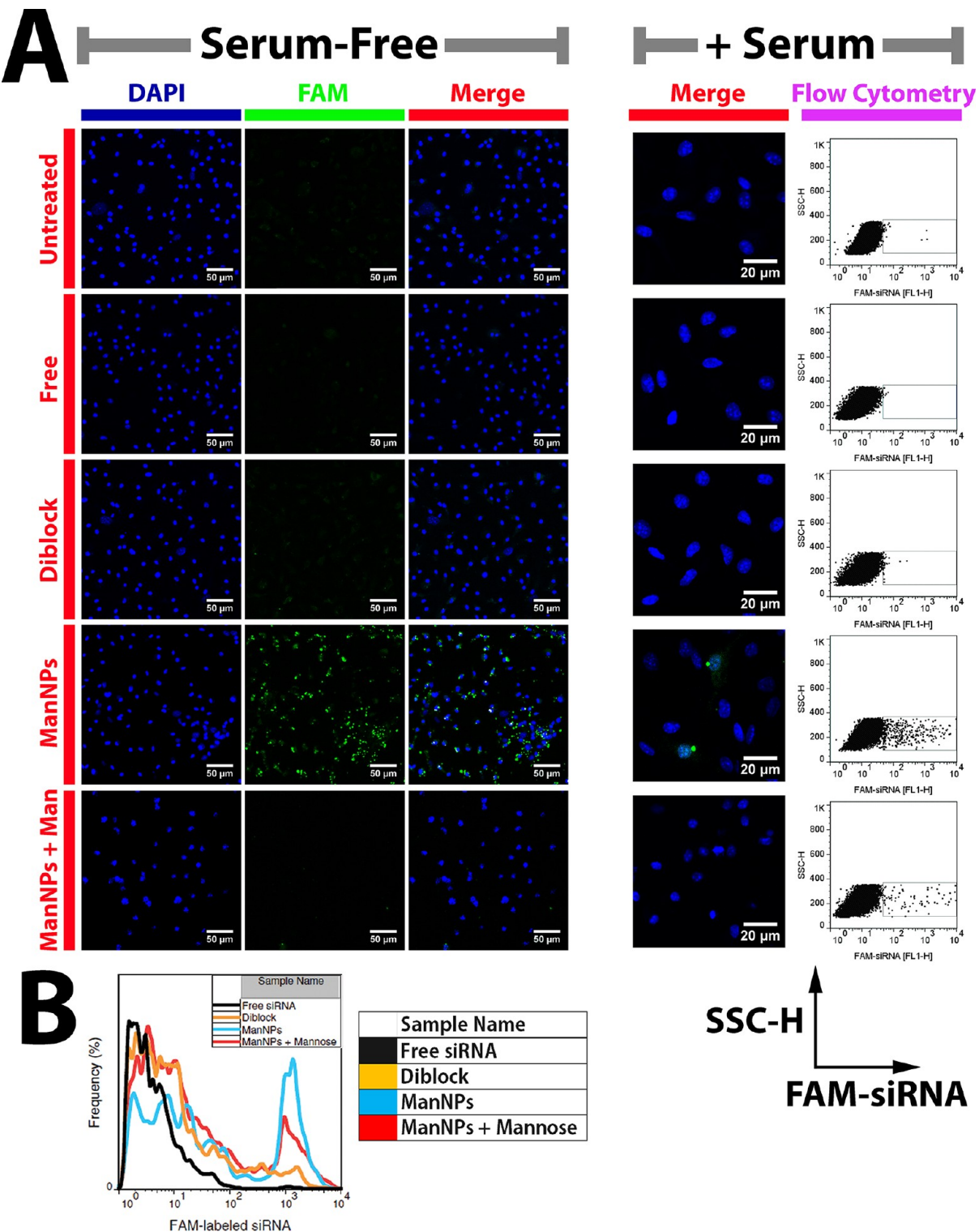


Figure 4. CD206-dependent delivery of siRNA to primary macrophages using ManNPs. (A) Following transfection with FAM-siRNA for 4 h (green; free or complexed into nanoparticles), BMDMs were fixed, and nuclei were stained with DAPI (blue) and imaged via confocal microscopy. Scale bars are 50 μ m for serum-free and 20 μ m for serum. Mannosylation of the polymeric vehicles enhanced their internalization by BMDMs. This could be competitively inhibited through co-administration of the ManNPs with D-mannose. A similar trend was observed when transfections were performed under serum conditions. The FAM brightness and contrast were enhanced equally for all samples with serum but unaltered for the serum-free condition. For the serum-free condition, the brightness and contrast were also enhanced in the DAPI channel to account for small differences in staining between samples. (B) Flow cytometry quantification of delivery of FAM-siRNA into BMDMs via ManNPs (blue) relative to untargeted nanoparticles (orange) or free siRNA without vehicle (black) within 4 h of administration under serum-free conditions. Quantification of mean fluorescence intensity in each treatment group is shown in Figure S6 of the Supporting Information.

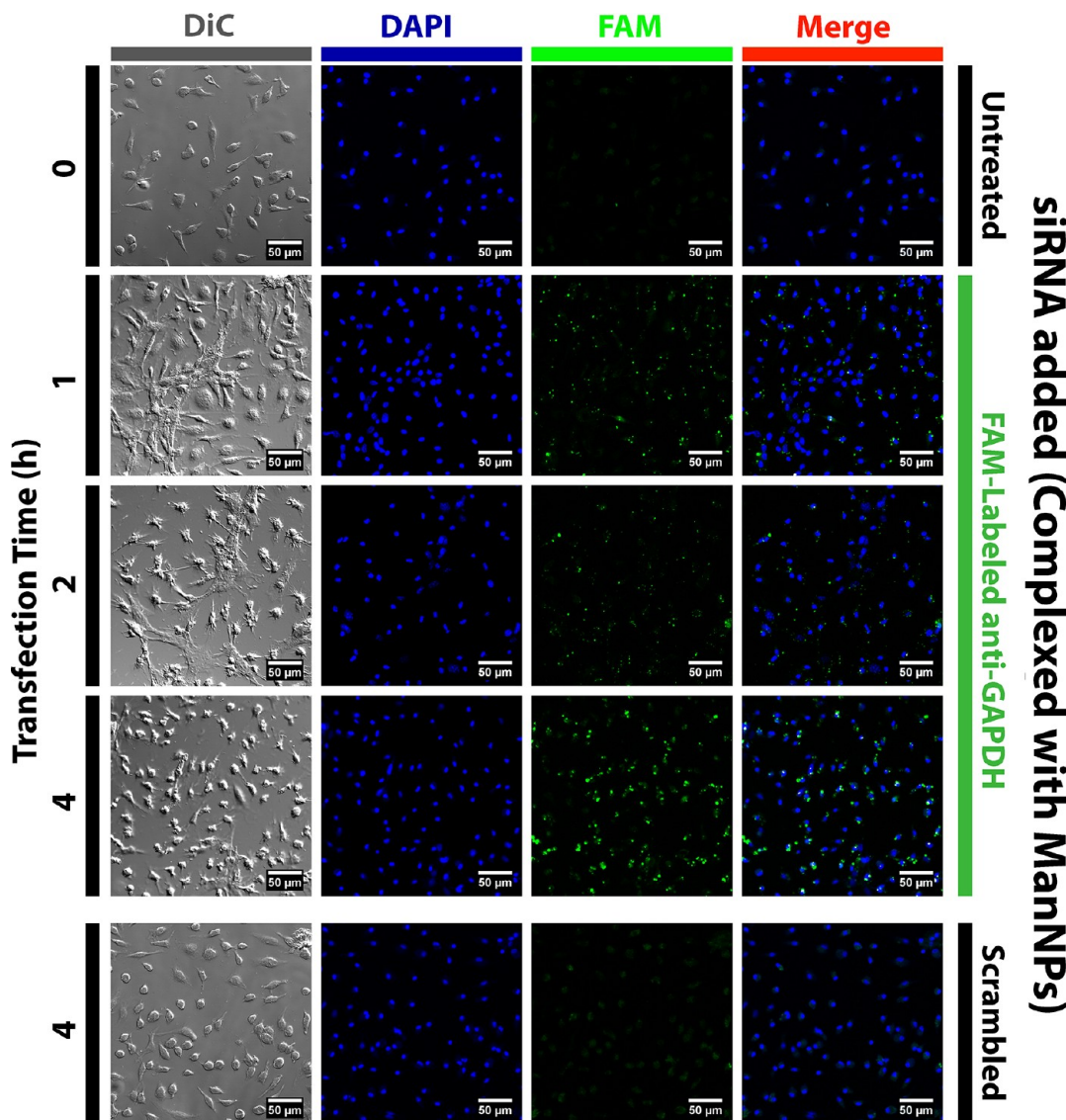


Figure 5. Kinetics of ManNP-mediated delivery of siRNA into primary macrophages. BMDMs were transfected with FAM-siRNA (green; complexed into ManNPs) for 1–4 h prior to being fixed, stained with DAPI (blue), and imaged via confocal microscopy. Scale bars are 50 μ m. As a comparison, BMDMs treated with nonfluorescent, scrambled siRNA (also complexed into ManNPs) are also shown. The brightness and contrast were enhanced in the DAPI channel to account for small differences in staining between samples. All settings were identical for FAM imaging. The punctate green signal is observed within 1–2 h of administration, suggesting internalization of siRNA into vesicles. At the 4 h time point, more green fluorescence has accumulated and the staining pattern is more diffuse, consistent with endosomal escape of the siRNA into the cytosol.

able to facilitate pH-dependent disruption of endosomal membranes and cytosolic delivery of the cargo.

To further demonstrate that the polymers do not cause significant cytotoxicity under physiologic pH conditions, immortalized human THP-1 macrophages were incubated with siRNA-loaded ManNPs at various N:P ratios, and cell viability was assessed via calcein AM/ethidium homodimer incorporation 4 or 24 h after ManNP delivery. Experimental groups were quantified via flow cytometry relative to untreated cells (100%) or methanol-killed cells [set to 0% (Figure 3A)]. For all N:P ratios investigated, negligible cytotoxicity was observed after treatment for 4 h. However, at 24 h, $76 \pm 1\%$ of the cells treated at the 8:1 N:P ratio remained viable, indicating that prolonged treatment of BMDMs with ManNPs and siRNA at this charge ratio resulted in mild but significant levels of cytotoxicity (*, ** $p < 0.01$; $n = 3$). The 4:1 N:P ratio was

selected for further experiments on the basis of precedent^{20,27,37} and because it did not result in significant cytotoxicity at 24 h.

ManNPs Selectively Enhance Delivery to Human Macrophages. To examine the potential of using the ManNPs to selectively target TAMs, we incubated ManNPs loaded with FAM-siRNA with immortalized human macrophages (THP-1) or human breast cancer cell lines (MDA-MB-231 and MDA-MB-468) for up to 4 h. Cellular internalization of the siRNA was assessed via flow cytometry (Figure 3B,C). All measurements were normalized against the inherent FAM intensity measured in untreated cells. As controls, cells treated with siRNA-loaded micelles made with the diblock copolymers were also measured. For both breast cancer cell lines, modest intracellular delivery of FAM-siRNA/ManNPs was observed with either carrier investigated (diblocks or ManNPs). Both cell types experienced an approximately 2-fold increase in FAM mean fluorescence intensity (MFI) over the 4 h study period.

With the macrophages, the same treatment period led to a 26-fold increase in the FAM MFI of the cells, confirming that these cells preferentially internalize the constructs relative to the model cancer cell lines (Figure 3C; $*p < 0.01$ vs all other treatment groups at the 4 h time point). Further, ManNPs facilitated a 3-fold increase in the level of delivery of siRNA to the macrophages, relative to the diblock micelles.

ManNPs Mediate CD206-Dependent Intracellular siRNA Delivery and Target Gene Knockdown in Primary Murine Macrophages. siRNA delivery and gene knockdown were examined in primary murine bone marrow-derived macrophages (BMDMs). Within 4 h of siRNA administration, ManNPs improved delivery of FAM-siRNA into macrophages by more than 40-fold relative to the delivery of free siRNA or 4-fold relative to the delivery of untargeted, diblock copolymers (Figure 4 and Figure S6 of the Supporting Information; $p < 0.01$). Notably, the uptake of ManNPs can be partially blocked via co-administration with D-mannose, indicating that internalization of the ManNPs is mediated by mannose receptor CD206. These phenomena are also observed when transfections are performed in serum-containing media (Figure 4A, right).

In support of these observations, imaging of the uptake of fluorescently labeled siRNA into BMDMs was accomplished by confocal microscopy (Figures 4A and 5 and Figure S7 of the Supporting Information). Consistent with the flow cytometry results, mannose targeting significantly increased the rate of delivery of siRNA into macrophages, and co-administration of D-mannose with the ManNPs reduced the magnitude of the FAM-siRNA signal in the BMDMs. Significant levels of FAM-siRNA can be visualized in the BMDMs within 1–2 h of administration.

The enhanced delivery of siRNA via the ManNPs also corresponded to knockdown of expression of a model gene, cyclophilin B (PPIB) in BMDMs relative to nontransfected cells and cells treated with complexes of ManNPs with scrambled siRNA [ManNPs/SCR (Figure 6; $*p < 0.05$)]. The commercially available Lipofectamine RNAiMAX transfection reagent was a reliable positive control and was the most effective vehicle for facilitating the knockdown of PPIB expression ($0.5 \pm 0.2\%$ residual PPIB expression). Despite lower levels of delivery of siRNA into the BMDMs than into ManNPs (Figure 4), the diblock nanoparticles also facilitated a significant level of PPIB knockdown ($p = 0.55$ relative to ManNPs, via one-way ANOVA).

DISCUSSION

Because of their central role in promoting the progression of a number of debilitating diseases, such as cancer and atherosclerosis, macrophages represent an important target for immunotherapy.^{19,38} Nanoparticle-mediated drug delivery is an attractive way to achieve this goal, because macrophages are phagocytes capable of efficiently internalizing particulate substances.^{39,40} However, macrophages play functional roles in maintaining the healthy physiology of many tissues, including bone, liver, and spleen.^{41–43} Therefore, to reduce the likelihood of an off-target impact on healthy immune function, it is very important to specifically target macrophages at desired pathological sites. In this work, we demonstrated the design, synthesis, and characterization of mannosylated micellar nanoparticles to target CD206 expression, which is upregulated in tumor-associated macrophages.^{23,24,44,45} The creation of these nanoparticles centers around a generalizable platform that

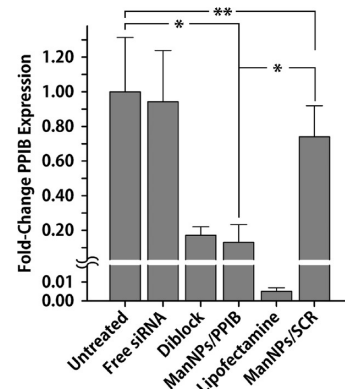


Figure 6. ManNPs mediate knockdown of PPIB expression in BMDMs. siRNA-mediated knockdown of PPIB expression using different transfection vehicles relative to controls. qRT-PCR confirmed ManNPs carrying anti-PPIB siRNA (ManNPs/PPIB) mediated an $87 \pm 10\%$ decrease in the level of target gene expression following treatment for 24 h, relative to nontransfected cells. Data were normalized to the expression of the housekeeping gene GAPDH as an internal control. Error bars represent the standard deviation of three independent experiments ($*p < 0.05$ by one-way ANOVA; **not statistically significant). Some BMDMs were also transfected with ManNPs carrying scrambled siRNA (ManNPs/SCR) as an additional negative control.

can be utilized for “clicking” ligands onto the surfaces of siRNA-condensing, polymeric nanoparticles. We opted for this strategy, involving the highly efficient Huisgen 1,3-dipolar cycloaddition reaction, otherwise known as azide–alkyne click chemistry (Figure 1), because it provides the necessary orthogonal chemistry to allow the synthesis of the block copolymers for siRNA delivery, followed by site-selective functionalization of the nanocarrier coronas with the ligand of interest in the final step. The resulting ManNPs exhibited diameters of <40 nm (Figure 2), a size range that confers the additional advantage of exhibiting improved passive accumulation into tumors.^{39,46}

This approach extends previous work by Convertine et al. describing polymers for siRNA delivery applications, which exhibited nonselective transfection activity driven by their cationic corona.²⁰ The diblock copolymers tested in this work were patterned after these polymers and provide a reliable benchmark against which the ManNPs can be reasonably compared.^{20,47} To improve the cellular specificity of these carriers, variants that target folate receptor and CD22 have recently been developed.^{32,33} These polymers include a micelle core-forming terpolymer block, which confers pH responsiveness to the final polymers. Because of the pK_a values of these monomers (7.5 for DMAEMA and 6.7 for PAA),^{48,49} at pH 7.4, approximately 50% of the amine groups on DMAEMA are protonated (NH^+), and 50% of the carboxylic groups on PAA are deprotonated (COO^-). Therefore, the terpolymer is approximately charge neutral at pH 7.4 when DMAEMA cations and PAA anions are present in relatively balanced quantities, leading to the insolubility of the terpolymer in water at this pH. When the terpolymer is paired with a hydrophilic block to form an amphiphilic diblock structure, the terpolymer block’s electrostatic and hydrophobic interactions allow it to self-assemble into a micelle core at pH 7.4.^{20,27,47} With a decrease in pH, PAA and DMAEMA become increasingly protonated, leading to a net cationic charge on this block that triggers micelle disassembly.²⁰ The exposed terpolymer is

hypothesized to disrupt endosomal and lysosomal membranes and ferry siRNA into the cytoplasm. The block copolymers described here behave in a fashion consistent with this hypothesis, as they exhibit pH-dependent hemolysis at pH ranges that mimic the acidic environments of late endosomes (Figure 2G).

These polymeric siRNA nanocarriers have cationic ζ -potential because of the presence of the poly(DMAEMA) block (blue in Figure 1), and previous observations by others suggest that such agents can exhibit charge-dependent cytotoxicity.¹⁴ Consistent with these reports, a moderate level of cytotoxicity at N:P ratios of >4:1 was not surprising. As a result, all polyplexes for subsequent experiments were prepared at N:P ratios for which negligible cytotoxicity was observed at the 24 h treatment time (Figure 3A). Because of negligible cytotoxicity at a 4:1 N:P ratio, many test agents have been optimized and evaluated at this charge ratio.^{20,27,37} When our delivery system is optimally formulated with siRNA, it is anticipated that the system for preferential macrophage targeting can be safely leveraged to treat diseases, such as cancer, where infiltrating macrophages at pathologic sites exhibit upregulated CD206 expression.⁵⁰

The ManNPs show cell selectivity, and the data suggest that in a tumor environment where cancer cells coexist with a significantly smaller population of macrophages, the ManNPs will enter macrophages markedly faster than the cancer cells (Figure 3B,C). While this increased internalization rate in macrophages over cancer cells was also observed for the diblock copolymer micelles, the effect was enhanced for the mannosylated constructs.

The ManNPs also facilitated improved delivery of siRNA into primary murine macrophages and generated robust knockdown of a model gene (Figures 4–6). The untargeted, diblock polymers also achieved potent gene knockdown despite delivering significantly smaller amounts of siRNA into the macrophages. However, like the ManNPs, the diblock polymers are capable of efficiently escaping from the endosomal compartment in a pH-dependent manner, as modeled via the hemolysis assay (Figure 2G).²⁹ Therefore, even if the diblock copolymers are not as efficiently internalized into BMDMs as the ManNPs, the diblock copolymers still deliver sufficient siRNA to cause significant levels of gene knockdown. This effect can depend on the potency of the siRNA sequence itself, as different siRNA sequences against the same target gene can exhibit widely different abilities to recognize the targeted mRNA sequence for knockdown.⁵¹

These results are significant because primary macrophages possess highly degradative phagocytic, endosomal, and lysosomal compartments, providing a formidable barrier to the cytosolic delivery of siRNA.¹³ Moreover, because the ManNPs are internalized via an endocytotic receptor, these data indicate that ManNPs successfully mediate escape from the endosomal pathway, through a mechanism that is likely mediated by the pH-responsive, endosomolytic behavior of the core-forming terpolymer block.²⁰

CONCLUSIONS

This report demonstrates a novel nanocarrier design for selectively targeting CD206-positive macrophages. The ManNPs' hydrodynamic radius was ~20 nm by DLS, which is appropriate for in vivo tumor biodistribution through the enhanced permeation and retention effect. This novel carrier has finely tuned pH-dependent membrane disruptive behavior,

to overcome the macrophage's highly degradative phagosomal and endosomal compartments. Nanocarrier characteristics allow biologics to be delivered into the macrophage cytosol and promote access of the payload to intracellular drug targets. Importantly, this generalized azide-containing siRNA delivery platform also has potential for click functionalization with alternative targeting ligands, and this is, to the best of our knowledge, the first demonstration of a "clickable", pH-responsive, endosomolytic micelle for siRNA delivery. These strategies will potentially open up new areas in cancer immunotherapy, allowing selective intervention with siRNA therapeutics.

ASSOCIATED CONTENT

Supporting Information

Supplementary materials and methods and supplementary figures. This material is available free of charge via the Internet at <http://pubs.acs.org>.

AUTHOR INFORMATION

Corresponding Author

*Department of Biomedical Engineering, Vanderbilt University, 5824 Stevenson Center, Nashville, TN 37235. E-mail: todd.d.giorgio@vanderbilt.edu. Phone: (615) 322-3521. Fax: (615) 343-7919.

Author Contributions

S.S.Y. oversaw all materials design and synthesis, experimental design, and data collection, analysis, and interpretation, with extensive input from F.E.Y., C.L.D., and T.D.G. C.M.L. and C.A.S. collected, analyzed, and interpreted data. W.J.B. and H.M.O. designed and selected the biological models used in this study and assisted in biological experiments with S.S.Y. and C.M.L., under the oversight of F.E.Y. C.E.N. and H.L. helped design protocols for the synthesis and purification of polymeric products and contributed new reagents and analytic tools crucial to the experiments. S.S.Y. wrote the manuscript. All authors discussed the results and commented on the manuscript.

Notes

The authors declare no competing financial interest.

ACKNOWLEDGMENTS

This work is supported through a Concept Award through the Department of Defense CDMRP Breast Cancer Research Program (W81XWH-10-1-0684). Bone marrow-derived macrophages were supported through a multi-investigator, collaborative IDEA Award through the Department of Defense CDMRP Breast Cancer Research Program (W81XWH-11-1-0344 and W81XWH-11-1-0242). Polymer development was also supported in part through National Institutes of Health (NIH) Grant R21 EB012750. S.S.Y. gratefully acknowledges partial support from a 2012 Lai Sulin Scholarship from the Vanderbilt University. C.M.L. acknowledges partial support through a fellowship from the Vanderbilt Undergraduate Summer Research Program (VUSR). Portions of this work were performed at the Vanderbilt Institute of Nanoscale Science and Engineering, using facilities renovated under National Science Foundation Grant ARI-R2 DMR-0963361. Confocal microscopy was supported in part by National Cancer Institute Cancer Center Support Grant P30 CA068485, utilizing the Vanderbilt University Medical Center Cell Imaging Shared Resource. The Vanderbilt University Medical Center

Cell Imaging Shared Resource is also supported by NIH Grants DK020593, DK058404, DK059637, and EY08126. qRT-PCR was performed in the laboratory of Prof. David G. Harrison (Division of Clinical Pharmacology, Vanderbilt University Medical Center, Nashville, TN). The authors also acknowledge Ryan A. Ortega (Department of Biomedical Engineering, Vanderbilt University) for reading and editing the manuscript.

■ ABBREVIATIONS

AzEMA, 2-azidoethyl methacrylate; BMA, butyl methacrylate; BMDM, bone marrow-derived macrophage; CD206, macrophage mannose receptor; DLS, dynamic light scattering; DMAEMA, 2-dimethylaminoethyl methacrylate; FAM-siRNA, FAM-labeled anti-GAPDH siRNA; ManNPs, mannosylated triblock copolymer nanoparticles; MFI, mean fluorescence intensity; N:P ratio, charge ratio ($\text{NH}^+:\text{PO}_4^-$); PAA, 2-propylacrylic acid; PCR, polymerase chain reaction; PPIB, peptidyl-prolyl *cis-trans*-isomerase B (cyclophilin B); qRT-PCR, quantitative real-time PCR; RAFT, reverse addition-fragmentation chain transfer; TAM, tumor-associated macrophage; THP-1, immortalized human leukemic monocytes/macrophages.

■ REFERENCES

- Kindt, T. J.; Goldsby, R. A.; Osborne, B. A.; Kuby, J. *Kuby Immunology*, 6th ed.; W. H. Freeman: New York, 2007; p xxii, 574, A-31, G-12, AN-27, I-27.
- Lewis, C. E.; Pollard, J. W. Distinct role of macrophages in different tumor microenvironments. *Cancer Res.* **2006**, *66* (2), 605–612.
- Dirkx, A. E.; Oude Egbrink, M. G.; Wagstaff, J.; Griffioen, A. W. Monocyte/macrophage infiltration in tumors: Modulators of angiogenesis. *J. Leukocyte Biol.* **2006**, *80* (6), 1183–1196.
- Vasievich, E. A.; Huang, L. The Suppressive Tumor Microenvironment: A Challenge in Cancer Immunotherapy. *Mol. Pharmaceutics* **2011**, *8* (3), 635–641.
- Fire, A.; Xu, S.; Montgomery, M. K.; Kostas, S. A.; Driver, S. E.; Mello, C. C. Potent and specific genetic interference by double-stranded RNA in *Caenorhabditis elegans*. *Nature* **1998**, *391* (6669), 806–811.
- Mantovani, A.; Garlanda, C.; Locati, M. Macrophage Diversity and Polarization in Atherosclerosis: A Question of Balance. *Arterioscler., Thromb., Vasc. Biol.* **2009**, *29* (10), 1419–1423.
- Porta, C.; Rimoldi, M.; Raes, G.; Brys, L.; Ghezzi, P.; Di Liberto, D.; Dieli, F.; Ghisletti, S.; Natoli, G.; De Baetselier, P.; Mantovani, A.; Sica, A. Tolerance and M2 (alternative) macrophage polarization are related processes orchestrated by p50 nuclear factor κ B. *Proc. Natl. Acad. Sci. U.S.A.* **2009**, *106* (35), 14978–14983.
- Hagemann, T.; Lawrence, T.; McNeish, I.; Charles, K. A.; Kulbe, H.; Thompson, R. G.; Robinson, S. C.; Balkwill, F. R. “Re-educating” tumor-associated macrophages by targeting NF- κ B. *J. Exp. Med.* **2008**, *205* (6), 1261–1268.
- Sica, A.; Bronte, V. Altered macrophage differentiation and immune dysfunction in tumor development. *J. Clin. Invest.* **2007**, *117* (5), 1155–1166.
- Kortylewski, M.; Swiderski, P.; Herrmann, A.; Wang, L.; Kowolik, C.; Kujawski, M.; Lee, H.; Scuto, A.; Liu, Y.; Yang, C.; Deng, J.; Soifer, H. S.; Raubitschek, A.; Forman, S.; Rossi, J. J.; Pardoll, D. M.; Jove, R.; Yu, H. In vivo delivery of siRNA to immune cells by conjugation to a TLR9 agonist enhances antitumor immune responses. *Nat. Biotechnol.* **2009**, *27* (10), 925–932.
- Leuschner, F.; Dutta, P.; Gorbatov, R.; Novobrantseva, T. I.; Donahoe, J. S.; Courties, G.; Lee, K. M.; Kim, J. I.; Markmann, J. F.; Marinelli, B.; Panizzi, P.; Lee, W. W.; Iwamoto, Y.; Milstein, S.; Epstein-Barash, H.; Cantley, W.; Wong, J.; Cortez-Retamozo, V.; Newton, A.; Love, K.; Libby, P.; Pittet, M. J.; Swirski, F. K.; Koteliansky, V.; Langer, R.; Weissleder, R.; Anderson, D. G.; Nahrendorf, M. Therapeutic siRNA silencing in inflammatory monocytes in mice. *Nat. Biotechnol.* **2011**, *29* (11), 1005–1010.
- Aouadi, M.; Tesz, G. J.; Nicoloro, S. M.; Wang, M.; Chouinard, M.; Soto, E.; Ostroff, G. R.; Czech, M. P. Orally delivered siRNA targeting macrophage Map4k4 suppresses systemic inflammation. *Nature* **2009**, *458* (7242), 1180–1184.
- Stacey, K. J.; Ross, I. L.; Hume, D. A. Electroporation and DNA-dependent cell death in murine macrophages. *Immunol. Cell Biol.* **1993**, *71* (2), 75–85.
- Lv, H.; Zhang, S.; Wang, B.; Cui, S.; Yan, J. Toxicity of cationic lipids and cationic polymers in gene delivery. *J. Controlled Release* **2006**, *114* (1), 100–109.
- Watkins, S. K.; Egilmez, N. K.; Suttles, J.; Stout, R. D. IL-12 rapidly alters the functional profile of tumor-associated and tumor-infiltrating macrophages in vitro and in vivo. *J. Immunol.* **2007**, *178* (3), 1357–1362.
- Briley-Saebo, K. C.; Cho, Y. S.; Shaw, P. X.; Ryu, S. K.; Mani, V.; Dickson, S.; Izadmehr, E.; Green, S.; Fayad, Z. A.; Tsimikas, S. Targeted Iron Oxide Particles for In Vivo Magnetic Resonance Detection of Atherosclerotic Lesions With Antibodies Directed to Oxidation-Specific Epitopes. *J. Am. Coll. Cardiol.* **2011**, *57* (3), 337–347.
- Lipinski, M. J.; Amirbekian, V.; Frias, J. C.; Aguinaldo, J. G.; Mani, V.; Briley-Saebo, K. C.; Fuster, V.; Fallon, J. T.; Fisher, E. A.; Fayad, Z. A. MRI to detect atherosclerosis with gadolinium-containing immunomicelles targeting the macrophage scavenger receptor. *Magn. Reson. Med.* **2006**, *56* (3), 601–610.
- Cormode, D. P.; Skajaa, T.; van Schooneveld, M. M.; Koole, R.; Jarzyna, P.; Lobatto, M. E.; Calcagno, C.; Barazzza, A.; Gordon, R. E.; Zanzonico, P.; Fisher, E. A.; Fayad, Z. A.; Mulder, W. J. Nanocrystal core high-density lipoproteins: A multimodality contrast agent platform. *Nano Lett.* **2008**, *8* (11), 3715–3723.
- Yu, S. S.; Ortega, R. A.; Reagan, B. W.; McPherson, J. A.; Sung, H.-J.; Giorgio, T. D. Emerging applications of nanotechnology for the diagnosis and management of vulnerable atherosclerotic plaques. *Wiley Interdiscip. Rev.: Nanomed. Nanobiotechnol.* **2011**, *3* (6), 620–646.
- Convertine, A. J.; Benoit, D. S.; Duvall, C. L.; Hoffman, A. S.; Stayton, P. S. Development of a novel endosomolytic diblock copolymer for siRNA delivery. *J. Controlled Release* **2009**, *133* (3), 221–229.
- Boyer, C.; Bulmus, V.; Davis, T. P.; Ladmiral, V.; Liu, J.; Perrier, S. Bioapplications of RAFT polymerization. *Chem. Rev.* **2009**, *109* (11), 5402–5436.
- Kolb, H. C.; Sharpless, K. B. The growing impact of click chemistry on drug discovery. *Drug Discovery Today* **2003**, *8* (24), 1128–1137.
- Allavena, P.; Chieppa, M.; Bianchi, G.; Solinas, G.; Fabbri, M.; Laskarin, G.; Mantovani, A. Engagement of the Mannose Receptor by Tumoral Mucins Activates an Immune Suppressive Phenotype in Human Tumor-Associated Macrophages. *Clin. Dev. Immunol.* **2010**, *2010*.
- Taylor, P. R.; Gordon, S.; Martinez-Pomares, L. The mannose receptor: Linking homeostasis and immunity through sugar recognition. *Trends Immunol.* **2005**, *26* (2), 104–110.
- East, L.; Isacke, C. M. The mannose receptor family. *Biochim. Biophys. Acta* **2002**, *1572* (2–3), 364–386.
- Solinas, G.; Germano, G.; Mantovani, A.; Allavena, P. Tumor-associated macrophages (TAM) as major players of the cancer-related inflammation. *J. Leukocyte Biol.* **2009**, *86* (5), 1065–1073.
- Nelson, C. E.; Gupta, M. K.; Adolph, E. J.; Shannon, J. M.; Guelcher, S. A.; Duvall, C. L. Sustained local delivery of siRNA from an injectable scaffold. *Biomaterials* **2012**, *33* (4), 1154–1161.
- Kirkland-York, S.; Zhang, Y.; Smith, A. E.; York, A. W.; Huang, F.; McCormick, C. L. Tailored design of Au nanoparticle-siRNA carriers utilizing reversible addition-fragmentation chain transfer polymers. *Biomacromolecules* **2010**, *11* (4), 1052–1059.
- Evans, B. C.; Nelson, C. E.; Yu, S. S.; Kim, A. J.; Li, H.; Nelson, H. M.; Giorgio, T. D.; Duvall, C. L. Ex Vivo Red Blood Cell Hemolysis

Assay for the Evaluation of pH-responsive Endosomolytic Agents for Cytosolic Delivery of Biomacromolecular Drugs. *J. Visualized Exp.* **2013**, DOI: 10.3791/50166.

(30) Connelly, L.; Jacobs, A. T.; Palacios-Callender, M.; Moncada, S.; Hobbs, A. J. Macrophage endothelial nitric-oxide synthase autoregulates cellular activation and pro-inflammatory protein expression. *J. Biol. Chem.* **2003**, 278 (29), 26480–26487.

(31) Duvall, C. L.; Convertine, A. J.; Benoit, D. S.; Hoffman, A. S.; Stayton, P. S. Intracellular Delivery of a Proapoptotic Peptide via Conjugation to a RAFT Synthesized Endosomolytic Polymer. *Mol. Pharmaceutics* **2010**, 7 (2), 468–476.

(32) Benoit, D. S. W.; Srinivasan, S.; Shubin, A. D.; Stayton, P. S. Synthesis of Folate-Functionalized RAFT Polymers for Targeted siRNA Delivery. *Biomacromolecules* **2011**, 12 (7), 2708–2714.

(33) Palanca-Wessels, M. C.; Convertine, A. J.; Cutler-Strom, R.; Booth, G. C.; Lee, F.; Berguig, G. Y.; Stayton, P. S.; Press, O. W. Anti-CD22 antibody targeting of pH-responsive micelles enhances small interfering RNA delivery and gene silencing in lymphoma cells. *Mol. Ther.* **2011**, 19 (8), 1529–1537.

(34) Crownover, E.; Duvall, C. L.; Convertine, A.; Hoffman, A. S.; Stayton, P. S. RAFT-synthesized graft copolymers that enhance pH-dependent membrane destabilization and protein circulation times. *J. Controlled Release* **2011**, 155 (2), 167–174.

(35) Sumerlin, B. S.; Tsarevsky, N. V.; Louche, G.; Lee, R. Y.; Matyjaszewski, K. Highly Efficient “Click” Functionalization of Poly(3-azidopropyl methacrylate) Prepared by ATRP. *Macromolecules* **2005**, 38 (18), 7540–7545.

(36) Plotz, P. H.; Rifai, A. Stable, Soluble, Model Immune-Complexes Made with a Versatile Multivalent Affinity-Labeling Antigen. *Biochemistry* **1982**, 21 (2), 301–308.

(37) Benoit, D. S. W.; Henry, S. M.; Shubin, A. D.; Hoffman, A. S.; Stayton, P. S. pH-Responsive Polymeric siRNA Carriers Sensitize Multidrug Resistant Ovarian Cancer Cells to Doxorubicin via Knockdown of Polo-like Kinase 1. *Mol. Pharmaceutics* **2010**, 7 (2), 442–455.

(38) Pollard, J. W. Macrophages define the invasive microenvironment in breast cancer. *J. Leukocyte Biol.* **2008**, 84 (3), 623–630.

(39) Yu, S. S.; Lau, C. M.; Thomas, S. N.; Jerome, W. G.; Maron, D. J.; Dickerson, J. H.; Hubbell, J. A.; Giorgio, T. D. Size- and charge-dependent non-specific uptake of PEGylated nanoparticles by macrophages. *Int. J. Nanomed.* **2012**, 7, 799–813.

(40) Daldrup-Link, H. E.; Golovko, D.; Ruffel, B.; DeNardo, D.; Castaneda, R.; Ansari, C.; Rao, J.; Tikhomirov, G. A.; Wendland, M. F.; Corot, C.; Coussens, L. M. MR Imaging of Tumor Associated Macrophages with Clinically-Applicable Iron Oxide Nanoparticles. *Clin. Cancer Res.* **2011**, 17, 5695–5704.

(41) Martin, P. Wound Healing: Aiming for Perfect Skin Regeneration. *Science* **1997**, 276 (5309), 75–81.

(42) Bouwens, L.; Baekeland, M.; de Zanger, R.; Wisse, E. Quantitation, tissue distribution and proliferation kinetics of Kupffer cells in normal rat liver. *Hepatology* **1986**, 6 (4), 718–722.

(43) Felix, R.; Cecchini, M. G.; Hofstetter, W.; Elford, P. R.; Stutzer, A.; Fleisch, H. Rapid publication: Impairment of macrophage colony-stimulating factor production and lack of resident bone marrow macrophages in the osteopetrotic op/op Mouse. *J. Bone Miner. Res.* **1990**, 5 (7), 781–789.

(44) Linehan, S. A.; Martinez-Pomares, L.; Gordon, S. Mannose receptor and scavenger receptor: Two macrophage pattern recognition receptors with diverse functions in tissue homeostasis and host defense. *Adv. Exp. Med. Biol.* **2000**, 479, 1–14.

(45) Stahl, P. D.; Ezekowitz, R. A. B. The mannose receptor is a pattern recognition receptor involved in host defense. *Curr. Opin. Immunol.* **1998**, 10 (1), 50–55.

(46) Larsen, E. K.; Nielsen, T.; Wittenborn, T.; Birkedal, H.; Vorup-Jensen, T.; Jakobsen, M. H.; Ostergaard, L.; Horsman, M. R.; Besenbacher, F.; Howard, K. A.; Kjems, J. Size-Dependent Accumulation of PEGylated Silane-Coated Magnetic Iron Oxide Nanoparticles in Murine Tumors. *ACS Nano* **2009**, 3, 1947–1951.

(47) Convertine, A. J.; Diab, C.; Prieve, M.; Paschal, A.; Hoffman, A. S.; Johnson, P. H.; Stayton, P. S. pH-Responsive Polymeric Micelle Carriers for siRNA Drugs. *Biomacromolecules* **2010**, 11 (11), 2904–2911.

(48) van de Wetering, P.; Moret, E. E.; Schuurmans-Nieuwenbroek, N. M.; van Steenbergen, M. J.; Hennink, W. E. Structure-activity relationships of water-soluble cationic methacrylate/methacrylamide polymers for nonviral gene delivery. *Bioconjugate Chem.* **1999**, 10 (4), 589–597.

(49) Grainger, S. J.; El-Sayed, M. E. H. Stimuli-Sensitive Particles for Drug Delivery. In *Biologically-Responsive Hybrid Biomaterials*; Jabbari, E., Khademhosseini, A., Eds.; World Scientific: Singapore, 2010; pp 171–190.

(50) Luo, Y.; Zhou, H.; Krueger, J.; Kaplan, C.; Lee, S.-H.; Dolman, C.; Markowitz, D.; Wu, W.; Liu, C.; Reisfeld, R. A.; Xiang, R. Targeting tumor-associated macrophages as a novel strategy against breast cancer. *J. Clin. Invest.* **2006**, 116 (8), 2132–2141.

(51) Rettig, G. R.; Behlke, M. A. Progress toward in vivo use of siRNAs-II. *Mol. Ther.* **2012**, 20 (3), 483–512.

Tumor Microenvironment Complexity: Emerging Roles in Cancer Therapy

Melody A. Swartz¹, Noriho Iida², Edward W. Roberts³, Sabina Sangaletti⁴, Melissa H. Wong⁵, Fiona E. Yull⁶, Lisa M. Coussens⁵, and Yves A. DeClerck⁷

Abstract

The tumor microenvironment (TME) consists of cells, soluble factors, signaling molecules, extracellular matrix, and mechanical cues that can promote neoplastic transformation, support tumor growth and invasion, protect the tumor from host immunity, foster therapeutic resistance, and provide niches for dormant metastases to thrive. An *American Association for Cancer Research (AACR)* special conference held on November 3–6, 2011, addressed five emerging concepts in our understanding of the TME: its dynamic evolution, how it is educated by tumor cells, pathways of communication between stromal and tumor cells, immunomodulatory roles of the lymphatic system, and contribution of the intestinal microbiota. These discussions raised critical questions on how to include the analysis of the TME in personalized cancer diagnosis and treatment. *Cancer Res*; 72(10): 2473–80. ©2012 AACR.

Introduction

The tumor microenvironment (TME) has received growing attention from an increasing number of investigators in the United States and abroad (1) and also by research organizations including the National Cancer Institute (NCI) and the *American Association for Cancer Research (AACR)* over the last decade. As our understanding of the role of the TME in cancer continues to evolve, the complexity of the interactions between neoplastic tumor cells and their microenvironment has become increasingly apparent, and at the same time, the number of agents entering clinical trials that specifically target interactive pathways between neoplastic and stromal cells has increased. On November 3–6, 2011, the AACR, in conjunction with its Tumor Microenvironment Working Group, organized a special conference entitled "Tumor Microenvironment Complexity: Emerging Roles in Cancer Therapy" that brought together in Orlando, FL, more than 280 participants including 42 speakers to discuss recent progress made in the field and to identify future directions of the highest priority. A workshop chaired by Suresh Mohla (NCI, Bethesda, MD) also presented the new TME network (TMEN) program at the NCI funded by U54 and U01 grants that brings together 11 centers and whose

mission is to promote and facilitate interdisciplinary collaborations in understanding the host stroma in tumorigenesis (2).

Many of the presentations focused on the interactions between tumor cells and their surrounding environment. How such interactions are critical for tumor progression was well illustrated by the work of Luis Parada (University of Texas Southwest Medical Center, Dallas, TX), who gave the opening keynote lecture. Using mouse models of neurofibromatosis type 1 (Nf1), he showed that loss of *Nf1* heterozygosity in Schwann cells that give rise to plexiform neurofibroma is insufficient for neurofibroma formation but rather that *Nf1* haploinsufficiency in mast cells is also required for tumor formation. Furthermore, cKIT in mast cells was critical for their recruitment and protumor effects. These elegant studies have led to clinical studies evaluating imatinib (Gleevec) in patients with Nf1 that have thus far indicated a favorable response rate and have bolstered enthusiasm for targeting stromal cells in a diversity of solid tumors.

The present article summarizes the meeting in 5 new emerging concepts (Fig. 1) and 2 critical questions that were the subject of discussion during the conference.

Emerging concept 1: The TME is a dynamic milieu

The TME is in constant evolution as a result of tissue remodeling, metabolic alterations in the tumor, and changes in the recruitment of stromal cells including a diversity of immune cells. Tissue remodeling that occurs in the post-partum breast during mammary gland involution, for example, perpetuates an increased risk of breast cancer (3). Pepper Schedin (University of Colorado, Aurora, CO) described how such remodeling creates a tumor-promoting inflammatory environment similar to the environment of a wound, characterized by an influx of T-helper (T_H)2-type macrophages, abundant fibrillar collagen, and increased COX-2 activity.

Authors' Affiliations: ¹Institute of Bioengineering and Swiss Institute for Experimental Cancer Research, École Polytechnique Fédérale de Lausanne, Lausanne, Switzerland; ²National Cancer Institute, National Institutes of Health, Bethesda, Maryland; ³University of Cambridge, Cambridge, United Kingdom; ⁴Fondazione IRCCS Instituto Nazionale Tumori, Milan, Italy; ⁵Oregon Health and Sciences University, Portland, Oregon; ⁶Vanderbilt University, Nashville, Tennessee; and ⁷University of Southern California, Los Angeles, California

Corresponding Author: Yves A. DeClerck, Children's Hospital Los Angeles, 4650 Sunset Boulevard, MS#54, Los Angeles, CA 90027. Phone: 323-361-2150; Fax: 323-361-4902; E-mail: declerck@usc.edu

doi: 10.1158/0008-5472.CAN-12-0122

©2012 American Association for Cancer Research.

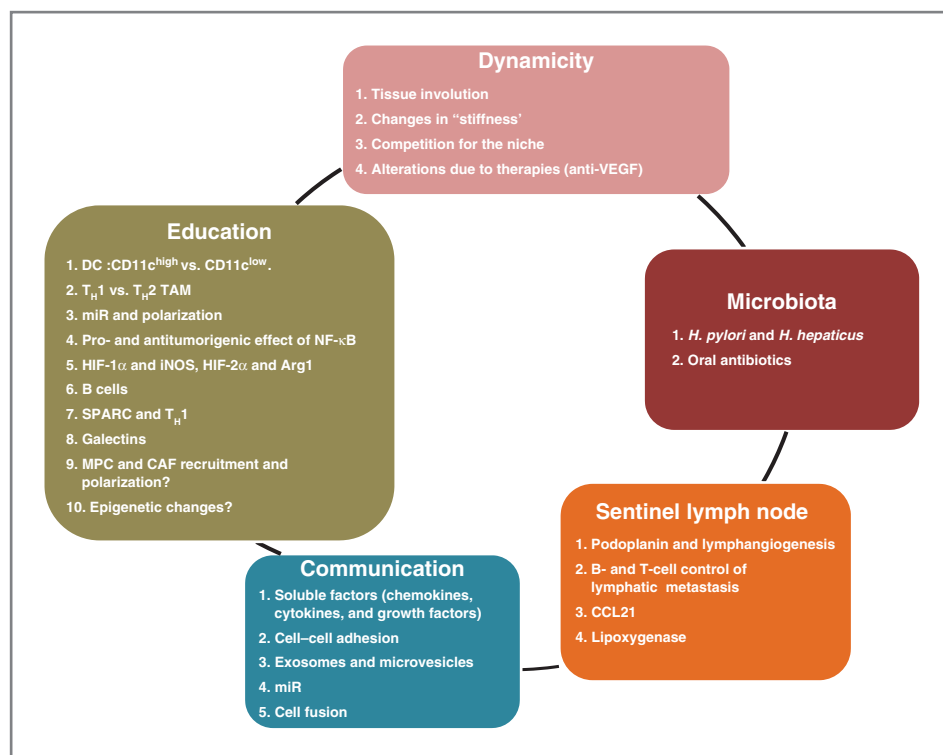


Figure 1. The diagram summarizes the 5 emerging themes that were the subject of presentations and discussions at the special AACR conference entitled "Tumor Microenvironment Complexity: Emerging Roles in Cancer Therapy" that took place in Orlando, FL, on November 3–6, 2011.

Human mammary tumor cells implanted into mouse mammary fat pads formed tumors more readily, with increased metastatic potential, when implanted in involuting (postlactation) mammary glands, rather than during pregnancy, whereas COX-2 inhibition during weaning slowed tumor growth and limited metastasis. These results raise the intriguing possibility that short-term anti-inflammatory treatment during the postpartum period may decrease breast cancer risk, similar to results in colon cancer (4).

Another important feature of the TME is the content and organization of the extracellular matrix (ECM), whose mechanical properties affect neoplastic cell differentiation and invasiveness. Increased stromal stiffness in breast tissue is a known risk factor of breast cancer in humans, and Valerie Weaver (University of California San Francisco, San Francisco, CA) described how inhibition of collagen cross-linking by lysyl oxidase (LOX) in murine models delayed and decreased tumor invasion (5). ECM stiffening promoted activation of ROCK, a Rho kinase effector, which increased collagen deposition by mechanisms associated with increased Wnt signaling, activation of STAT3, and expression of inflammatory cytokines, including CCL2 and granulocyte macrophage colony-stimulating factor (GM-CSF), that recruited bone marrow (BM)-derived cells into the TME. These compelling data indicate that changes in the biomechanical function of the TME impact neoplastic cell proliferation and migration, as well as secretion of immunomodulatory factors. Using second harmonic generation microscopy, Ryan Burke (University of Rochester, New York, NY) from the laboratory of Edward Brown showed that altering the alignment of collagen fibers in solid tumors impacted malignant cell invasion and their metastatic prop-

erties, in part, via regulation of TNF- α and macrophages. Thus, as similarly illustrated in P. Shedin's presentation in the involuting mammary gland not only the amount of stromal collagen but also its organization are drivers of the malignant process.

Dynamic interactions between tumor cells and cells of the osteoblastic niche affect malignant evolution. It has been appreciated for some time that in patients with prostate cancer, increased presence of circulating hematopoietic stem cells (HSC) is an indicator of bone metastasis. Russell Taichman (University of Michigan, Ann Arbor, MI) showed that prostate carcinomas seeded into BM remained dormant and insensitive to drug treatment (6). During bone metastasis, these cells competed with HSCs for occupation of the osteoblastic niche. Conversely, altering the osteoblastic niche in mice by pretreatment with parathormone or by clearing HSCs with a CXCR4 inhibitor promoted prostatic bone metastasis.

Anticancer therapies alter the TME in ways that either promote or inhibit tumorigenicity, depending on a diverse array of heterotypic mechanisms. This concept was elegantly illustrated for the case of anti-VEGF therapy by Gabriele Bergers (University of California San Francisco) who showed that glioblastoma-bearing mice treated with Avastin exhibited a transient beneficial therapeutic response that was followed by tumor revascularization and enhanced invasiveness (7) associated with increased c-Met expression and epithelial-to-mesenchymal transformation (EMT). This is explained by the observation that VEGF receptor (VEGFR)2 and c-Met were antagonistically associated, where c-Met signaling became dominant in the presence of VEGFR2 signaling blockade and vice versa. Thus, combined therapy targeting both signaling

pathways may be required for efficient, durable antitumor responses.

Emerging concept 2: Significance of immune and stromal cell education in the TME

Emerging studies indicate that reciprocal interactions between the diverse assemblages of stromal cells and evolving neoplastic cells fundamentally regulate tumor progression. Adaptive and innate immune cells represent a significant component of the TME. Largely dependent on soluble cytokines and chemokines, immune cells become variably polarized toward T_{H1} - (generally antitumor) or T_{H2} -type (generally protumorigenic) phenotypes. While initially described for $CD4^+$ T cells, it is now clear that T_{H1} - and T_{H2} -type factors regulate the phenotype and bioactivity of essentially all immune cells subtypes. Michael Shurin (University of Pittsburgh, Pittsburgh, PA) showed that conventional dendritic cells (DC) exposed to tumor-derived factors polarize into regulatory DCs (regDC) that suppressed the proliferation of preactivated T cells and were phenotypically and functionally different from their precursors and from immature conventional DCs (8). In particular, $CD11c^{low} CD11b^{high}$ DCs exhibited immunosuppressive activity toward implanted 3LL tumors, whereas $CD11c^{high}$ DCs instead promoted their metastasis dependent on RhoGTPase. In the presence of *Clostridium difficile* toxin, DCs failed to polarize and exhibited altered activity and effector functions. Related to DCs, the significance of macrophage T_{H2} polarization was reported by Lisa Coussens (Oregon Health and Science University, Portland, OR). T_{H2} -type tumor-associated macrophages (TAM) are common constituents of many solid tumor types and not only provide proangiogenic and proinvasive factors to growing tumors but also suppress $CD8^+$ T-cell-mediated antitumor immunity. Accordingly, blocking recruitment of macrophages into mammary tumors by treating mice with agents that blocked CSF1R signaling not only diminished tumor vascularity and slowed primary tumor development but also reduced formation of pulmonary metastases and improved survival, when given in combination with chemotherapy, by $CD8^+$ T-cell-dependent mechanisms (9). These preclinical data highlight the multifunctional role of macrophages in solid tumors and importantly reveal that TAMs blunt cell killing by $CD8^+$ T cells as well as by various forms of chemotherapy suggesting a novel combinatorial anticancer approach. A therapeutic CSF1R kinase inhibitor, PLX3397, is currently being tested with eribulin in a phase Ib/II clinical trial in patients with metastatic triple-negative breast cancer.

Macrophage polarization is also modulated by endogenous microRNAs (miR). Michele de Palma (San Raffaele Scientific Institute, Milan, Italy) presented data identifying miR-511-3p, an miRNA encoded by the mannose receptor *Mrc1* gene that was specifically upregulated in $F4/80^+ MRC1^+ CD11c^+$ TAMs and functioned as a negative regulator of TAM protumorigenic polarization. Also, critical for macrophage phenotype and bioactivity is the expression of the NF- κ B. Using mice in which expression of a constitutive activator of NF- κ B was induced, Fiona Yull (Vanderbilt University, Nashville, TN) reported that NF- κ B activation in macrophages variably affected carcinoma cell metastasis dependent on spatial/temporal features (10).

When activated in the presence of circulating tumor cells, NF- κ B exerted antitumorigenic activities whereas when activated later in tumor progression, for example, in secondary sites of metastasis, protumorigenic activities on macrophages predominated.

Hypoxia can also affect immune cell education in the TME depending on the type of hypoxia-inducible factor (HIF) involved in myeloid cells (11). Jessica Shay (University of Pennsylvania, Philadelphia, PA) of Celeste Simon's laboratory reported that whereas HIF-1 α fostered T_{H1} polarization, HIF-2 α instead favored T_{H2} polarization of immune cells. Experimentally, when HIF-2 α was either inhibited via acriflavine or genetically deleted, $CD68^+$ macrophage infiltration into colons of mice challenged with dextran sodium sulphate (DSS) was decreased, and carcinogenesis was reduced. Randall Johnson (University of California San Diego, La Jolla, CA) presented complementary data showing that HIF regulated inducible nitric oxide synthase (iNOS) and arginase 1 (Arg1) expression. In the presence of low IFN- γ , HIF-2 α induced the expression of Arg1, reducing the production of NO and fostering a T_{H2} phenotype. Under conditions of high IFN- γ , HIF-1 α dominated and iNOS was induced converting arginine into NO and promoting a T_{H1} phenotype.

Tumor recruitment of myelocytic cells is also regulated by B cells. Using a mouse model of squamous cell carcinoma induced by K-Ras expression in basal keratinocytes, Andrew Gunderson (Pennsylvania State University, University Park, PA) of Adam Glick's laboratory reported that K-Ras activation led to cutaneous inflammation, including expansion of immunosuppressive myeloid cells. However, when B cells were deleted, myeloid suppressor cells were ablated, indicating the requirement of B cells to stimulate the recruitment and suppressive activity of these myeloid cells. Along these same lines, Tiziana Schioppa (Barts Cancer Institute, London, United Kingdom) from Frances Balkwill's laboratory presented data showing that the clinical efficacy of anti-TNF- α therapy may, in part, be due to its effect on protumorigenic B cells (12). Development of 7,12-dimethylbenz(a)anthracene (DMBA)/12-O-tetradecanoylphorbol-13-acetate (TPA)-induced papillomas was significantly reduced in either TNF- α -deficient or B-cell-deficient mice; transfer of B cells from DMBA-treated mice into TNF- α -/- recipient mice reinstated papilloma development. Notably, B regulatory cell expression of interleukin (IL)-10 was critically dependent on TNF- α expression, suggesting that anti-TNF- α therapy promotes antitumor immunity by suppressing B regulatory expression of IL-10.

ECM proteins also contribute to local immunoregulation. Sabina Sangaletti (Fondazione IRCCS Instituto Nazionale Tumori, Milan, Italy) from the laboratory of Mario Colombo showed that the matricellular secreted protein acidic rich in cysteine (SPARC) with profibrotic actions was expressed in remodeling tissues and in tumors and promoted T_{H1} -type polarization by regulating expression and activation of TGF- β 1 and in turn modulating macrophage production of TNF- α (13). In the absence of SPARC, macrophages did not down-modulate TNF- α in response to TGF- β 1, and thus fostered fibrosis. SPARC could thus be a potential therapeutic target to render the TME unsuitable for cancer cell proliferation.

Galectins, a family of evolutionarily conserved glycan-binding proteins, play an important function in educating immune cells and controlling angiogenesis. Gabriel Rabinovich (Instituto de Biología y Medicina Experimental, Buenos Aires, Argentina) discussed how galectin-1 associated with VEGFR2 in tumor-associated endothelial cell stimulated VEGFR2-mediated signaling and angiogenesis in the absence of VEGF (14). Accordingly, a monoclonal antibody (mAb) against galectin-1 inhibited growth of Kaposi sarcoma and B16 melanomas in mice with increased recruitment of T_{H17} -type lymphocytes and decreased tumor vascularization.

In addition to polarization, programmed death-1 (PD-1), an inhibitory coreceptor expressed on T and B cells, plays an important role in providing immune-inhibitory signals in the TME. Drew Pardoll (Johns Hopkins University, Baltimore, MD) showed that PD-1 was expressed by activated T and B cells and monocytes and interacted with the ligand B7-H1 expressed by DCs and many tumor cells, providing them with adaptive resistance and an immune escape mechanism. Accordingly, a therapeutic mAb against B7H1 is currently being tested in a phase I clinical trial in patients with advanced solid tumors and preliminary data suggest clinical activity against melanoma and non-small cell lung cancer (15).

Nonimmune mesenchymal cells, such as fibroblasts, myofibroblasts, or adipocytes, play an important role in TMEs where they are "educated" by neoplastic cells. Frank Marini (Wake Forest Comprehensive Cancer Center, Winston-Salem, NC) used mice transplanted with EGFP-labeled BM cells to show that BM-derived mesenchymal progenitor cells (MPC) were recruited into primary tumors where they differentiated into cancer-associated fibroblasts (CAF), expressing fibroblast activation protein (FAP) and fibroblast-specific protein (FSP). The presence of these cells in the tumor affected growth and promoted immune escape. Deletion of CD44 led to a loss of FAP/FSP-producing cells in the tumor, suggesting that CD44 was critical for their recruitment. When in the TME, MPCs and CAFs interact with tumor cells by a variety of mechanisms. One mechanism is activation of the hedgehog (HH) pathway. Yunjung Choi (University of Michigan, Ann Arbor, MI) of Ronald Buckanovich's laboratory showed that HH activation in tumoral stem cells led to induction of bone morphogenic protein (BMP)-2 and -4 (among other factors) that stimulate proliferation of $ALDH^+$ ovarian cancer stem cells. MPCs and CAFs are a source of multiple growth factors and chemokines/cytokines including IL-6 and FAP. Yves DeClerck (University of Southern California, Los Angeles, CA) reported that IL-6 expression in MPCs was increased in the presence of tumor (neuroblastoma) cells and that it activated STAT3, which by upregulating expression of survivin, Mcl-1, and Bcl-xL in neoplastic cells, increased their resistance to cytotoxic drugs. Interestingly, TAMs collaborated with MPCs by being a source of the agonistic soluble IL-6 receptor enhancing STAT3 activation. Targeting CAFs may be an attractive therapeutic target; however, it may have a toxic effect as these cells are present in normal tissue. Ed Roberts (University of Cambridge, Cambridge, United Kingdom) from Douglas Fearon's group provided data showing that FAP^+ cells were present in normal tissues and that their depletion in nontumor-bearing mice

induced a state of cachexia and metabolic waste with a loss in skeletal muscle of follistatin, an inhibitor of procatabolic mediators. Using intravital microscopy and 3-dimensional cell-based models, Eric Sahai (London Research Institute, London, United Kingdom) showed that CAFs contributed to tumor cell migration by locally remodeling the ECM to generate routes used by "following" carcinoma cells (16). ECM remodeling by CAFs depended on Rho-Rock signaling that occurred under the influence of neoplastic cells via IL-6 that induced actomyosin polymerization in CAFs by STAT3 activation (17).

Genetic factors can also contribute to education of the stroma in cancer. Germ line mutations that affect formation of carcinomas such as in the case of familial adenomatous polyposis coli (FAPC) affect mesenchymal cells in the TME. For example, Monica Bertagnolli (Harvard Medical College, Boston, MA) presented data showing that in *Apc*^{Min/+} mice, Wnt signaling was also deregulated in mesenchymal cells and desmoid tumors formed as the result of a COX-2-dependent activation of the mesenchyme associated with an increased production of collagens (18). Furthermore, epigenetic factors may contribute. Benjamin Tycko (Columbia University, New York, NY) showed that in pancreatic intraepithelial neoplasia, there was a decrease in global methylation not only in malignant epithelial cells but also in CAFs. DNA methylation further decreased as lesions progressed from *in situ* to invasive carcinoma. Interestingly, in transgenic mice prone to develop pancreatic cancers, treatment with the hypomethylating agent 5-azacytidine led to a hypomethylation crisis associated with reduction in tumor growth and upregulation of a subset of IFN target genes affecting cell proliferation.

Emerging concept 3: The mechanisms of communication between tumor cells and the microenvironment are diverse: emerging role of exosomes and cell fusion

Two novel mechanisms potentially supporting the communication between tumor cells and stromal cells were the subject of presentations at the meeting. A first mechanism consisted of exosomes (19). Initially considered to be primarily responsible for release of unwanted material by cells, exosomes are now recognized as active entities involved in regulating a variety of extracellular signals. Exosomes have been isolated from the plasma of patients with cancer, and their concentration and protein content correlated with tumor stage and clinical outcome. David Lyden (Cornell University Weill Medical College, New York, NY) presented data suggesting that tumor exosomes, which package not only tumor antigens and immunosuppressive molecules but also miRs, were involved in mobilizing BM-derived cells to premetastatic niches (20). Preconditioning of BM cells with exosomes purified from metastatic melanoma cells, but not from non-malignant cells, transplanted into lethally irradiated recipient mice significantly increased metastasis. Tumor cells within the TME are not the sole source of exosomes, and Ngai-Na Chloe Co (University of Texas MD Anderson Cancer Center, Houston, TX) from Samuel Mok's laboratory presented work showing that CAFs and cancer-associated adipocytes from ovarian tumors released miR21 containing exosomes that in co-culture,

transferred miR21 to tumor cells promoting migration and invasion. Exosomes thus appear to be involved in a 2-way communication between tumor cells and stromal cells. A second newly reported mechanism of communication between tumor and stromal cells is cell fusion. Melissa Wong (Oregon Health and Science University) presented *in vitro* and *in vivo* data showing that functional fusion between TAMs and neoplastic cells occurred and altered the transcriptome by introducing the expression of macrophage-specific genes (21). These macrophage–carcinoma cell fusion hybrid cells may be more prone to migrate and metastasize due to their ability to mimic migratory behaviors of macrophages.

Emerging concept 4: The sentinel lymph node is an active part of the TME

Many tumors metastasize first to the sentinel lymph node after entering lymphatic vessels around the tumor. Although tumor-associated lymphatic vessels were previously considered passive transporters of fluid, molecules, and cells, the last decade has seen numerous reports correlating lymphatic growth factors in the TME with metastatic potential (22). Furthermore, observations that sentinel lymph nodes undergo lymphangiogenesis before metastasis led to the notion that lymph node lymphangiogenesis may be involved in the pre-metastatic niche. Five presentations illustrated how tumor-associated lymphatic vessels, lymph flow, and the sentinel lymph nodes promote immune tolerance and distant metastasis.

Michael Detmar (ETC Zurich Institute of Pharmaceutical Sciences, Zurich, Switzerland) discussed how podoplanin, expressed by lymph node stromal cells in the T-cell zone, can be present in the tumor stroma and how its presence correlated with tumor lymphangiogenesis (23). One mechanism by which podoplanin-induced lymphangiogenesis occurred is via endothelin-1 upregulation. *In vitro*, podoplanin increased tumor cell motility as well as lymphatic endothelial cell (LEC) migration and tubulogenesis. Podoplanin upregulation may be induced by increased lymph flow to the draining lymph nodes, which occurs in lymphangiogenic tumors unless metastasis is extensive enough to be obstructive (24). Interestingly, both increased lymph flow from the tumor as well as lymph node metastasis appear to depend on tumor-draining lymph node lymphangiogenesis, according to new evidence presented by Alanna Ruddell (Fred Hutchison Cancer Research Center, Seattle, WA). She showed that lymphangiogenesis in the tumor-draining lymph nodes was dependent on B cells and that normally metastatic tumors grown in B-cell-deficient mice failed to provoke lymph node lymphangiogenesis, to increase flow or metastasis. Furthermore, in μ c-Myc mice with B-cell expansion in the lymph node, melanoma and lymphoma metastasis to the sentinel lymph node was increased and more rapid, and hematogeneous metastasis also increased (25). However, metastatic colonization of the same tumors after intravenous injection was unchanged in these mice, supporting the hypothesis that B-cell-driven lymph node lymphangiogenesis affects lymphatic spread of lymphoma and melanoma and that hematogeneous spread occurs after lymphatic spread.

Why does sentinel lymph node lymphangiogenesis promote metastasis? Melody Swartz (Swiss Federal Institute of Technology, Lausanne, Switzerland) presented data suggesting that lymphatic involvement by tumors and lymph node lymphangiogenesis promoted tolerance from host immunity (26). B16 melanoma expression of VEGF-C protected tumors against preexisting, vaccine-induced immunity. VEGF-C upregulated CCL21 in the tumor stroma, which attracted naive T cells and promoted their education in the regulatory chemokine environment (27). In addition, LEC in the sentinel lymph node could cross-present tumor antigen MHC class I molecules leading to CD8⁺ T-cell deletion, supporting a new role for LECs in tolerance. On the other hand, CCL21 in tumors and lymphoid stroma drove antitumor as well as protumor effects by attracting naive and regulatory T cells along with antigen-presenting cells. David Peske (University of Virginia, Charlottesville, VA) from the laboratory of Victor Engelhart showed that CCL21 expression in the stroma of ovalbumin-expressing melanomas could attract adoptively transferred naive ovalbumin-specific CD8⁺ T cells after adoptive transfer from T-cell receptor transgenic mice and activated them in the TMEs. In contrast, naturally arising host CD8⁺ T cells proliferated from a rare population of naive CD8⁺ T cells and existed in balance with regulatory T cells. These studies highlight the importance of context and timing for both antitumor immune responses and tumor tolerance to develop.

The session closed with Dotscho Kerjaschki (University of Vienna, Wien, Austria) describing new work on mammary carcinomas, whose lymph node metastasis correlated with lymphangiogenesis in the sentinel lymph nodes and with metastatic tumors but not with the primary tumor. Histopathology of invasive mammary tumors revealed large gaps in lymphatic vessels where tumor cells entered, and this was consistent with *in vitro* data showing tumor spheroids forming gaps in LEC monolayers. Invasive but not benign tumors induced this gap formation, and only in lymphatic but not blood endothelial cells, in a lipoxygenase-dependent manner. In mice with lipoxygenase knockdown, metastasis was prevented, even in VEGF-C-overexpressing tumors. These exciting new data identify lipoxygenase as a potential new drug target to prevent lymphatic spread of mammary carcinomas (28).

Emerging concept 5: The microbial flora can be friend or foe of cancer

The recent possibility of examining the entire microbiome in the gut is shedding new light on the role of commensal/pathogenic bacteria in cancer initiation and progression. One of the burning questions is how the microbiota regulates the inflammatory components of the TME and affects inflammation-associated carcinogenesis (29). The protumorigenic role of gut *Helicobacter hepaticus* in extra-intestinal carcinogenesis was discussed by Susan Erdman (Massachusetts Institute of Technology, Cambridge, MA) who reported that introduction of *H. hepaticus* to Apc^{Min/+}Rag2^{-/-} mice led to development of colitis and intestinal tumors but also to mammary gland tumors heavily infiltrated with macrophages (30). Systemic anti-TNF- α treatment or adoptive transfer of IL-10 producing

CD4⁺ T regulatory cells abolished both intestinal and mammary tumorigenesis. Because Rag2^{-/-} mice lack both T and B cells, inflammation-associated carcinogenesis found in Apc^{Min/+}Rag2^{-/-} mice was mediated by cells of the innate immune system. The presence of mammary tumors in these mice suggest that *H. hepaticus* inhabiting the gut elicits a systemic inflammatory reaction driven by innate immune cells that is also carcinogenic in tissues not directly in contact with the pathogens. Noriho Iida (NCI, Frederick, MD) from Giorgio Trinchieri's group explored the potential ability of intestinal commensal bacteria to augment antitumor immune responses in treatment-induced acute inflammation. They used a model in which mice subcutaneously implanted with melanoma cells and treated with an anti-IL-10R antibody and intratumoral injection of CpG oligonucleotides developed an intratumoral hemorrhagic necrosis due to production of TNF- α by macrophages and exhibited prolonged survival. He showed that depletion of gut commensal bacteria by administration of antibiotics impaired production of TNF- α in the tumor and decreased survival in treated colon carcinoma and melanoma-bearing mice. Thus, proper activation of innate myeloid cells by CpG nucleotides requires an intact intestinal microbiota. These two presentations illustrate the opposite roles that the microbial flora may have on cancer initiation and progression as a function of the type of inflammation present.

Critical question 1: How should we include the TME in the initial evaluation of a tumor and in preclinical cancer models?

Typically, genomic and transcriptomic analyses of tumors are conducted on DNA and RNA extracted from entire tumors and it is generally assumed that genetic and epigenetic alterations and changes in gene expression observed reflect modifications in the tumor cells. This may not necessarily be the case. Morag Park (McGill University, Montreal, Quebec, Canada) reported results from an extensive transcriptomic analysis of breast cancer specimens in which samples were microdissected to separate stroma from malignant epithelium that were individually analyzed (31). She described stromal-specific signatures that allowed classification of breast cancers into 5 TME-based subgroups. Her laboratory also identified 26 stromal-derived genes that predicted outcomes with a power better than the 70 genes used in the mammaprint test (32). Furthermore, data generated from transgenic mice in which oncogenes were targeted in the mammary epithelium suggested that oncogenes produce distinct patterning changes in the mouse mammary stroma similar to those observed in human breast tumors.

Another important question is the development of preclinical cancer mouse models that take the TME into consideration. The important role played by immune cells in the TME indicates that xenotransplanted tumor models in immunodeficient mice are of limited value in the study of TME. Genetically engineered mice have the advantage to recapitulate an oncogenic event within the context of a competent immune system but they represent murine and not human cancer models. Alana Welm (University of Utah, Salt Lake City, UT) discussed a mouse model where fresh human breast cancer

samples were xenografted into immunodeficient mice along with a component of the human stroma to achieve a high rate of engraftment and spontaneous metastasis (33). The pathology of these tumors faithfully reflected the organization of human tumors. Engraftment was also a prognosticator of outcome as women whose tumors engrafted had a poorer survival than women whose tumors did not engraft. Interestingly, although cotransplantation of a stromal component or of human mesenchymal stem cells increased the efficiency of the xenograft, the mouse stroma was quickly recruited to reshape the TME.

Critical question 2: What should be the strategies to target the microenvironment in cancer therapy?

A fundamental question raised by many of the presentations at the meeting is related to the application of our knowledge of the TME to the design of therapeutic strategies. Therapies solely targeted at the TME are unlikely to eradicate cancer, although they could have the potential to convert cancer into a chronic disease. The major focus of ongoing efforts have thus been on strategies that combine targeting tumor cells and the microenvironment and several presentations showed that targeting the microenvironment in combination with therapies aimed at tumor cells is a valuable approach. A first strategy is the use of agents blocking pathways responsible for the recruitment and activation of stromal cells in the TME as first shown for Avastin, that is now part of the armamentarium to combat colon cancer and glioblastoma (34). William Dougall (Amgen, Seattle, WA) presented data illustrating the efficacy of targeting receptor activator of NF- κ B ligand (RANKL) in bone metastasis with denosumab, a fully human mAb against RANKL (35). Three phase III clinical studies with denosumab recently completed in patients with bone metastasis from breast cancer, castration-resistant prostate cancer (CRPC), and other advanced malignancies showed effective inhibition of bone remodeling and the superiority of denosumab over Zometa (zoledronic acid) in decreasing the number of skeletal-related events in these patients. Denosumab was also effective in delaying the development of bone metastasis in men with CRPC, showing that targeting the TME can also have a preventive effect on metastasis. RANKL is also a mediator of the mitogenic activity of progesterone in mouse mammary epithelium and pharmacologic inhibition of RANKL in progesterone-dependent mouse mammary tumors attenuated tumorigenesis. A second strategy is based on the concept that the TME modulates tumor susceptibility to therapy. Combination therapies that include agents targeting pathways affecting tumor cell resistance to drugs with standard chemotherapy or targeted therapy have garnered renewed excitement. William Dalton (H. Lee Moffitt Cancer Center and Research Institute, Tampa, FL) discussed environment-mediated drug resistance (EMDR) as a mechanism where the interaction between tumor cells and the BM environment allows for discrete tumor populations to survive as minimal residual disease and emerge as drug-resistant clones (36). Interfering with these mechanisms may increase cancer response to therapy and prevent resistance. In myeloma, in which such resistance has been extensively studied, the mechanisms

involve activation of specific pathways such as IL-6/STAT3, SDF1/CXCR4, Notch, or TRAIL and miR that provide tumor cells with a survival advantage. Several inhibitors of such pathways are currently in clinical trials. The ECM can also be a factor of therapeutic resistance and thus a target for therapeutic intervention. Sunil Hingorani (Fred Hutchinson Cancer Research Center) showed that the formation of a hyaluronic acid-rich stroma in pancreatic tumors resulted in unperfused blood vessels that provided a drug-free sanctuary for tumor cells. Treatment of the stroma with hyaluronidase in transgenic mice prone to develop pancreatic cancer was followed by a rapid reperfusion of the blood vessels that led to decreased proliferation, increased apoptosis, increased response to therapy, and improved survival.

A third strategy consists of targeting protumorigenic inflammatory pathways, an approach taken by Frances Balkwill's (Barts Cancer Institute) laboratory. She identified TNF, IL-6, and CXCL12 as a TNF network of 3 key cytokine mediators of cancer-related inflammation, having a paracrine action on angiogenesis, infiltration with myeloid cells, and Notch signaling. She reported that siltuximab, an anti-human IL-6 antibody inhibited IL-6 signaling (STAT3 activation) in cancer cells and had therapeutic effects in xenograft models (37). A phase II clinical trial of siltuximab as single agent in platinum-resistant ovarian cancer indicated that it was well-tolerated and had some therapeutic effects.

Conclusion

This conference illustrated well the high level of complexity of the TME and the challenges ahead in our attempt to ultimately identify therapeutic agents that target the TME. This aspect was illustrated by Michael Karin (University of California San Diego), who gave the closing keynote lecture. His work shows how in certain cases, inflammation can suppress antitumor immunity but can also be used to enhance the efficacy of cancer immunotherapy. Central to inflammation is NF- κ B that can have pro- and anti-inflammatory functions (38). Evidence showing its activation in many inflammatory conditions associated with cancer such as inflammatory bowel

disease, rheumatoid arthritis, or psoriasis raised enthusiasm about NF- κ B and IKK β as therapeutic targets in chronic inflammation, autoimmune diseases, and cancer. However, it was a disappointment to later realize that inhibition of NF- κ B increased or even caused inflammation under certain circumstances. In cancer, NF- κ B can have a pro- or antitumorigenic activity depending on the cancer type and also the mechanism of carcinogenesis involved. To understand this complexity will be critical to avoid premature testing in clinical trials of agents whose activity is not entirely understood, which could result in a premature abandonment of these agents as effective anti-cancer agents. We must remember the lessons learned from the clinical testing of inhibitors of matrix metalloproteinases in the late 1990s when the complexity of their role in cancer was not entirely appreciated at the time they were clinically tested (39). This is therefore a challenging but also a very exciting time for investigators studying the TME.

Disclosure of Potential Conflicts of Interest

No potential conflicts of interests were disclosed.

Authors' Contributions

Conception and design: M.A. Swartz, M.H. Wong, Y.A. DeClerck
Writing, review, and/or revision of the manuscript: M.A. Swartz, N. Iida, E. W. Roberts, S. Sangaletti, M.H. Wong, F.E. Yull, L.M. Coussens, Y.A. DeClerck
Administrative, technical, or material support (i.e., reporting or organizing data, constructing databases): Y.A. DeClerck

Y.A. DeClerck chaired the editorial committee that was responsible for summarizing the presentations at the meeting. M.A. Swartz, N. Iida, E.W. Roberts, S. Sangaletti, M.H. Wong, F.E. Yull, and Y.A. DeClerck equally contributed to the summary of the various sessions of the meeting.

Acknowledgments

The authors thank Amy Baran, Amy Flynn, and Kacie Sheppeck for their assistance in the planning and conduct of the meeting. They also thank J. Rosenberg for her assistance in the preparation of the manuscript.

Grant Support

The meeting was supported by Genentech, Teva Pharmaceuticals, Amgen, Bristol Myers Squibb, and Hypoxigen, and a conference grant, R13 CA165812, from the NIH to Y.A. DeClerck and the AACR.

Received January 17, 2012; revised February 23, 2012; accepted March 5, 2012; published OnlineFirst March 13, 2012.

References

1. Hanahan D, Weinberg RA. Hallmarks of cancer: the next generation. *Cell* 2011;144:646–74.
2. Tumor Microenvironment Network [homepage on the Internet]. Bethesda, MD: NCI. Available from: <http://tmen.nci.nih.gov/>.
3. Borges VF, Schedin PJ. Pregnancy-associated breast cancer: an entity needing refinement of the definition. *Cancer*. 2011 Nov 15. [Epub ahead of print].
4. Koehne CH, DuBois RN. COX-2 inhibition and colorectal cancer. *Semin Oncol* 2004;31:12–21.
5. DuFort CC, Paszek MJ, Weaver VM. Balancing forces: architectural control of mechanotransduction. *Nat Rev Mol Cell Biol* 2011;12:308–19.
6. Patel LR, Camacho DF, Shiozawa Y, Pienta KJ, Taichman RS. Mechanisms of cancer cell metastasis to the bone: a multistep process. *Future Oncol* 2011;7:1285–97.
7. Dvorak HF, Weaver VM, Tlsty TD, Bergers G. Tumor microenvironment and progression. *J Surg Oncol* 2011;103:468–74.
8. Shurin GV, Ouellette CE, Shurin MR. Regulatory dendritic cells in the tumor immunoenvironment. *Cancer Immunol Immunother* 2011;61: 223–30.
9. Denardo DG, Brennan DJ, Rexhepaj E, Ruffell B, Shiao SL, Madden SF, et al. Leukocyte complexity predicts breast cancer survival and functionally regulates response to chemotherapy. *Cancer Discov* 2011; 1:54–67.
10. Connelly L, Barham W, Onishko HM, Chen L, Sherrill TP, Zabuawala T, et al. NF- κ B activation within macrophages leads to an anti-tumor phenotype in a mammary tumor lung metastasis model. *Breast Cancer Res* 2011;13:R83.
11. Keith B, Johnson RS, Simon MC. HIF1alpha and HIF2alpha: sibling rivalry in hypoxic tumour growth and progression. *Nat Rev Cancer* 2011;12:9–22.
12. Schioppa T, Moore R, Thompson RG, Rosser EC, Kulbe H, Nedospasov S, et al. B regulatory cells and the tumor-promoting actions of TNF- α during squamous carcinogenesis. *Proc Natl Acad Sci U S A* 2011;108:10662–7.
13. Sangaletti S, Tripodo C, Cappetti B, Casalini P, Chiodoni C, Piconese S, et al. SPARC oppositely regulates inflammation and fibrosis in bleomycin-induced lung damage. *Am J Pathol* 2011;179: 3000–10.

14. Soldati R, Berger E, Zenclussen AC, Jorch G, Lode HN, Salatino M, et al. Neuroblastoma triggers an immuno-evasive program involving galectin-1-dependent modulation of T cell and dendritic cell compartments. *Int J Cancer* 2011 Oct 23. [Epub ahead of print].
15. Topalian SL, Weiner GJ, Pardoll DM. Cancer immunotherapy comes of age. *J Clin Oncol* 2011;29:4828–36.
16. Calvo F, Sahai E. Cell communication networks in cancer invasion. *Curr Opin Cell Biol* 2011;23:621–9.
17. Sanz-Moreno V, Gaggioli C, Yeo M, Albrengues J, Wallberg F, Viros A, et al. ROCK and JAK1 signaling cooperate to control actomyosin contractility in tumor cells and stroma. *Cancer Cell* 2011;20:229–45.
18. Carothers AM, Rizvi H, Hasson RM, Heit YI, Davids JS, Bertagnolli MM, et al. Mesenchymal stromal cell mutations and wound healing contribute to the etiology of desmoid tumors. *Cancer Res* 2012;72: 346–55.
19. Thery C, Zitvogel L, Amigorena S. Exosomes: composition, biogenesis and function. *Nat Rev Immunol* 2002;2:569–79.
20. Peinado H, Lavotshkin S, Lyden D. The secreted factors responsible for pre-metastatic niche formation: old sayings and new thoughts. *Semin Cancer Biol* 2011;21:139–46.
21. Powell AE, Anderson EC, Davies PS, Silk AD, Pelz C, Impey S, et al. Fusion between intestinal epithelial cells and macrophages in a cancer context results in nuclear reprogramming. *Cancer Res* 2011;71: 1497–505.
22. Alitalo A, Detmar M. Interaction of tumor cells and lymphatic vessels in cancer progression. *Oncogene* 2011 Dec 19. [Epub ahead of print].
23. Kitano H, Kageyama S, Hewitt SM, Hayashi R, Doki Y, Ozaki Y, et al. Podoplanin expression in cancerous stroma induces lymphangiogenesis and predicts lymphatic spread and patient survival. *Arch Pathol Lab Med* 2010;134:1520–7.
24. Proulx ST, Detmar M. Watching lymphatic vessels grow by making them glow. *Cell Res* 2011;22:12–3.
25. Ruddell A, Harrell MI, Furuya M, Kirschbaum SB, Iritani BM. B lymphocytes promote lymphogenous metastasis of lymphoma and melanoma. *Neoplasia* 2011;13:748–57.
26. Lund AW, Swartz MA. Role of lymphatic vessels in tumor immunity: passive conduits or active participants? *J Mammary Gland Biol Neoplasia* 2010;15:341–52.
27. Shields JD, Kourtis IC, Tomei AA, Roberts JM, Swartz MA. Induction of lymphoidlike stroma and immune escape by tumors that express the chemokine CCL21. *Science* 2010;328:749–52.
28. Kerjaschki D, Bago-Horvath Z, Rudas M, Sexl V, Schneckenleithner C, Wolbank S, et al. Lipoxygenase mediates invasion of intrametastatic lymphatic vessels and propagates lymph node metastasis of human mammary carcinoma xenografts in mouse. *J Clin Invest* 2011;121: 2000–12.
29. Parsonnet J, Friedman GD, Vandersteen DP, Chang Y, Vogelman JH, Orentreich N, et al. Helicobacter pylori infection and the risk of gastric carcinoma. *N Engl J Med* 1991;325:1127–31.
30. Fox JG, Ge Z, Whary MT, Erdman SE, Horwitz BH. Helicobacter hepaticus infection in mice: models for understanding lower bowel inflammation and cancer. *Mucosal Immunol* 2011;4:22–30.
31. Bertos NR, Park M. Breast cancer - one term, many entities? *J Clin Invest* 2011;121:3789–96.
32. Glas AM, Floore A, Delahaye LJ, Witteveen AT, Pover RC, Bakx N, et al. Converting a breast cancer microarray signature into a high-throughput diagnostic test. *BMC Genomics* 2006;7:278.
33. DeRose YS, Wang G, Lin YC, Bernard PS, Buys SS, Ebbert MT, et al. Tumor grafts derived from women with breast cancer authentically reflect tumor pathology, growth, metastasis and disease outcomes. *Nat Med* 2011;17:1514–20.
34. Ferrara N. From the discovery of vascular endothelial growth factor to the introduction of avastin in clinical trials - an interview with Napoleone Ferrara by Domenico Ribatti. *Int J Dev Biol* 2011;55:383–8.
35. Dougall WC. Osteoclast-dependent and-independent roles of the RANKL/RANK/OPG pathway in tumorigenesis and metastasis. *Clin Cancer Res* 2012;18:326–35.
36. Meads MB, Gatenby RA, Dalton WS. Environment-mediated drug resistance: a major contributor to minimal residual disease. *Nat Rev Cancer* 2009;9:665–74.
37. Coward J, Kulbe H, Chakravarty P, Leader D, Vassileva V, Leinster DA, et al. Interleukin-6 as a therapeutic target in human ovarian cancer. *Clin Cancer Res* 2011;17:6083–96.
38. Ben Neriah Y, Karin M. Inflammation meets cancer, with NF- κ B as the matchmaker. *Nat Immunol* 2011;12:715–23.
39. Coussens LM, Fingleton B, Matrisian LM. Matrix metalloproteinase inhibitors and cancer: trials and tribulations. *Science* 2002;295: 2387–92.

Size- and charge-dependent non-specific uptake of PEGylated nanoparticles by macrophages

Shann S Yu^{1,2}
Cheryl M Lau¹
Susan N Thomas³
W Gray Jerome⁴
David J Maron⁵
James H Dickerson^{2,6}
Jeffrey A Hubbell³
Todd D Giorgio^{1,2,7,8}

¹Department of Biomedical Engineering, Vanderbilt University, Nashville, ²Vanderbilt Institute of Nanoscale Science and Engineering, Nashville, TN, USA; ³Institute of Bioengineering, École Polytechnique Fédérale de Lausanne, Lausanne, Switzerland, ⁴Department of Pathology, Vanderbilt University Medical Center, Nashville, ⁵Vanderbilt Heart and Vascular Institute, Nashville, ⁶Department of Physics and Astronomy, Vanderbilt University, Nashville, ⁷Department of Cancer Biology, Vanderbilt University Medical Center, Nashville, ⁸Department of Chemical and Biomolecular Engineering, Vanderbilt University, Nashville, TN, USA

Abstract: The assessment of macrophage response to nanoparticles is a central component in the evaluation of new nanoparticle designs for future in vivo application. This work investigates which feature, nanoparticle size or charge, is more predictive of non-specific uptake of nanoparticles by macrophages. This was investigated by synthesizing a library of polymer-coated iron oxide micelles, spanning a range of 30–100 nm in diameter and –23 mV to +9 mV, and measuring internalization into macrophages in vitro. Nanoparticle size and charge both contributed towards non-specific uptake, but within the ranges investigated, size appears to be a more dominant predictor of uptake. Based on these results, a protease-responsive nanoparticle was synthesized, displaying a matrix metalloproteinase-9 (MMP-9)-cleavable polymeric corona. These nanoparticles are able to respond to MMP-9 activity through the shedding of 10–20 nm of hydrodynamic diameter. This MMP-9-triggered decrease in nanoparticle size also led to up to a six-fold decrease in nanoparticle internalization by macrophages and is observable by T_2 -weighted magnetic resonance imaging. These findings guide the design of imaging or therapeutic nanoparticles for in vivo targeting of macrophage activity in pathologic states.

Keywords: macrophage targeting, poly(ethylene glycol) (PEG), poly(propylene sulfide) (PPS), iron oxides, opsonization

Introduction

As one of the most phagocytic cells in the human body, macrophages are among the first cells of the innate immune system to arrive at a site of injury, but also have been observed as permanent residents in certain organs, such as in the liver and bone marrow.^{1–3} They function to clear pathogens and microbes, as well as host cell and matrix debris that are present at sites of tissue injury. Macrophages recognize and interact with this multitude of potential targets through a variety of mechanisms, including phagocytosis and receptor-mediated endocytosis. The latter is mediated primarily through pattern recognition receptors, which include toll-like receptors, the mannose receptor (CD206), and scavenger receptor A (CD204).^{4–6} The polygamous nature of these pattern-recognition receptors is not restricted to natural ligands and targets. For example, CD204 has a wide range of molecular partners, leading to receptor-mediated endocytosis, distinct from the non-specific uptake due to pinocytosis.⁷ For the purposes of this manuscript, we have defined this polygamous behavior as “non-specific” uptake or internalization. This is emphasized by evidence that CD204 has been shown to contribute to the non-specific uptake of nanoparticles surface-functionalized with carboxylic acids, antibodies, as well as synthetic polymers.^{8,9} Therefore, the rational design of nanoparticles for in vivo use requires an application-driven minimization

Correspondence: Todd D Giorgio
Vanderbilt University, VU Station B,
Box 351631, Nashville, TN 37235, USA
Tel +1 615 343 1099
Fax +1 615 343 7919
Email todd.d.giorgio@vanderbilt.edu

or optimization of such non-specific interactions between macrophages and synthetic nanoparticles. However, this area remains largely uninvestigated.

Non-specific interactions between macrophage receptors and nanoparticles may be dictated by a variety of characteristics, including particle size, shape, surface charge, and hydrophobicity, and facilitated by surface chemistry-specific complement activation on the nanoparticle.^{10,11} Doshi and Mitragotri treated macrophages at 4°C with a library of polystyrene microparticles exhibiting a variety of sizes and shapes to mimic bacterial dimensions, and observed optimal attachment for rod-shaped particles with the longest dimension at 2–3 µm.¹¹ However, the smallest particles investigated were in the range of 500 nm; work with such nanoparticles has yet to be extended to the sub-100 nm dimensional range, which is of interest in many in vivo applications. Raynal et al showed that macrophages exhibit size-dependent uptake of nanoparticles functionalized with dextran, but macrophages can interact directly with dextran, as their expression of a dextran receptor (SIGNR1) was later documented.^{12,13}

Therefore, in this work, we sought to investigate non-specific uptake of synthetic nanoparticles by macrophages, extending the work of these earlier groups into sub-100 nm PEGylated nanoparticles. To our knowledge, this is the first investigation of the effects of nanoparticle size, surface chemistry, and charge on non-specific uptake by macrophages. The rationale for using a PEG-functionalized nanoparticle system to accomplish these objectives is that macrophages are unlikely to have specific receptors for poly(ethylene glycol) (PEG). Further, PEG can be easily modified to display various chemical functionalities, enabling the modulation of nanoparticle charge without significantly varying the bulk properties of the PEG coating. This is also a relevant model system for study because PEGylation of nanoparticles is commonly performed in order to render synthetic nanoparticles water-soluble and applicable for in vivo use. This is, in part, because PEG has been shown to discourage protein adsorption and opsonization on nanomaterial surfaces.¹⁴

Therefore, we used block copolymers of poly(ethylene glycol)-bl-poly(propylene sulfide) (PEG-PPS), which are amphiphilic copolymers that are capable of forming micelles and stabilizing hydrophobic drugs and nanoparticles at their liquid, PPS core.^{15,16} The incorporation of ultrasmall superparamagnetic iron oxides (USPIOs) into the micellar core of PEG-PPS block copolymers serves two functional purposes – enabling easy quantification of particle uptake through colorimetric assays, while also being a widely investigated contrast agent for T_2 -weighted magnetic resonance

imaging (MRI). Through the use of a variety of materials processing techniques to form the micelles, including thin film hydration and direct hydration, the same starting PEG-PPS copolymers and iron oxide cores can lead to monodisperse micelles (PEG-PPS-USPIOs) exhibiting hydrodynamic diameters at 30 nm, 40 nm, or 100 nm. Additionally, PEG-PPS-USPIOs can be fashioned with different surface chemistries at the PEG terminus, enabling an examination of charge-dependent non-specific uptake of nanoparticles by the macrophages.

To demonstrate the utility of these studies, we evaluated a protease-activity MRI probe design against these results. To make activity probes, PEG chains containing a protease-cleavable peptide substrate were synthesized and conjugated to PPS, in order to fashion surfactants for the micellization of USPIOs. The resulting nanoparticles are “activatable” by protease activity through a ≥ 10 nm decrease in hydrodynamic diameter. Macrophages are therefore expected to internalize protease-treated nanoparticles differently than untreated nanoparticles. We hypothesize that these differences can be visualized via MRI with the aid of the contrast agent USPIOs encapsulated within the micelles. Taken together, the work presented here shows methods to design ideal nanoparticle dimensions and properties in order to better optimize nanoparticle behavior in vivo.

Materials and methods

All reagents were purchased from Sigma-Aldrich (St Louis, MO) and used as purchased unless otherwise noted below. Matrix metalloproteinase-9 (MMP-9), MMP-9 inhibitor, Fmoc-protected L-amino acids, and resins for solid-phase peptide synthesis were purchased from EMD Biosciences (Gibbstown, NJ). PEG reagents were purchased from Laysan Biosciences (Arab, AL). All dialysis supplies were ordered from Pierce Scientific (Rockford, IL) and used with modifications to the factory-provided protocol as indicated in the appropriate sections below. Copper transmission electron microscopy (TEM) grids with Formvar film and uranyl acetate were purchased from Electron Microscopy Sciences (Hatfield, PA). GIBCO® RPMI-1640 medium, penicillin-streptomycin, and fetal bovine serum (FBS) were purchased from Life Technologies (Carlsbad, CA).

PEG-PPS block copolymers and functionalization

Synthesis of approximately 7 kDa carboxy-PEG-PPS (cPEG-PPS) was carried out as previously described.¹⁶ For fluorescent polymers, FITC-PEG-NH₂ was used

in place of cPEG-NH₂ in the coupling reaction to PPS. The MMP-9-cleavable peptide GGPQRQITAGC (M9C; Gly-Gly-Pro-Arg-Gln-Ile-Thr-Ala-Gly-Cys)¹⁷ was synthesized on a Rink-amide MBHA resin support, via standard Fmoc-based solid phase peptide synthesis on an automated system (Protein Technologies PS3, Tucson, AZ).¹⁸ The peptide (1.5 eq, 45 mmol) was then reacted overnight with 1 eq of 5 kDa methoxy-PEG-maleimide (mPEG-MAL; 30 mmol; 150 mg), in an aqueous buffer containing 0.1 M Na₃PO₄ and 0.15 M NaCl at pH 7.2. Unbound peptide was removed by dialysis across a 2 kDa molecular weight cutoff membrane overnight at room temperature. The completed mPEG-[M9C] conjugate was lyophilized, then coupled to cPEG-PPS via standard carbodiimide chemistry to yield mPEG-[M9C]-PEG-PPS block copolymers.

For Fourier transform infrared (FT-IR) spectroscopy, polymer samples were prepared by mixing with IR-grade KBr and pelleting on a KBr press (Specac, Slough, UK). FT-IR was performed on a Bruker Tensor 27 system (Billerica, MA).

Proton nuclear magnetic resonance (1H NMR) spectra were obtained at 400 MHz using a 9.4 Tesla Oxford magnet operated by a Bruker AV-400 console. The main NMR probe for the instrument is a 5 mm Z-gradient broadband inverse (BBI) probe with automatic tuning and matching capability (ATM).

Gel permeation chromatography (GPC) was performed on three resolving columns running in series (1 × TSKGel Alpha4000, 2 × TSKGel Alpha3000; Tosoh Bioscience, King of Prussia, PA) with dimethylformamide (DMF) + 0.1 M LiBr mobile phase. Columns were incubated at 60°C, and chromatograms were obtained with a Shimadzu SPD-10A UV detector and RID-10A refractive index detector (Shimadzu Scientific Instruments, Columbia, MD), and a Wyatt miniDAWN Treos multi-angle light scattering detector (MALS; Wyatt Technology, Santa Barbara, CA). Data collection and analysis was achieved through the Wyatt ASTRA software (v 5.3.4).

Encapsulation of USPIOs in PEG-PPS copolymers

Synthesis of hydrophobic, monodisperse USPIO core particles and their encapsulation in PEG-PPS copolymers was carried out as previously described.¹⁶ In brief, USPIO cores of predictable diameters were first synthesized through thermal decomposition, by controlling the molar ratios of iron precursor to oleic acid introduced in the reaction feed (Supplementary Figure S1). A 1:2 mass ratio of dried

hydrophobic USPIO cores to PEG-PPS polymers were then dissolved in toluene, vortexed to mix, sonicated for 5 seconds to break apart clumps, and then dried by rotary evaporation for 20 minutes. The dried polymer/USPIO mixture was then rehydrated in 3 mL of nanopure water and vortexed vigorously to suspend all particulates. Large clumps and byproducts were removed by magnetic pelletting, and the colloidal phase was collected and further centrifuged at 2500 g for 5 minutes to precipitate excess polymers. The supernatant is gently aspirated by pipette into fresh scintillation vials and stored at 4°C.

To fabricate fluorescent micelles, a 1:40:20.5 mass ratio of FITC-PEG-PPS:PEG-PPS:iron oxide cores was mixed and micellized as described above. Therefore, the overall mass ratio of polymers to iron oxides is preserved at 1:2 for all micellization procedures. To make “proximity-activated” USPIOs (PA-USPIOs) – which are able to respond to local MMP-9 activity, OA-USPIOs were encapsulated in MMP-9-cleavable mPEG-[M9C]-PEG-PPS polymers using the same protocol.

Pluronic®-PPS nanoparticles and loading with USPIOs

Pluronic-stabilized PPS nanoparticles (NPs) were synthesized by inverse emulsion polymerization as described previously.^{10,19} Pluronic F-127 (a block copolymer of polyethylene glycol and polypropylene glycol terminated by α and ω hydroxyl groups) was used alone or in combination with carboxyl-terminated Pluronic derivatized as previously described.²⁰ The hydrophobic core was stabilized by disulfide crosslinking of the linear PPS chains.¹⁹ However, since crosslinking cannot reach completion, remaining free sulphydryl groups on the NP surface were irreversibly capped by reaction with the alkylating reagent iodoacetamide. NP solutions were sterile-filtered, and then loaded with 3 nm USPIO cores through a direct hydration process. Then 100 μ L of the hydrophobic OA-USPIOs (20 mg/mL in tetrahydrofuran [THF]) was added to 1 mL of the Pluronic-PPS NPs (15 mg/mL in water) with swirling, and was followed by removal of THF by rotary evaporation, and removal of non-encapsulated OA-USPIOs by filtration through 0.45 μ m Teflon filters (Whatman Inc, Piscataway, NJ).

Nanoparticle characterization

Size and ζ -potential of NPs were investigated by dynamic light scattering (DLS) in a Malvern Zetasizer Nano-ZS with the reusable dip-cell kit (Malvern Instruments Ltd, Worcestershire, UK). For measurements of ζ -potential in

serum media, nanoparticles were mixed with THP-1 growth medium and allowed to incubate at 37°C for 24 hours prior to DLS measurements. No further purification of the nanoparticles was performed. This is because the purification process ends up diluting the particles (along with the adsorbed proteins), and may lead to further protein exchange interactions with media used downstream of isolation procedures, as per the Vroman effect.¹⁴ Therefore, in order to best mimic in vivo conditions, the nanoparticles were measured in the presence of serum. Measurements of hydrodynamic diameter demonstrated the presence of a peak at <5 nm that corresponded to proteins, while nanoparticles could still be easily discerned within the 20–100 nm diameter range.

Transmission electron microscopy (TEM) was conducted on a Philips CM20 system (Amsterdam, the Netherlands) operating at 200 kV. Carbon film-backed copper grids were inverted onto droplets containing nanoparticle suspensions of interest and blotted dry. Images were collected using a CCD camera with AMT Image Capture Engine software (v 600.335h built on 29 Apr 2010; Advanced Microscopy Techniques, Danvers, MA), and sizing of the particles was automated using a particle analyzer on ImageJ software (v 1.43u). Images were thresholded, and then the built-in (Analyze Particles) function was used to measure the major and minor axes of the fit ellipses around each particle. After artificially discarding clumps of particles encompassed within single fit ellipses (usually identified by major and minor axes that were >10% different from one another), or ellipses drawn around globs in the carbon grid (usually identified by any dimension <1 nm), the diameter of individual particles was taken to be the average of the major and minor axis.

For aqueous samples, nanoparticles on TEM grids were also counterstained with 3% uranyl acetate in water for 2 minutes, gently blotted dry, and dried in a vacuum desiccator for 2 hours prior to imaging.

Cell culture and nanoparticle co-incubation experiments

Non-adherent THP-1 human leukemic monocytes (American Type Culture Collection, Manassas, VA) were grown in RPMI-1640 medium supplemented with 10% FBS, 1% penicillin-streptomycin, 1 × MEM vitamins (Mediatech, Manassas, VA), 120 μM β-mercaptoethanol, and 10 mM HEPES® (Sigma-Aldrich) at 37°C in a 5% CO₂ incubator. For all cell experiments, monocytes were seeded into standard tissue culture-treated plates at a density of 300,000 cells/cm², and differentiated for 3 days in growth medium (above) supplemented with 200 nM of phorbol myristate acetate (PMA).

The differentiation process leads to induction of cell adherence onto tissue culture polystyrene surfaces.

For nanoparticle co-incubation experiments, cells were washed once with phosphate buffered saline (PBS) to remove unbound cells, prior to addition of growth medium. The medium was supplemented with nanoparticles and fucoidan. Nanoparticle dosing was based on total iron concentration as measured through the colorimetric phenanthroline assay as previously described.²¹ Final iron concentrations in the wells were calculated to be between 30 μM and 200 μM. For fucoidan competition experiments, media was supplemented with fucoidan to a final concentration of 0–500 μM.

At selected time points, cells were washed three times with PBS to remove unbound nanoparticles, and then lysed in 3 N HCl and 0.25% Triton X-100 for at least 2 hours. The strongly acidic environment also promotes solubilization of the endocytosed USPIOS via oxidation of the amphiphilic PEG-PPS shell on the nanoparticles into fully hydrophilic polymers,¹⁹ as well as leaching and mineralization of the iron in the USPIO core. The cell lysate was analyzed for protein content using a commercial Lowry protein assay kit (Bio-Rad Laboratories, Hercules, CA), while iron content was measured using the colorimetric phenanthroline assay as previously described.²¹ While the acidic conditions for the Lowry protein assay deviate significantly from the protocol described by the supplier (alkaline conditions), this does not significantly affect the sensitivity or results of the assay (Supplementary Figure S2).

Calculation of nanoparticle internalization was dependent upon nanoparticle type, as shown in Table 1. The rationale behind the two different measurement types is inherent to the loading efficiencies possible. Because PEG-PPS-USPIO samples are purified, all cell-nanoparticle interactions in experiments involving them involve an iron “tag”. However, since Pluronic-PPS-USPIOS are a subpopulation of the nanoparticles used in this system, not all cell-nanoparticle interactions here involve the iron tag. Due to differing USPIO loading efficiencies across the different Pluronic-PPS surface chemistries available to us, an additional normalization method was required in order that resulting figures fully represented charge-dependent uptake of nanoparticles. The normalization of internalization data to the initially administered dose of iron was therefore used to report internalization of Pluronic-PPS-USPIOS (Table 1).

For cell viability experiments, cells were incubated for 24 hours with PEG-PPS-USPIOS, at a final iron dose of 30 μM, 60 μM, or 120 μM. After rinsing cells three times with PBS to remove unbound nanoparticles, they were

Table 1 Quantification of nanoparticle uptake into THP-1 cells

Nanoparticle type	Required measurements	Units	Equation	Rationale
PEG-PPS-USPIOS	[Fe] and [Protein] in cell lysates	µg Fe/mg protein	$\frac{[Fe]}{[Protein]}$	Result is a quantity normalized to cell number, but reflects dose-dependence and cell number-dependence of quantified internalization
Pluronic-PPS-USPIOS	[Fe] and [Protein] in cell lysates, and $[Fe]_0$ (concentration of iron administered at time 0)	%/mg protein	$\left(\frac{[Fe]}{[Fe]_0} \right) \times 100$	Different surface chemistries led to differing loading efficiencies of Pluronic-PPS nanoparticles with USPIOS. Quantification method enables experiments to be run at constant nanoparticle concentrations, without worry of effects of different loading efficiencies on measured iron internalization

Notes: PEG-PPS-USPIO internalization data was also represented as %ID/mg once in this manuscript (Figure 3E) in order to facilitate comparison of results.

Abbreviations: PEG, poly(ethylene glycol); PPS, poly(propylene sulfide); USPIO, ultrasmall superparamagnetic iron oxides.

stained with a commercial calcein-AM/ethidium homodimer live/dead assay kit (Invitrogen, Carlsbad, CA), and quantified according to the manufacturer's instructions.

Protease-activatable nanoparticles

“Proximity-activated” USPIOS (PA-USPIOS) – which are able to respond to local MMP-9 activity, were formed as described for other PEG-PPS-USPIOS above. For protease experiments, 50 µL PA-USPIOS (iron dose = 600 µM) were incubated with 10 µL MMP-9 (final concentration = 2 µg/mL) in an aqueous buffer containing 0.1 M HEPES, 0.15 M NaCl, and 5 mM CaCl₂ (pH 7.2) for 24 hours at 37°C. For control experiments, PA-USPIOS were incubated with buffer only. Following cleavage, nanoparticles were added directly to cell cultures. The final concentration of iron and MMP-9 in the cell cultures were 120 µM and 400 ng/mL, respectively. In some control experiments, MMP-9 inhibitor was also added to the cell cultures, to a final concentration of 300 ng/mL.

Magnetic resonance imaging (MRI)

MRI was performed on a Varian 4.7 T horizontal bore imaging system. *T*₂ signal decay was measured using a Carr-Purcell-Meiboom-Gill (CPMG) spin-echo pulse sequence with N = 8 echoes with 6.5 ms echo spacing. The signal from each voxel at the eight imaging time points was fit to a mono-exponential signal decay model to determine *T*₂ for each voxel:

$$S = S_0 e^{-\frac{t}{T_2}} \quad (1)$$

A region of interest (ROI) was manually drawn using MATLAB (MathWorks, Inc, Natick, MA) for the first imaging time point and translated to the images from later echoes. The mean *T*₂ and standard deviation for each well

was then calculated from all voxels within this ROI. Other imaging parameters included TR = 2 seconds, field of view = 22 mm × 22 mm, data matrix = 128 × 128, slice thickness = 1 mm, number of acquisitions = 24 (total scan time approximately 1 hour 45 minutes).

To prepare cells for MRI, the supernatant containing unbound nanoparticles in medium was aspirated and replaced with PBS, prior to scraping of the cells into the buffer (Corning Life Sciences, Lowell, MA). Cells were centrifuged into a pellet at 300 g for 5 minutes, and rinsed with PBS twice more. Cells were then fixed with 10% buffered formalin, gently mixed, and allowed to incubate for 30 minutes at room temperature before they were pelleted and imaged.

Results and discussion

The primary objective of this study was to investigate size- and charge-dependent non-specific uptake of nanoparticles by macrophages. With the targeted size range being in the sub-100 nm hydrodynamic diameter range, the objectives required the synthesis of a library of highly monodisperse, water-soluble nanoparticles in order to reduce size overlap between different nanoparticle formulations and elucidate trends between size and uptake. Therefore, USPIO cores were synthesized by thermal decomposition in organic solvents, which led to oleic acid-stabilized USPIOS (OA-USPIOS) of 3.0 ± 0.4 nm (Figure 1A, n approximately 200) and 12.0 ± 1.0 nm (Figure 1B, n > 400). Control over USPIO core diameters was accomplished by adjusting the molar ratios of oleic acid surfactant to iron pentacarbonyl precursor in the reaction feed, and to date, we have synthesized OA-USPIOS of up to 24 nm in diameter using this method (Supplementary Figure S1). These results extend previous work by Woo et al,²² who showed the ability to synthesize particles from 5 nm to 19 nm in diameter using this same exact method. Additionally, we were also able to scale up this original synthesis and now are able to produce the uniform OA-USPIOS in 1 g amounts.

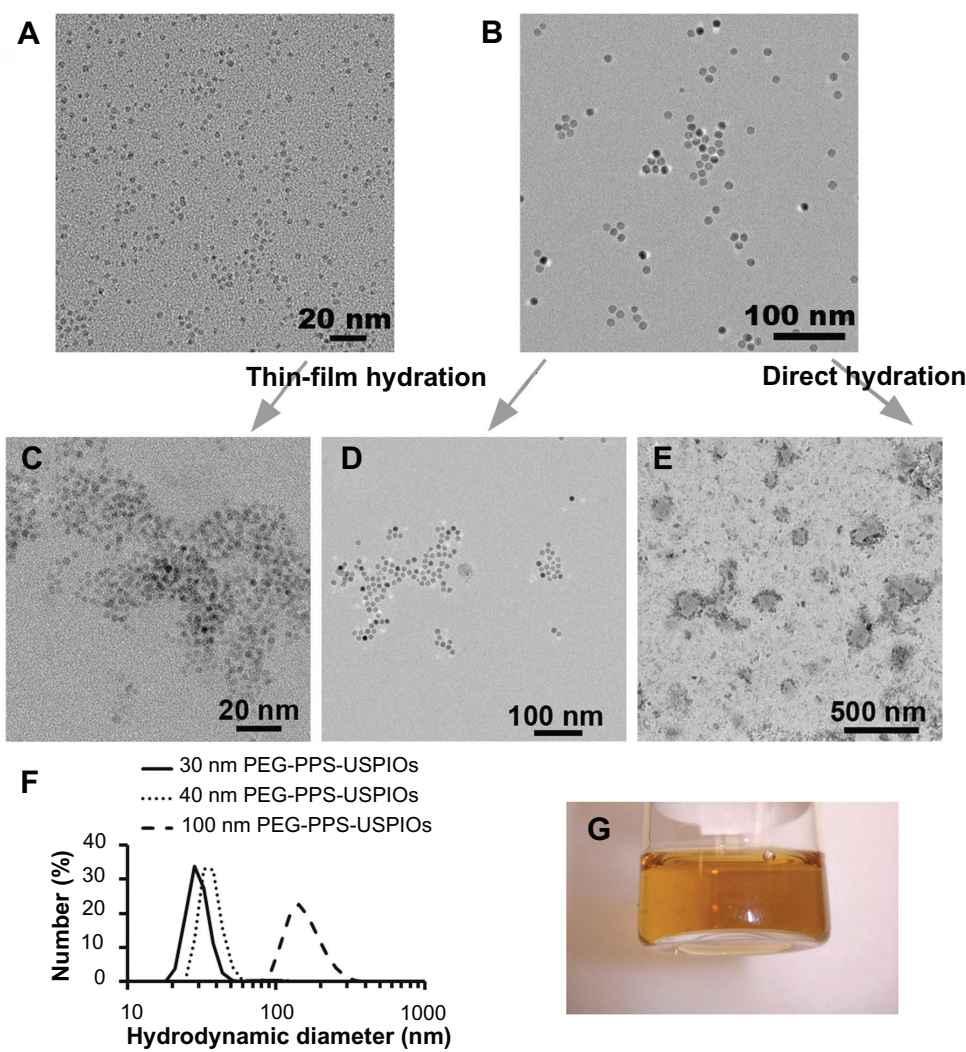


Figure 1 Characterization of USPIOs and PEG-PPS-USPIO micelles. HRTEM images of (A) 3 nm and (B) 12 nm hydrophobic, oleic acid-stabilized USPIO cores (γ -Fe₂O₃), which were synthesized via thermal decomposition. To render particles water-soluble, they were coated with PEG-PPS block copolymers via thin-film hydration to yield, respectively, (C) 30 nm and (D) 40 nm PEG-PPS-USPIO micelles. (E) 100 nm PEG-PPS-USPIO micelles can also be synthesized via direct hydration using the same feed materials used to create micelles in (D); this TEM image has been counterstained with 3% uranyl acetate. (F) Size-number distributions of these PEG-PPS-USPIO micelles were obtained by dynamic light scattering. (G) As shown in this representative photograph, 40 nm PEG-PPS-USPIOs remain stable in water and do not flocculate even after storage at room temperature over 4 months.

Note: Scale bars: (A and C) 20 nm; (B and D) 100 nm; (E) 500 nm.

Abbreviations: HRTEM, high resolution transmission electron microscope; PEG, poly(ethylene glycol); PPS, poly(propylene sulfide); TEM, transmission electron spectroscopy; USPIO, ultrasmall superparamagnetic iron oxides.

To render the OA-USPIOs water-soluble, either a thin-film hydration or a direct hydration method was employed, effectively encapsulating OA-USPIOs within micelles composed of amphiphilic PEG-PPS block copolymers (1.65 kDa PPS block, 4.2 kDa PEG block; Figure 1C–E). Prior to cell experiments, the micelles were sterile-filtered; size-number distributions of the completed USPIO-loaded micelles are shown in Figure 1F. However, due to the larger size of the 100 nm micelles, these materials tended to be caught in the Teflon filters and were thus used as synthesized. The 30 nm and 40 nm micelles were particularly stable in water and flocculated minimally even after storage for several months

at room temperature (Figure 1G). These two formulations were also extremely difficult to pellet by centrifugation or through the influence of an externally-applied 1 T neodymium magnet. The completed micelles exhibited ζ -potentials that were weakly anionic (Table 2), owing partly to the terminal mono-methyl ether group on the PEG block that is displayed on the nanoparticle surface.

Nanoparticles were next administered to THP-1 human leukemic macrophages in order to establish a quantitative basis for the remainder of the experiments, while also examining the kinetics of particle uptake. THP-1 cells were chosen for this study because uptake and processing of lipid nanoparticles by

Table 2 Size and ζ -potential of as-synthesized PEG-PPS-USPIO micelles

Sample name	USPIO core diameter (nm)	Micelle diameter range (nm) ^a	ζ -potential (mV)
30 nm PEG-PPS-USPIOs	3	30.0 \pm 2.6	-2.8 \pm 5.9
40 nm PEG-PPS-USPIOs	12	36.6 \pm 11.9	-1.7 \pm 4.6
100 nm PEG-PPS-USPIOs	12		-7.8 \pm 5.1

Notes: ^aDetermined after filtration through a 0.45 μ m PTFE filter. 100 nm PEG-PPS-USPIOs were not as stable to filtration and were not subjected to this additional treatment step prior to use in cell experiments.

Abbreviations: PEG, poly(ethylene glycol); PPS, poly(propylene sulfide); USPIO, ultrasmall superparamagnetic iron oxides.

THP-1 and primary human monocyte-derived macrophages is not significantly different between the two cell types.^{23,24} We expected, therefore, that macrophage interactions with synthetic nanoparticles can be similarly modeled through this readily available, *in vitro* system.

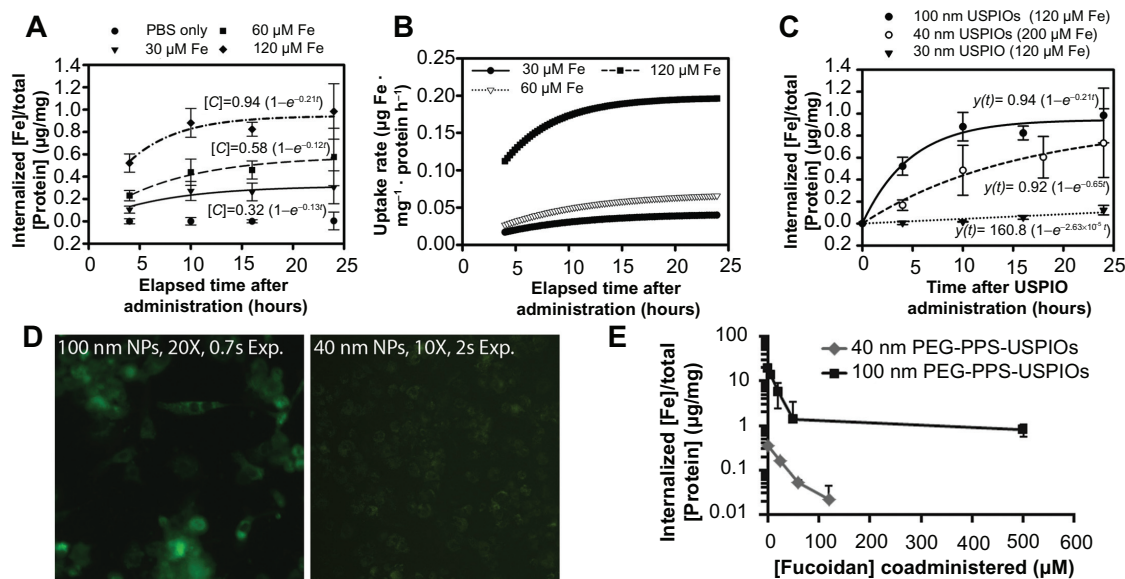


Figure 2 Dose- and size-dependent internalization of PEG-PPS-USPIOs by THP-1 macrophages. THP-1 cells were treated for up to 24 hours with standard growth serum medium supplemented with varying doses of PEG-PPS-USPIOs in PBS. As a negative control, PBS was used in place of the PEG-PPS-USPIO colloidal suspension. Iron internalization and initial doses were quantified using a colorimetric phenanthroline assay, and internalized iron content was normalized to cell number indirectly via a protein assay. (A) Internalization of nanoparticles over the time period of interest is described by first-order rate kinetics, indicating that initial dose of nanoparticles is the primary determinant of internalization rate and total internalization amount. Relative to the initial doses of USPIOs, macrophages receiving 30 μ M, 60 μ M, and 120 μ M of iron endocytosed 8.4% \pm 3.7%, 7.7% \pm 3.2%, and 6.2% \pm 0.9% of the maximum possible USPIOs, respectively. Error bars indicate standard deviations from six independent experiments. (B) Derivatives of the best-fit kinetic equations plotted in (A) demonstrate further the dependence of uptake rate on initial dose of PEG-PPS-USPIOs. (C) Of the three sizes investigated, 100 nm nanoparticles were most effectively internalized by the macrophages. Smaller nanoparticles were internalized less effectively, and 30 nm nanoparticles experienced almost negligible uptake levels over the 24 hour experimental period. Normalization of the 24 hour uptake amounts to the initially administered doses shows that macrophages internalized 6.2% \pm 0.9%, 1.4% \pm 2.3%, and 1.1% \pm 0.3% of the 100 nm, 40 nm, and 30 nm PEG-PPS-USPIOs, respectively. Error bars represent standard deviation from three to six independent experiments. (D) Fluorescent imaging of the delivery of 40 nm and 100 nm fluorescent PEG-PPS-USPIO micelles. The uptake of 100 nm nanoparticles was easily visualized at 20X magnification with a 0.7 second exposure time, but even with a lower magnification and roughly a three-fold higher exposure time, the microscope was insufficiently sensitive to visualize the internalization of the 40 nm nanoparticles. (E) 40 nm PA-USPIOs (at 200 μ M Fe) or 100 nm PEG-PPS-USPIOs (at 120 μ M Fe) were co-administered to THP-1 macrophages with varying amounts of fucoidan for 24 hours, and allowed to incubate overnight prior to cell lysis and measurement of internalized iron. Increasing concentrations of fucoidan correlated with decreased uptake of the nanoparticles, suggesting that the mechanism of PEG-PPS-USPIO uptake is via receptor-mediated endocytosis, and facilitated by the scavenger receptor CD204. Error bars represent standard deviation of three independent experiments.

Abbreviations: PA-USPIOs, proximity-activated ultrasmall superparamagnetic iron oxides; PBS, phosphate buffered saline; PEG, poly(ethylene glycol); PPS, poly(propylene sulfide); THP, human acute monocytic leukemia cell line.

As an example, varying doses of the 100 nm PEG-PPS-USPIOs were administered to THP-1 macrophages. Because first-order rate equations are often used as governing equations in efforts to model receptor-mediated endocytosis of nanoparticles by macrophages,²⁵ the resulting 24-hour uptake profiles (Figure 2A) were fit to first-order rate kinetic equations (Figure 2A and B). The successful curve-fit suggested that USPIO concentration is the primary determinant of uptake rate. The best-fit equations take the form:

$$[C] = [C]_{\max}(1 - e^{-kt}) \quad (2)$$

where $[C]_{\max}$ represents the maximum possible concentration of iron in the cells and $[C]$ is a measure of the accumulated iron content in the cells. As the fit equations show (Figure 2A), the calculated $[C]_{\max}$ values are proportional to the initially administered doses of PEG-PPS-USPIOs (standard errors $< 13\%$), while the calculated rate constants k do not vary significantly across the doses (standard

errors 25%–40%). Relative to the initial doses of USPIOs, macrophages receiving 30 μ M, 60 μ M, and 120 μ M of iron endocytosed 8.4% \pm 3.7%, 7.7% \pm 3.2%, and 6.2% \pm 0.9% of the maximum possible USPIOs, respectively. In order to ensure that the measurements excluded USPIO binding events not resulting in uptake, some experiments were also conducted at 4°C to block endocytosis, resulting in insignificant iron levels quantified in the lysates (Supplementary Figure S3). In addition, a live/dead cytotoxicity assay was also conducted in order to confirm that treatment of macrophages with the PEG-PPS-USPIOs resulted in minimal cell death (Supplementary Figure S4).

Similar nanoparticle uptake kinetics were also observed for particles of smaller hydrodynamic diameters (Figure 2C). The results also show that by mass, smaller nanoparticles are internalized less effectively than their larger counterparts. The 40 nm nanoparticles shown in this graph were based on a higher iron dose for easier visualization; however, the same nanoparticles, administered at the same 120 μ M Fe dose as the other two samples, were internalized at 0.36 \pm 0.55 μ g/mg protein (curve not shown). Normalization of the 24-hour uptake data to the initially administered doses shows that THP-1 macrophages were able to internalize 1.1% \pm 0.3%, 1.4% \pm 2.3%, and 6.2% \pm 0.9% of the 30 nm, 40 nm, and 100 nm PEG-PPS-USPIOs, respectively. When nanoparticle internalization is normalized to cell number, a 70% decrease in PEG-PPS-USPIO diameter corresponded with almost a ten-fold decrease in iron uptake per cell. This was supported by fluorescence microscopy experiments, where macrophages were treated with FITC-tagged nanoparticles (Figure 2D), demonstrating the accumulation of 100 nm micelles within the macrophages. Despite longer exposure times at a lower magnification, the microscope was insufficiently sensitive to visualize the internalization of the 40 nm micelles by the macrophages. Taken together, these data suggest a positive correlation between nanoparticle size and their non-specific recognition and internalization by macrophages.

Given the lack of any specific targeting moieties on the micelle surface, this evidence suggested that within the nanoparticle size range investigated, macrophages were able to optimally recognize and internalize PEGylated nanoparticles of >100 nm diameter. Further, smaller nanoparticles seemed to experience significantly less non-specific uptake by the macrophages. One of the mechanisms of uptake is likely through receptor-mediated endocytosis via CD204 – as PEG-PPS-USPIO internalization can be effectively blocked by co-administration of nanoparticles with fucoidan, which is a well-known CD204 ligand (Figure 2E).⁴

We next investigated the effects of nanoparticle charge on non-specific uptake. Because the sub-40 nm nanoparticles provided a satisfactorily minimal baseline uptake over 24 hours, we opted to focus on nanoparticles of this size for this section of the study. End-carboxylated, -aminated, and -thiolated Pluronic were used as surfactants in inverse emulsion polymerization as described previously.¹⁰ The resulting Pluronic-PPS nanoparticles were loaded with USPIOs via direct hydration (Figure 3A–C), and delivered to THP-1 macrophages under the same conditions described for the other cell experiments above. Since Pluronic polymers are PEG-containing block co-polymers, the properties of Pluronic-PPS are not very different from those of PEG-PPS used in the other studies shown here, and, in effect, still produce PEG-PPS-coated USPIOs. Pluronic-PPS enables facile synthesis schemes necessary to produce the various end-functionalized polymers used in this work that would otherwise be more difficult to generate from PEG-PPS coatings.¹⁹

In order to account for differences in USPIO loading efficiencies across the library of Pluronic-PPS nanoparticle formulations, uptake was not only reported as [Fe]/[Protein] as above, but further normalized to initial doses of iron and reported as percent injected dose/protein (%ID/mg protein; Figure 3D, Table 1). We hypothesized that this system would enable us to parse out the roles of surface charge from size on nanoparticle internalization, leading us to identify the sensitivity of size and charge on nanoparticle non-specific uptake by macrophages.

The Pluronic-PPS-USPIOs initially exhibited surface charges from -23 mV up to $+9$ mV, but following incubation in 10% serum media for 4 hours, all nanoparticle formulations experienced significant changes in ζ potential (Figure 3D). Therefore, while the ζ potential of the nanoparticles was tunable to some extent by varying the surface chemistry of the nanoparticles, electrostatic interactions with serum proteins and components, as well as protein adsorption and opsonization processes contributed to significant changes in nanoparticle properties. The addition of serum into the incubation medium for these studies is intended to reflect an interaction environment that includes important components of the *in vivo* environment. Since there is no opportunity for nanoparticle purification following intravenous injection, we elected to allow nanoparticle interaction with serum proteins during ζ potential measurements, and later on, incubation with THP-1 cells. One outcome of this approach, and equally true *in vivo*, is the modulation of initial nanoparticle ζ potential by serum protein adsorption. These processes have been studied in detail for the Pluronic-PPS nanoparticle system, as

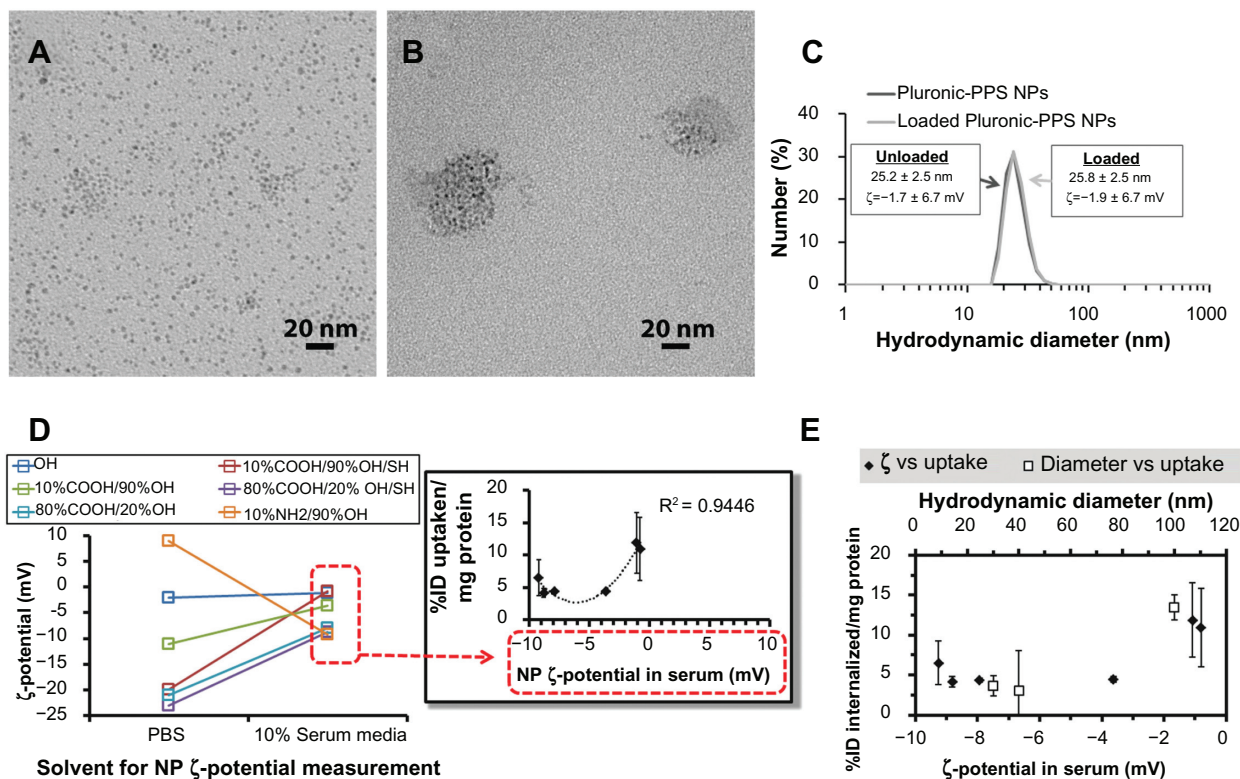


Figure 3 Effects of nanoparticle surface charge and chemistry on macrophage uptake. Representative TEM images of (A) hydrophobic, unloaded 3 nm OA-USPIOs and (B) water-soluble Pluronic-PPS nanoparticles after loading with the OA-USPIOs. (C) The loading process does not significantly affect the hydrodynamic diameters or the ζ potentials inherent to the Pluronic-PPS nanoparticles. (D) ζ -potential of all nanoparticle formulations (color-coded by surface chemistry) was originally measured in PBS following synthesis, and again following incubation in 10% serum media. While modulation of surface chemistry allows for a wide range of ζ -potentials, this range is compressed due to interactions between nanoparticles and media components. Uptake of nanoparticles correlated with their surface charge as measured in media (inset; red dotted boxes indicate source of data for x-axis), according to a parabolic distribution. To account for differences in USPIO loading efficiency across the different Pluronic-PPS nanoparticle formulations, nanoparticle uptake was normalized to the initial dose administered as well as cell content indirectly, via a protein assay. Error bars indicate standard deviation for three independent experiments. (E) Cell internalization data is plotted versus nanoparticle ζ -potentials measured in 10% serum media (solid squares). In order to determine which nanoparticle feature may be more determinant of non-specific interactions with macrophages, the effects of nanoparticle diameter have also been plotted for comparison (open squares).

Abbreviations: OA-USPIOs, oleic acid-stabilized ultrasmall superparamagnetic iron oxides; PBS, phosphate buffered saline; PPS, poly(propylene sulfide); TEM, transmission electron microscopy.

reported by Thomas et al.¹⁰ In particular, varying the surface chemistry of this nanoparticle system influenced the ability of the nanoparticles to become functionalized with the C3 complement proteins.¹⁰ More generally, this phenomena is well known in the synthetic gene delivery field, in which cationic nanoscale carriers of pDNA or siRNA rapidly interact with albumin and other serum proteins *in vivo*, and is consistent with the findings reported here.²⁶ This is significant because many consider that a minimum ζ potential of ± 30 mV is necessary in order to form stable nanoparticle suspensions.²⁷ Because electrostatic interactions and adsorption processes between serum proteins and the nanoparticle surface are inevitable following *in vivo* administration, higher ζ potential magnitudes may actually promote these processes, and in turn, opsonization processes ultimately leading to nanoparticle clearance from the bloodstream.

The observed decrease in the magnitude of the nanoparticle ζ potentials did not correspond with increased

agglomeration, as no flocculation or sedimentation was observed in any of the samples following treatment with serum. This observation was true of all nanoparticle formulations regardless of surface chemistry, possibly owing to the colloidal stability of Pluronic-PPS nanoparticles as shown previously.¹⁹

The two formulations that were most efficiently internalized were the nanoparticles displaying the terminal OH ($12\% \pm 5\% \text{ ID/mg protein}$) and the 10%COOH/90% OH/SH ($11\% \pm 5\% \text{ ID/mg protein}$). Uptake correlated with nanoparticle charge as measured in serum, yielding a parabolic trend with maximum uptake observed for cationic and strongly anionic nanoparticles (Figure 3D, $R^2 = 0.94$, inset). However, because interactions with serum compressed the range of nanoparticle ζ potentials, we were unable to experimentally explore uptake of the nanoparticles beyond the -10 mV to 0 mV range. Despite the narrow window of ζ potentials covered by the data, the trends suggest that

non-specific uptake of nanoparticles may be promoted by nanoparticle cationicity or high anionicity. This is consistent with previous observations.¹³

Uptake of nanoparticles in serum was minimized in the range of ζ potentials from -9.0 mV to -3.5 mV. A three-fold increase in uptake was measured for identically sized nanoparticles having ζ potentials in serum from -3.5 mV to -0.8 mV, representing a 77% decrease in anionicity. In comparison, a four-fold change in uptake was observed for a 60% decrease in PEG-PPS-USPIO diameter (100 nm to 40 nm). Over these ranges and conditions, macrophage uptake of these nanoparticles is 42% more sensitive to size than to ζ potential (Figure 3E).

To expand on this conclusion, we synthesized PEG-PPS-USPIOS containing an MMP-9-degradable peptide (M9C) within the PEG chain (Figure 4A and B). This design results in particles that respond to active MMP-9 in the environment by releasing a layer of PEG, effectively leading to a decrease in nanoparticle diameter. Probes for MMP-9 activity are of wide interest because of the upregulation of MMP-9 in the progression of atherosclerosis.^{28–30} Based on the studies described earlier, we hypothesized that this experimental contrast agent would experience less uptake by macrophages following treatment with MMP-9, relative to the as-synthesized, intact form.

These MMP-9-responsive contrast agents were synthesized by encapsulating 10 nm and 3 nm OA-USPIOS using approximately 10 kDa mPEG-[M9C]-PEG-PPS (subsequently referred to as “PA” for protease-activatable), to produce 60 nm and 30 nm PA-USPIOS (Figure 4C and D). Both PA-USPIO formulations responded to MMP-9 treatment with a 10–20 nm decrease in nanoparticle hydrodynamic diameters as measured by DLS, while ζ -potentials were not significantly affected (30 nm PA-USPIOS: -3.9 ± 6.4 mV pre-cleavage, -2.8 ± 5.9 mV post-cleavage; 60 nm PA-USPIOS: 0.0 ± 7.1 mV pre-cleavage, -4.7 ± 5.5 mV post-cleavage). For cell experiments, PA-USPIOS were incubated with MMP-9 for 24 hours prior to their administration to THP-1 cells at equivalent iron doses. In both cases, MMP-9-treated PA-USPIOS were internalized significantly less effectively than their non-cleaved counterparts (Figure 4E). Most notably, the 30 nm PA-USPIOS experienced a six-fold decrease in nanoparticle uptake following MMP-9 cleavage (0.12 ± 0.04 $\mu\text{g Fe}/\text{mg protein}$ pre-cleavage vs 0.02 ± 0.02 $\mu\text{g}/\text{mg}$ post-cleavage). Also of note is the slightly higher uptake of the MMP-9-treated 60 nm PA-USPIOS (final diameter = 40.0 ± 6.2 nm) relative to the untreated 30 nm PA-USPIOS (30.0 ± 2.6 nm).

Because these changes in nanoparticle internalization may be due to MMP-9-mediated modifications on the cell membranes, a series of control experiments were also performed, using non-cleavable, 40 nm PEG-PPS-USPIOS (Supplementary Figure S5). In these experiments, co-administration of non-cleavable nanoparticles with MMP-9 did not lead to significant differences in nanoparticle internalization. Further, co-administration with a MMP-9 inhibitor also did not affect internalization. Taken together, the results suggest that the variations in PA-USPIO internalization by the THP-1 cells were attributable to the size of the nanoparticles, as the nanoparticle ζ potentials did not vary significantly before versus after treatment with MMP-9. Further, cellular capacity for nanoparticle internalization was unaffected by exposure to protease.

To determine if these MMP-9-dependent differences in nanoparticle internalization result in statistically significant changes in sample T_2 relaxation, and therefore, clinically relevant detection of MMP-9 activity in cell samples, 60 nm PA-USPIO-treated cells were pelleted and imaged on a 4.7 T magnetic resonance imaging scanner (Figure 4F). Through the use of a CPMG spin-echo pulse sequence, MMP-9-treated PA-USPIOS appeared to exhibit higher mean gray intensities versus cells incubated with untreated PA-USPIOS.

While the PA-USPIOS exhibited $T_2 = 4.82 \pm 0.02$ ms, the PA-USPIOS on the macrophages exhibited $T_2 = 23.2 \pm 3.5$ ms. These rather strong changes in T_2 are somewhat surprising assuming that approximately 1% of the administered dose was taken up by the macrophages as measured in the earlier sections of this work. This implies that for each imaging slice, the concentration of iron responsible for T_2 signal modulation within that slice is about 100-fold less in the nanoparticle-treated cell samples versus the positive control. To quantify this phenomenon, the calculated values above (from first-principle measurements) can be plugged into the R_2 relaxivity equation:

$$R_2 = \frac{1}{T_2 \times [Fe]} \quad (3)$$

in order to produce a measure of how effective the USPIOS are in modulating the local negative contrast. Given that measured T_2 in the cell samples is only approximately five times higher than the measurements in the positive control, the iron concentration in the cell samples would need to be about a fifth of the concentration in the positive control in order to maintain the same R_2 value. As we have seen, this

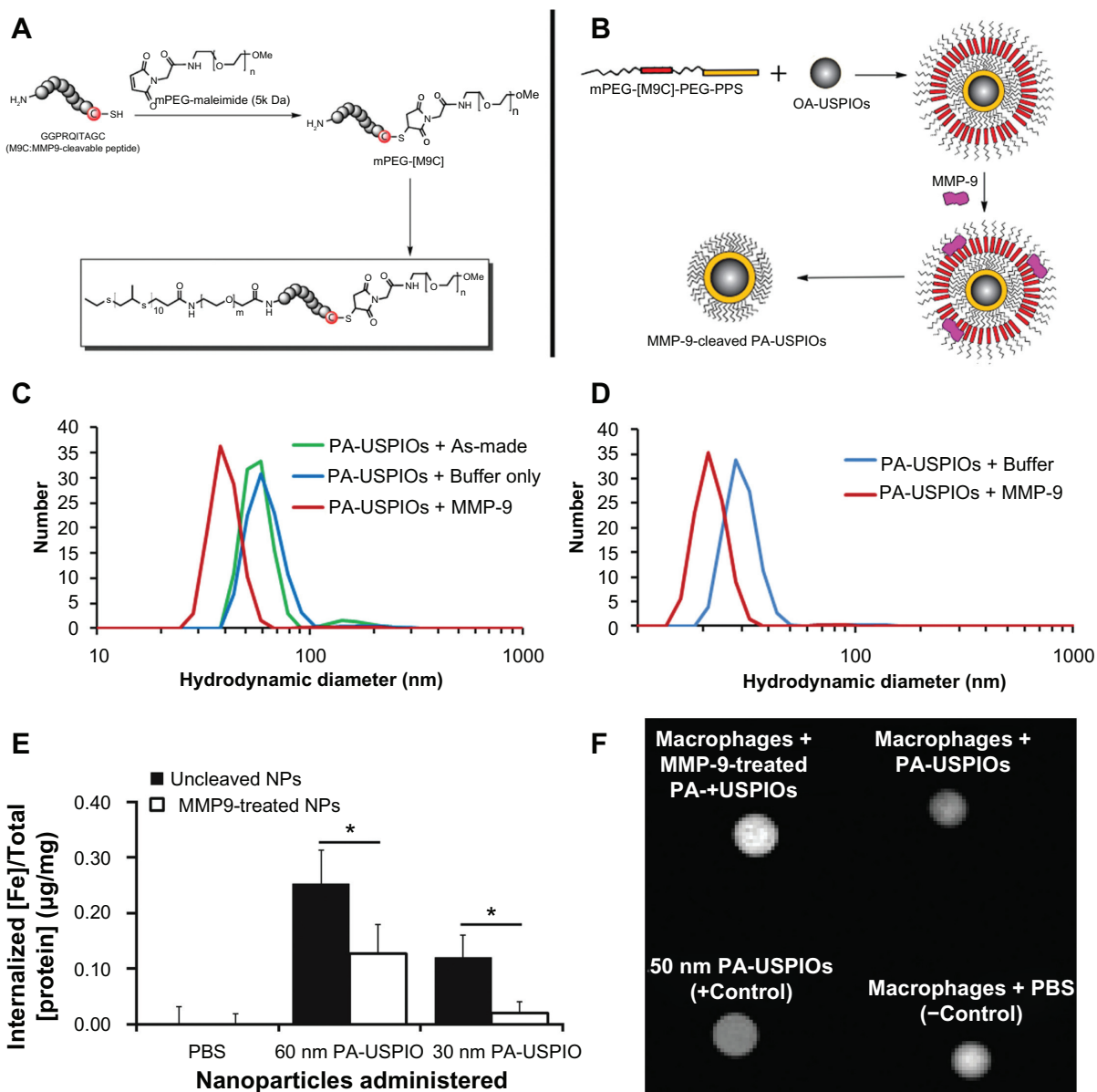


Figure 4 Behavior of MMP-9-responsive PA-USPIOs. **(A)** Synthesis of MMP-9-cleavable PEG-PPS chains (mPEG-[M9C]-PEG-PPS; PA) and **(B)** encapsulation of USPIOs to form PA-USPIOs. MMP-9 is able to recognize and cleave the (M9C) peptide sequence, resulting in release of a layer of PEG from the nanoparticle surface, accompanied by a decrease in nanoparticle hydrodynamic diameter. **(C)** DLS characterization of hydrodynamic diameters of as-synthesized 60 nm PA-USPIOs (**C**; green) and 30 nm PA-USPIOs (**D**; blue) demonstrates a loss in hydrodynamic diameter following treatment with MMP-9. **(E)** Buffer-treated or MMP-9-pretreated nanoparticles were delivered to THP-1 macrophages for 24 hours in standard growth medium. As a control, PBS was used in place of the nanoparticles. For both PA-USPIO formulations tested, the decrease in nanoparticle size following MMP-9 treatment results in less effective nanoparticle internalization by the macrophages. Error bars represent standard deviations from three to six independent experiments. **(F)** T_2 -weighted MRI of THP-1 cells treated with MMP-9-cleaved PA-USPIOs appeared brighter than cells incubated with untreated PA-USPIOs, indicating that less cleaved nanoparticles were internalized by the macrophages versus the untreated PA-USPIOs.

Note: $^*P < 0.05$ by Student's *t*-test.

Abbreviations: DLS, dynamic light scattering; MMP-9, matrix metalloproteinase-9; PA-USPIOs, proximity-activated ultrasmall superparamagnetic iron oxides; MRI, magnetic resonance imagery; PBS, phosphate buffered saline; PEG, poly(ethylene glycol); PPS, poly(propylene sulfide).

is hardly the case, and based on our data, we can conclude that the R_2 values in the cell sample would have to be on the order of 20-fold larger than the R_2 of the free-floating PA-USPIOs. These results indicate that following internalization by the macrophages, the PA-USPIOs are being manipulated in such a way that increases their ability to exert T_2 contrast.

This phenomenon can be explained by previous observations that aggregated or clustered superparamagnetic nanoparticles result in higher R_2 versus fully dispersed, singlet nanoparticles.^{16,31} Others have demonstrated via TEM that following endocytosis of iron oxide nanoparticles, macrophages can process the particles into lysosomes, where dense clusters of particles can usually be observed.³²

Taken together, these other observations help explain how even a small amount of nanoparticle uptake results in a marked change in T_2 contrast in the system.

Conclusion

PEGylated nanoparticles are internalized by macrophages in a size-dependent fashion for diameters between 30 nm and 100 nm. Charge-uptake relationships were investigated by varying the surface properties of nanoparticles. While the data supports the possibility that cationic and strongly anionic nanoparticles may be internalized most effectively, within the ranges investigated, nanoparticle size, not charge, is a stronger determinant of non-specific uptake by macrophages. Based on this information, an MMP-9-sensitive nanoparticle was developed that decreases in size following treatment with MMP-9. Macrophages respond to MMP-9-treated nanoparticles in a predictable fashion, and cleaved nanoparticles were consistently phagocytosed less efficiently than their untreated counterparts, demonstrating the effects of dynamic nanoparticle size modulation on macrophage uptake. These MMP-9-induced differences in uptake are also detectable via MRI. Despite the low levels of overall uptake over the 24 hour incubation periods ($\leq 1\%$ initially administered dose), a significant increase in macrophage R_2 was observed. Presumably, and consistent with quantitative analysis, the clustering of nanoparticles into endosomes following endocytosis results in an increase in nanoparticle R_2 , providing amplification of negative MR image contrast. The results presented here inform the design of nanoparticles to target or evade macrophages in future *in vivo* applications.

Acknowledgments

This work was supported by a Vanderbilt University Intramural Discovery Grant (4-48-999-9132), the Department of Defense Congressionally Directed Medical Research Programs (W81XWH-08-1-0502), and a Whitaker International Scholarship to SNT. CML acknowledges support through a fellowship from the Vanderbilt University Undergraduate Summer Research Program (VUSR). Dynamic light scattering and TEM were conducted through the use of the core facilities of the Vanderbilt Institute of Nanoscale Sciences and Engineering (VINSE), using facilities renovated under NSF ARI-R2 DMR-0963361. We thank Dr Daniel Colvin of the Vanderbilt University Institute of Imaging Science (VUIIS) for his assistance with MRI imaging and analysis. We also acknowledge the laboratories of Professors Hak-Joon Sung and Craig L Duvall (Vanderbilt Biomedical Engineering), whose equipment were instrumental to the execution of this work.

Disclosure

The authors have no conflicts of interest to disclose.

References

- Martin P. Wound healing – aiming for perfect skin regeneration. *Science*. 1997;276(5309):75–81.
- Bouwens L, Baekeland M, De Zanger R, Wisse E. Quantitation, tissue distribution and proliferation kinetics of Kupffer cells in normal rat liver. *Hepatology*. 1986;6(4):718–722.
- Felix R, Cecchini MG, Hofstetter W, Elford PR, Stutzer A, Fleisch H. Impairment of macrophage colony-stimulating factor production and lack of resident bone marrow macrophages in the osteopetrotic op/op Mouse. *J Bone Miner Res*. 1990;5(7):781–789.
- Brown MS, Goldstein JL. Lipoprotein metabolism in the macrophage: implications for cholesterol deposition in atherosclerosis. *Annu Rev Biochem*. 1983;52:223–261.
- Linehan SA, Martinez-Pomares L, Gordon S. Mannose receptor and scavenger receptor: two macrophage pattern recognition receptors with diverse functions in tissue homeostasis and host defense. *Adv Exp Med Biol*. 2000;479:1–14.
- Kindt TJ, Goldsby RA, Osborne BA, Kuby J. *Kuby Immunology*. 6th ed. New York: W.H. Freeman; 2007.
- Plüddemann A, Neyen C, Gordon S. Macrophage scavenger receptors and host-derived ligands. *Methods*. 2007;43(3):207–217.
- Chnari E, Nikitczuk JS, Wang J, Uhrich KE, Moghe PV. Engineered polymeric nanoparticles for receptor-targeted blockage of oxidized low density lipoprotein uptake and atherosogenesis in macrophages. *Biomacromolecules*. 2006;7(6):1796–1805.
- Lipinski MJ, Amirbekian V, Frias JC, et al. MRI to detect atherosclerosis with gadolinium-containing immunomicelles targeting the macrophage scavenger receptor. *Magn Reson Med*. 2006;56(3):601–610.
- Thomas SN, van der Vlies AJ, O’Neil CP, et al. Engineering complement activation on polypropylene sulfide vaccine nanoparticles. *Biomaterials*. 2011;32(8):2194–2203.
- Doshi N, Mitragotri S. Macrophages recognize size and shape of their targets. *PLoS One*. 2010;5(4):e10051.
- Taylor PR, Brown GD, Herre J, Williams DL, Willment JA, Gordon S. The role of SIGNR1 and the beta-glucan receptor (dectin-1) in the nonopsonic recognition of yeast by specific macrophages. *J Immunol*. 2004;172(2):1157–1162.
- Raynal I, Prigent P, Peyramaure S, Najid A, Rebuzzi C, Corot C. Macrophage endocytosis of superparamagnetic iron oxide nanoparticles: mechanisms and comparison of ferumoxides and ferumoxtran-10. *Invest Radiol*. 2004;39(1):56–63.
- Ratner BD. *Biomaterials Science: an Introduction to Materials in Medicine*. San Diego, CA: Academic Press; 1996.
- Velluto D, Demurtas D, Hubbell JA. PEG-b-PPS diblock copolymer aggregates for hydrophobic drug solubilization and release: cyclosporin A as an example. *Mol Pharm*. 2008;5(4):632–642.
- Yu SS, Scherer RL, Ortega RA, et al. Enzymatic- and temperature-sensitive controlled release of ultrasmall superparamagnetic iron oxides (USPIOs). *J Nanobiotechnology*. 2011;9:7.
- Deguchi JO, Aikawa M, Tung CH, et al. Inflammation in atherosclerosis: visualizing matrix metalloproteinase action in macrophages *in vivo*. *Circulation*. 2006;114(1):55–62.
- Chan WC, White PD, editors. *Fmoc Solid Phase Peptide Synthesis: a Practical Approach*. Oxford, UK: Oxford University Press; 2000.
- Rehor A, Hubbell JA, Tirelli N. Oxidation-sensitive polymeric nanoparticles. *Langmuir*. 2005;21(1):411–417.
- van der Vlies AJ, O’Neil CP, Hasegawa U, Hammond N, Hubbell JA. Synthesis of pyridyl disulfide-functionalized nanoparticles for conjugating thiol-containing small molecules, peptides, and proteins. *Bioconjug Chem*. 2010;21(4):653–662.
- Christian GD. *Analytical Chemistry*. 5th ed. New York: Wiley & Sons; 1994.

22. Woo K, Hong J, Choi S, et al. Easy synthesis and magnetic properties of iron oxide nanoparticles. *Chem Mater*. 2004;16(14):2814–2818.
23. Griffin EE, Ullery JC, Cox BE, Jerome WG. Aggregated LDL and lipid dispersions induce lysosomal cholesterol ester accumulation in macrophage foam cells. *J Lipid Res*. 2005;46(10):2052–2060.
24. Jerome WG, Cox BE, Griffin EE, Ullery JC. Lysosomal cholesterol accumulation inhibits subsequent hydrolysis of lipoprotein cholesterol ester. *Microsc Microanal*. 2008;14(2):138–149.
25. Ece Gamsiz D, Shah LK, Devalapally H, Amiji MM, Carrier RL. A model predicting delivery of saquinavir in nanoparticles to human monocyte/macrophage (Mo/Mac) cells. *Biotechnol Bioeng*. 2008;101(5):1072–1082.
26. Phillips NC, Heydari C. Modulation of cationic liposomal DNA zeta potential and liposome-protein interaction by amphiphilic poly (ethylene glycol)*. *Pharm Pharmacol Commun*. 1996;2(2):73–76.
27. Han F, Li S, Yin R, Liu H, Xu L. Effect of surfactants on the formation and characterization of a new type of colloidal drug delivery system: nanostructured lipid carriers. *Colloids Surf A: Physicochem Eng Asp*. 2008;315(1–3):210–216.
28. Gough PJ, Gomez IG, Wille PT, Raines EW. Macrophage expression of active MMP-9 induces acute plaque disruption in apoE-deficient mice. *J Clin Invest*. 2006;116(1):59–69.
29. Schellenberger E, Rudloff F, Warmuth C, Taupitz M, Hamm B, Schnorr J. Protease-specific nanosensors for magnetic resonance imaging. *Bioconjug Chem*. 2008;19(12):2440–2445.
30. Sluijter JP, Pulskens WP, Schoneveld AH, et al. Matrix metalloproteinase 2 is associated with stable and matrix metalloproteinases 8 and 9 with vulnerable carotid atherosclerotic lesions: a study in human endarterectomy specimen pointing to a role for different extracellular matrix metalloproteinase inducer glycosylation forms. *Stroke*. 2006;37(1):235–239.
31. Perez JM, O'Loughlin T, Simeone FJ, Weissleder R, Josephson L. DNA-based magnetic nanoparticle assembly acts as a magnetic relaxation nanoswitch allowing screening of DNA-cleaving agents. *J Am Chem Soc*. 2002;124(12):2856–2857.
32. Müller K, Skepper JN, Posfai M, et al. Effect of ultrasmall superparamagnetic iron oxide nanoparticles (Ferumoxtran-10) on human monocyte-macrophages in vitro. *Biomaterials*. 2007;28(9):1629–1642.

Supplementary figures

Online supplementary materials include the following Figures: (S1) control over iron oxide nanoparticle size, (S2) Lowry protein assay standard curves, (S3) nanoparticle

binding experiments, (S4) nanoparticle cytotoxicity assay, and (S5) control internalization experiments involving MMP-9, MMP-9 inhibitor, and protease-insensitive nanoparticles.

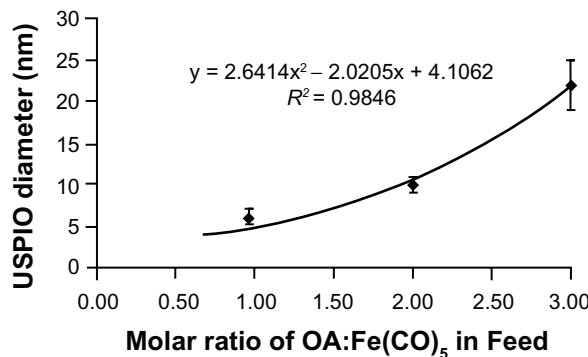


Figure S1 Feed ratio of oleic acid surfactant to iron pentacarbonyl precursors and resulting USPIO diameters. A 6 mmol quantity of $\text{Fe}(\text{CO})_5$ was introduced into reactors containing 40 mL octyl ether and varying amounts of oleic acid at 100°C. USPIO cores were allowed to grow and then oxidize as described in materials and methods, and then imaged by HRTEM. Core diameters were measured via ImageJ software.

Abbreviations: HRTEM, high resolution transmission electron microscope; USPIO, ultrasmall superparamagnetic iron oxides.

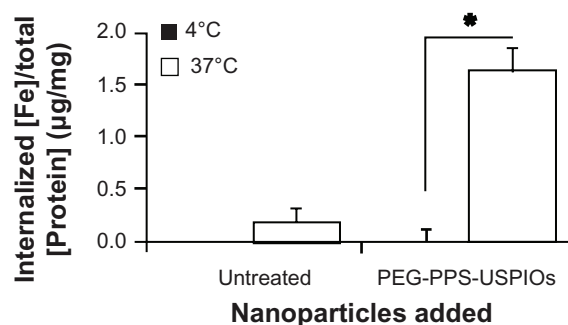


Figure S3 Twenty-four hour uptake of nanoparticles by THP-I macrophages. Cells were treated with 40 nm PEG-PPS-USPIOs for 24 hours, and then measured for iron content via the phenanthroline assay. Iron content was normalized to cell number indirectly via a protein assay. To confirm that the phenanthroline assay measures internalized nanoparticles and not just nanoparticles that have bound to macrophage receptors, some cells were incubated with nanoparticles at 4°C. Results showed about ten-fold lower iron content in these samples relative to samples treated at 37°C, indicating that the protocol successfully lyses cells and enables measurements of internalized iron.

Note: Error bars indicate standard deviation of three independent experiments (* $P < 0.01$).

Abbreviations: PEG, poly(ethylene glycol); PPS, poly(propylene sulfide); USPIO, ultrasmall superparamagnetic iron oxides; THP, human acute monocytic leukemia cell line.

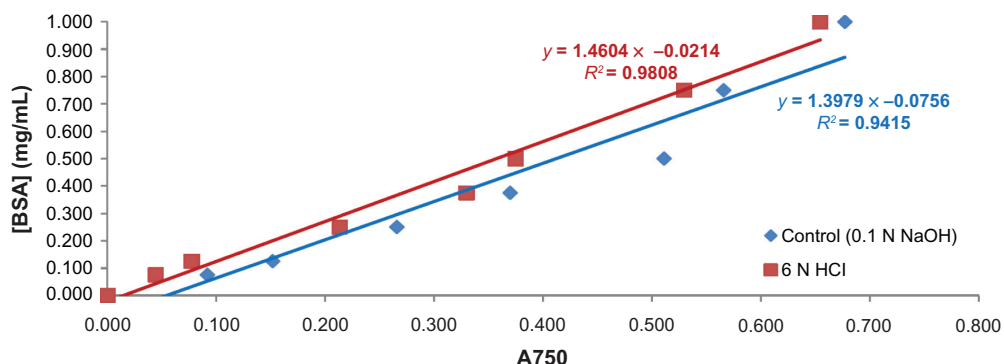


Figure S2 Lowry protein assay standard curves. BSA was dissolved in PBS and treated with either 0.1 N NaOH or 6 N HCl prior to performance of the Lowry protein assay. While the assay is typically run under alkaline conditions (blue), strong acidic conditions do not significantly affect the sensitivity or reliability of this assay.

Abbreviations: BSA, bovine serum albumin; PBS, phosphate buffered saline.

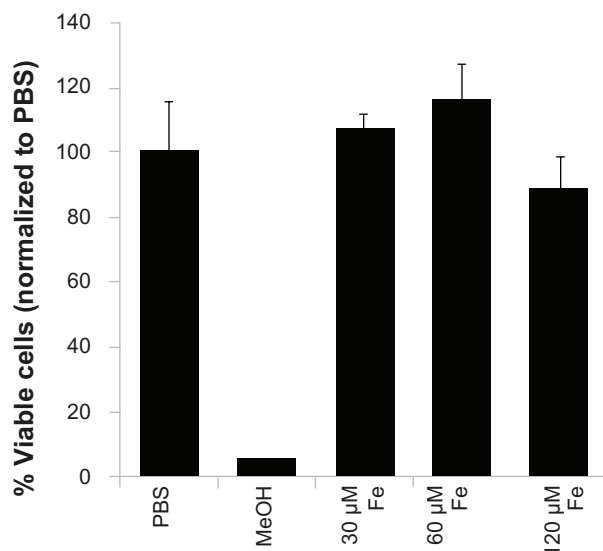


Figure S4 Cell viability measurements on nanoparticle-treated THP-1 cells, normalized to untreated cells (media + PBS). Cells were treated with increasing doses of 100 nm PEG-PPS-USPIOs for 24 hours, prior to removal of unbound nanoparticles and assessment of cell viability via quantification of calcein-AM/ethidium homodimer staining. Dosage on the x-axis represents actual iron concentration within the samples. No statistically significant differences in viability were observed between any of the treatment groups ($n = 3$).

Abbreviations: PBS, phosphate buffered saline; PEG, poly(ethylene glycol); PPS, poly(propylene sulfide); USPIO, ultrasmall superparamagnetic iron oxides; THP, human acute monocytic leukemia cell line.

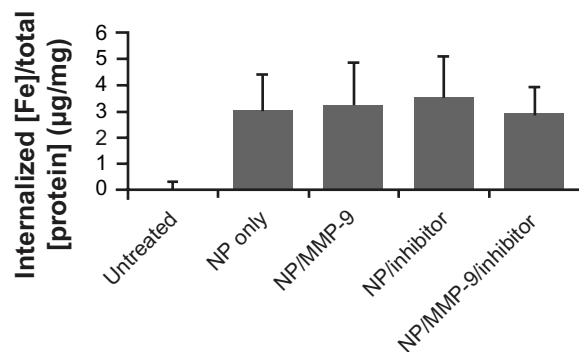


Figure S5 Co-administration of 40 nm PEG-PPS-USPIOs (do not contain MMP-9-cleavable peptide) with MMP-9 does not significantly affect internalization of nanoparticles. THP-1 cells were treated with media only (untreated), nanoparticles only, or nanoparticles co-administered with 200 ng/mL MMP-9 and/or 300 ng/mL MMP-9 inhibitor. Because these nanoparticles do not contain MMP-9-cleavable elements, their diameter is unaffected by treatment (data not shown). MMP-9 treatment does not change the properties of the THP-1 cell membrane in a way that affects their interactions with nanoparticles. Error bars indicate standard deviation for three independent experiments.

Abbreviations: MMP-9, matrix metalloproteinase-9; PEG, poly(ethylene glycol); PPS, poly(propylene sulfide); USPIO, ultrasmall superparamagnetic iron oxides; THP, human acute monocytic leukemia cell line.